

2020

3D Printed Architected Materials for Improving Biofilm Carriers for Wastewater Treatment Applications

Bryan Ovelheiro
University of Massachusetts Amherst

Follow this and additional works at: https://scholarworks.umass.edu/cee_ewre



Part of the [Environmental Engineering Commons](#)

Ovelheiro, Bryan, "3D Printed Architected Materials for Improving Biofilm Carriers for Wastewater Treatment Applications" (2020). *Environmental & Water Resources Engineering Masters Projects*. 103. Retrieved from https://scholarworks.umass.edu/cee_ewre/103

This Article is brought to you for free and open access by the Civil and Environmental Engineering at ScholarWorks@UMass Amherst. It has been accepted for inclusion in Environmental & Water Resources Engineering Masters Projects by an authorized administrator of ScholarWorks@UMass Amherst. For more information, please contact scholarworks@library.umass.edu.

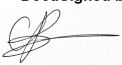
3D printed architected materials for improving biofilm carriers for wastewater treatment applications


A Masters Project Presented

by

Bryan Ovelheiro

Approved as to style and content by:

DocuSigned by:

01F608E2CB7F4FD...
Caitlyn S. Butler, Chairperson

DocuSigned by:

E2F7267C0325435...
Simos Gerasimidis, Member


DocuSigned by:

01F608E2CB7F4FD...
Caitlyn Butler
Civil and Environmental Engineering Department

Table of Contents

Acknowledgements.....	3
1. Introduction.....	4
1.1 Objectives and Hypotheses.....	8
2. Factors Affecting Biofilms in a Wastewater Treatment Setting.....	9
2.1 Design Considerations of Biofilm-Based Wastewater Treatment.....	10
2.2 Carrier Consideration and their Effects on Performance.....	11
2.2.1 Biofilm Thickness.....	11
2.2.2 Material Properties' Effects on Biofilm Development.....	11
2.2.3 Surface Characteristics' Effects on Biofilm Development.....	11
3. Manufacturing.....	13
3.1 Additive Manufacturing and Architected Materials.....	13
3.1.1 Cost of Additive Manufacturing.....	16
3.1.2 Energy Efficiency and Environmental Impacts of Additive Manufacturing.....	17
3.1.3 Quality of Additive Manufacturing.....	18
3.1.4 Selective Laser Sintering Process – an Overview.....	19
3.2 Conventional Biofilm Carrier Technologies.....	21
3.2.1 Moving Bed Biofilm Reactor (MBBR) Technology.....	21
3.2.2 The Plastic Extrusion Process – an Overview.....	21
4. Geometry Design and Preliminary Microscopy Study.....	23
4.1 Geometry Selection.....	23
4.2 3D Printing of Plates and Corresponding Error.....	25
4.3 Biofilm Imaging via Microscopy.....	27
5. Biofilm Treatment Performance.....	32
5.1 Methods.....	32
5.1.1 Pilot Treatment Study.....	34
5.1.2 Biofilm Kinetics.....	37
5.1.3 Biomass Quantification.....	37
5.2 Results.....	38
5.2.1 Pilot Treatment Study.....	38
5.2.2 Biofilm Performance.....	44
5.2.3 Biomass Quantification.....	48
5.3 Discussion.....	50
6. Biofilm Volume Quantification.....	57
6.1 Methods.....	57
6.2 Results.....	62
6.3 Discussion.....	65
7. Conclusions and Future Work.....	69
8. References.....	72
9. Appendix.....	83

Acknowledgements

I would like to thank the Massachusetts Technology Transfer Center ACORN grant, the University of Massachusetts Amherst, and the Department of Civil and Environmental Engineering. This research would not have been possible without the financial support of this grant, or the support provided to me by the department and school.

I would also like to express my sincere gratitude to my advisors and committee throughout this research, Drs. Caitlyn Butler and Simos Gerasimidis. This work would not have been possible without both their support and advice given to me during the course of this research. I am especially grateful for their patience, knowledge, and guidance as I undertook a project as large as this one.

Thank you also to my fellow group mates, Ian, Joann, and Sally, for helping me keep up with my experiments whenever I needed help.

Additionally, I would like to thank the Department of Civil and Environmental Engineering at the University of Massachusetts for helping to fund my research and providing me with guidance when I was unsure what my next steps were in selecting courses and planning my future semesters. I would also like to thank Jodi Ozdarski for helping me and answering my questions whenever I had issues with choosing classes.

I would also like to extend a thank you to my parents and my sister for their emotional support as I worked through both my thesis and completed my coursework. Thank you especially to my parents for supporting me and making my studies here at the University of Massachusetts possible.

Finally, and most importantly, I would like to thank my fiancée and best friend, Leslie Rosales. She has provided me with endless support during my research and helped me succeed when I thought it was impossible for me to complete such a large thesis. I could not have completed this project without the support of everyone involved.

1. Introduction

Wastewater infrastructure in the United States has been in dire need of improvement for quite a while. It was estimated that wastewater treatment systems would need about \$57.2 billion to maintain acceptable levels of treatment in the coming years (Christen, 2003). This is just for maintaining the treatment systems in place, without any room for improvement, and it only accounts for about 31.6% of the total wastewater infrastructure need in this area (Christen, 2003). In fact, without sufficient upgrades, water quality gains achieved through the passing of the Clean Water and Safe Drinking Water acts could be lost (Christen, 2003). More recently in 2013, the American Society of Civil Engineers (ASCE) estimated that if the current trend continues in which only partial funding is provided by the federal government to address the problem, the funding gap of both wastewater and water infrastructure is expected to reach \$84 billion (67% of total need) by 2020, and \$144 billion (73% of total need) by 2040 (ASCE, 2013). Because of this funding gap, wastewater treatment plants have to be able to address many of the shortcomings themselves. Therefore, wastewater treatment plants have to be able to perform more efficient treatment with less investment.

Currently, many wastewater treatment plants (WWTPs) use the conventional activated sludge (CAS) process to treat their wastewater, with roughly 74% of the United States population being served by these plants (Pabi, Amarnath, Goldstein, and Reekie, 2013). This process has been around for over a century. Developed by Edward Ardern and William Lockett in 1914 (Ardern and Lockett, 1914a; Ardern and Lockett, 1914b; Ardern and Lockett, 1915), the process allows for biological treatment of waste. This process makes up the secondary treatment part of the conventional wastewater treatment process. The following is a summary of the wastewater treatment process as summarized from (Hammer and Hammer, 2012). In this process, which is depicted in **Figure 1-1**, water comes in as raw wastewater. This water must undergo preliminary treatment, where large solids and grit are removed. Next, the wastewater undergoes primary treatment, where wastewater is allowed to settle in a large clarifier, referred to as a primary clarifier. Here, solids in the water settle to the bottom, while scum floats to the top. Next, the conventional activated sludge process officially begins. The clarified water, now referred to as primary effluent, enters an aeration basin, where the wastewater undergoes secondary treatment. The water in this basin is aerated to provide the microorganisms with oxygen. Here, microorganisms grow and form flocculated organic colloids and consume nutrients in the wastewater. These microorganisms are referred to as activated sludge, hence the name CAS. The nutrients that the microorganisms consume are the constituents that engineers seek to remove. In the conventional process, the goal is to remove biological oxygen demand (BOD), which is the sum of organic material in the water. After secondary treatment, the water enters a secondary clarifier, where the grown biomass can then be settled and removed from the wastewater. After settling, the water is disinfected and released to a receiving water body (Hammer and Hammer, 2012).

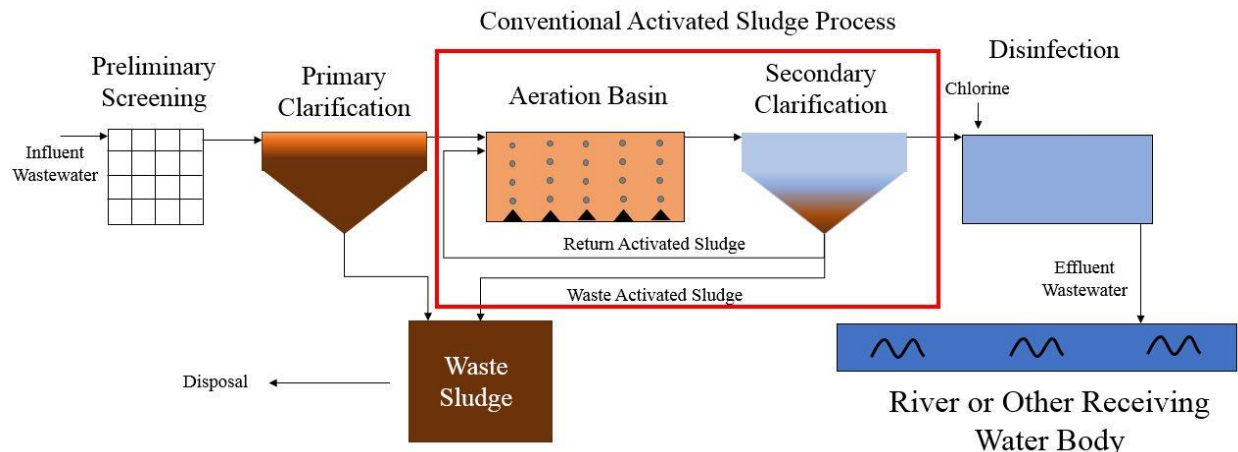


Figure 1-1: The wastewater treatment process steps with the conventional activated sludge process highlighted

While the conventional activated sludge process is a proven method, it may not be sufficient for all applications in today's changing world. Both biological oxygen demand and ammonia removal are important to the operation of a wastewater treatment plant. The removal of biological oxygen demand is important because it prevents large amounts of bacteria from feeding off of this BOD in a water body. Additionally, excessive ammonia also allows bacteria to oxidize the material and use it for further biomass growth. While older treatment systems targeted the removal of BOD alone, modern goals include nitrogen and phosphorus removal in an attempt to prevent eutrophication and deterioration of receiving water bodies (Pell and Wörman, 2008). This eutrophication can lead to large amounts of microorganisms to consume all of the dissolved oxygen in the water and kill the fish. One potential improvement to the conventional activated sludge process is to add biofilms to intensify the process overall and promote specialized treatment. Biofilms have the potential to form specialized relationships based on metabolic reactions (Subashchandrabose, Ramakrishnan, Megharaj, Venkateswarlu, and Naidu, 2011), meaning that one species of microorganisms is capable of processing the products of another, creating a chain of organics removal. Biofilm-based systems can also improve existing treatment by offering flexible procedures, smaller space demand, lower hydraulic retention time, increased resilience to changes in the environment, higher biomass retaining period, high active biomass concentration, as well as lower sludge production (Wang, Parajuli, Sivalingam, and Bakke, 2019).

A biofilm is an aggregation of microorganisms and their extracellular polymers (Rittmann and McCarty, 2001b). Biofilms can either be attached to a solid surface or self-encased as a floc or aggregated cells. In this thesis, we will focus on biofilms that form on solid surfaces. Biofilm goes through four main states of development, as illustrated by (Dirchx, 2013) (**Figure 1-2**). First, planktonic bacteria come into contact with a solid surface. They attach themselves to the surface. Once bacteria are present and attached to a surface, they begin to excrete extracellular polymeric substances (EPS). This EPS is composed of multipurpose polymers that help the biofilm's structure and function (Staudt, Horn, Hempel, and Neu, 2004). This EPS has an effect on both the biofilm and the macroenvironment around the biofilm (Staudt et al., 2004). The bacteria will then continue excreting EPS, as well as dividing and proliferating. The biofilm will continue to grow

until it reaches maturation. Once matured, the biofilm will reach a critical point where the bacteria in the biofilm can no longer withstand the exterior forces present on the biofilm, such as liquid shear, and some bacteria will begin to detach. Bacteria will once again become planktonic in the bulk liquid unless they attach themselves somewhere else. The cycle will repeat and more biofilms form. The original biofilm will also continue to grow.

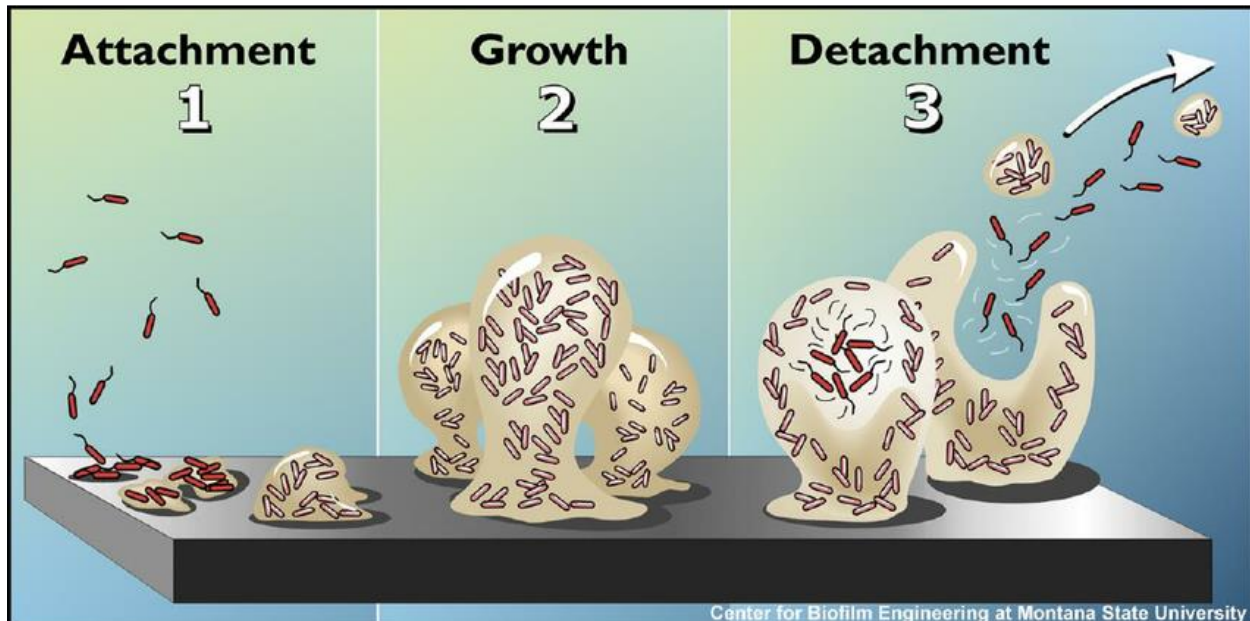


Figure 1-2: A schematic of biofilm formation from attachment to detachment. Retrieved from (Dirchx, 2013).

In recent decades, the moving bed biofilm reactor (MBBR) has been established as a robust method of using biofilm to treat wastewater. This is a retrofit solution that allows media to be added to existing processes to modify the process. In addition to intensifying the process overall, they can provide diversified treatment, allowing for the removal of different substrates. It also combines suspended processes with biofilm processes. Biofilms have been found to more efficient at removing chemical oxygen demand (COD), nitrogen, and phosphates (Naz, Seher, Perveen, Saroj, and Ahmed, 2015). MBBR systems involve placing small plastic media into a reactor, such as an existing aeration basin, to take advantage of bacteria's desire to form biofilm. The media are designed to have high surface area to volume ratios to promote maximum biofilm formation. The biofilm then treats the wastewater by removing BOD, among other contaminants present in wastewater (Phillips, Steichen, and Johnson, 2010). This media can be readily adapted to the conventional activated sludge processes by retrofitting the existing infrastructure. MBBRs have been shown to allow for BOD removal, nitrification, and denitrification to occur by utilizing different reactors within a treatment scheme (McQuarrie and Maxwell, 2003). The system can also allow for operational control, in terms of what treatment occurs (Steichen et al., 2009). Additionally, MBBR technology retains its biomass better than suspended-based systems, making them more resistant to wet-weather events that could potentially wash out bacteria (Phillips et al., 2010). The HRT can also be lowered as a result of decoupling biomass from the water which carries it (Javid, Hassani, Ghanbari, and Yaghmaeian, 2013). Converting old treatment plants from

CAS-based to MBBR-based could allow plants to increase their treatment capacity and diversify their treatment capabilities (Mannina and Viviani, 2009; Falletti and Conte, 2007).

The plastic media for use in a moving bed biofilm reactor has been improved upon for over a generation now, with the technology being implemented in facilities since the 1990s (Phillips et al., 2010). It has proven to be a robust technology for effective treatment of wastewater. However, we propose that there are some ways in which the technology could be improved upon further. The plastic media that is typically used in a moving bed biofilm reactor is often produced via plastic extrusion methods. The plastic extrusion process, which will be explained in more detail in **Section 3**, limits the design of media to a two-dimensional cross-section. This prevents the utilization of a third dimension for designing more complicated but possibly more efficient designs. These two-dimensional designs target maximizing surface area, but not all of the surface area that is present on the carriers is ideal. As seen in **Figure 1-3**, these carriers contain surface on both the inside and outside. Only the biofilm that forms on the inside of the carrier will be protected from abrasive

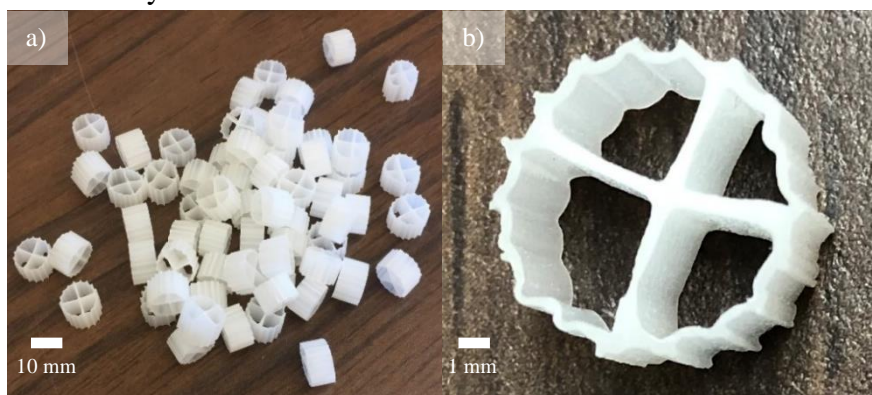


Figure 1-3: Example moving bed biofilm reactor media, Kaldnes K1

forces, limiting the amount of effective surface area. Biofilm that does form on these surfaces will likely slough off. While this can also act to remove older biomass, it does so in an uncontrolled manner. Additionally, the carriers themselves, which will collide frequently during operation, will incur

abrasive forces, which have the potential to damage the carriers.

In this thesis, we explore the idea of using additive manufacturing to 3D print architected biofilm carriers to promote a better platform for biofilm growth than conventional methods. We hope to explore the role of architecture, rather than surface area, in optimizing biofilm. 3D printing allows for a much more open design space than allowed by conventional manufacturing methods. Due to advances in the field in recent years, more complicated architectures can be designed and constructed. This makes it possible to experiment with new designs of biofilm carriers that were not previously possible. It is our hope that we can develop new architectures that are better suited to growing biofilm than conventional carriers. In this work, various architectures were explored to see which are better suited for growing biofilm. Additionally, the treatment performance of this biofilm was also assessed. Variables such as strut size, strut configuration (topology), and strut density (unit cell density) were explored. These architectures are compared with an equal volume of conventional carriers subjected to the same conditions. With the added design freedom allowed by 3D printing, design can be focused on optimizing a biofilm carrier for its purpose of improving treatment efficacy and maximizing biofilm. Therefore, the architecture of a biofilm carrier was

explored using 3D printing for the purpose of optimizing the biofilm for treatment goals as well as biofilm structure.

1.1 Objectives and Hypotheses

- **Hypothesis 1.** Different architectures will yield different biofilm structures to form on different 3D-printed architected biofilm carriers.
 - **Objective 1a.** Qualitatively assess biofilm formation patterns on various architectures using visual microscopy.
 - **Objective 1b.** Quantify biofilm volume that forms on 3D printed architectures by using microCT technology to assess biofilm volume patterns quantitatively and visually.
- **Hypothesis 2.** 3D printing can be used to develop architected biofilm carriers that can achieve a biofilm that yields better removal of ammonia and COD for use in a wastewater treatment setting. Additionally, the communities of bacteria that form on these carriers can achieve enhanced biofilm performance beyond those of conventional, non-architected carriers.
 - **Objective 2a.** Conduct a flow-through study to demonstrate the ability of the 3D printed architectures to remove both COD and ammonia and compare this removal to the conventional carriers.
 - **Objective 2b.** Conduct a batch study to assess the biofilm performance on each of the biofilm carriers, both conventional and 3D printed, and compare them.

2. Factors Affecting Biofilms in a Wastewater Treatment Setting

Biofilms have the potential to improve wastewater treatment. The idea of using biofilms in wastewater treatment is not inherently new, and it actually predates the conventional activated sludge process. Trickling filters were discovered and installed municipally starting in 1910 (Hammer and Hammer, 2012). The process involves running wastewater over inert media, such as rocks, to promote biofilm to grow and treat the water. It is an easy to operate system but can lead to large sludge generation and clogging (Sehar and Naz, 2016). Several other biofilm-based treatment systems have since evolved. Another process is the rotating biological contactor. This process involves a large disc that is partially submerged in wastewater. The disc rotates into and out of the wastewater, providing both media exposure and aeration. The system offers reduced life cycle costs, less sludge production, less space requirement, ease of operation, and high process stability, but can be difficult to adapt to different environmental and influent conditions (Sehar and Naz, 2016). The process can also be optimized by increasing both rotation speed (Szulyzyk-Cieplak, Tarnogorska, and Lenik, 2018) and contact time (Szulyzyk-Cieplak et al., 2018; Rana, Gupta, and Rana, 2017). Finally, and more recently, another method of biofilm-based treatment is the moving bed biofilm reactor.

In recent decades, the moving bed biofilm reactor (MBBR) has been established as a robust method of using biofilm to treat wastewater, with growth in popularity of the technology since the 1990s (Phillips, Steichen, and Johnson, 2010). This is a retrofit solution that allows media to be added to existing processes to modify the process. In addition to intensifying the process overall (Phillips et al., 2010), they can provide diversified treatment, allowing for the removal of different substrates. Biofilms have been found to be more efficient at removing chemical oxygen demand (COD), nitrogen, and phosphates (Naz et al., 2015). MBBR systems involve placing small plastic media into a reactor, such as an existing aeration basin, to take advantage of bacteria's desire to form biofilm. The media are designed to have high surface area to volume ratios to promote maximum biofilm formation (Ødegaard, Rusten, and Westrum, 1994). The biofilm then treats the wastewater by removing BOD, among other contaminants present in wastewater (Phillips et al., 2010). This media can be readily adapted to the conventional activated sludge processes by retrofitting the existing infrastructure. MBBRs have been shown to allow for BOD removal, nitrification, and denitrification to occur by utilizing different reactors within a treatment scheme (McQuarrie and Maxwell, 2003). The system can also allow for operational control, in terms of what treatment occurs (Steichen et al., 2009). Additionally, MBBR technology retains its biomass better than suspended-based systems, making them more resistant to wet-weather events that could potentially wash out bacteria (Phillips et al., 2010). The HRT can also be lowered as a result of decoupling biomass from the water which carries it (Javid et al., 2013). Converting old treatment plants from CAS-based to MBBR-based could allow plants to increase their treatment capacity and diversify their treatment capabilities (Mannina and Viviani, 2009; Falletti and Conte, 2007).

The biofilm that forms on these carriers is composed of bacteria. Most bacteria present in a wastewater treatment setting are mesophilic, meaning they prefer temperatures of 10-45° C (Rittmann and McCarty, 2001a). These bacteria also thrive best when the pH is neutral (Mladenovic, Muruzovic, and Comic, 2017; Rittmann and McCarty, 2001a; Sehar and Naz, 2016). Two common contaminants that have to be removed from wastewater influent are biological and/or chemical oxygen demand (BOD/COD) and ammonia. The ratio of carbon to nitrogen (COD/N) has a direct effect on the types of bacteria that can form within a biofilm. High COD/N ratios lead to more competition between heterotrophic bacteria and autotrophic ammonia oxidizing

bacteria (AOB) (Bassin et al., 2015). Despite this competition, operating at a high COD/N ratio initially may be conducive to the success of autotrophic bacteria in the long term. Heterotrophic bacteria excrete more EPS than autotrophs, and therefore form biofilms faster. By starting with these heterotrophic bacteria, then removing the carbon source by lowering the COD/N ratio, autotrophic bacteria can colonize the biofilm and offer better ammonia removal than if the system had been without carbon all along (Bassin, Kleerebezem, Rosado, van Loosdrecht, and Dezotti, 2012). Additionally, the hydraulic retention time seems to play a larger role in ammonia removal, with longer HRTs leading to more nitrification, than in BOD and COD removal (Hamoda and Al-Sharekh, 2000).

2.1 Design Considerations of Biofilm-Based Wastewater Treatment

Biofilm-based systems are a potential enhancement to the conventional activated sludge process. However, because they utilize biofilms rather than suspended biomass, the design considerations are a bit different. Carriers have to be designed such that they promote attachment of biomass to the surface of the carrier. The specific surface area, a , is a measure of how much surface area per unit volume is provided by a carrier. When multiplied by the total volume of the reactor, the biofilm surface area is obtained (Rittmann and McCarty, 2001b). Increasing the surface area of the biofilm provides the biofilm with more access to the bulk liquid, allowing the bacteria at the biofilm's surface to conduct treatment. Another factor affecting the performance of biofilms is the thickness (L_f) and density (X_f) of the biofilm. When multiplied together, these values give the biomass per area of biofilm (Rittmann and McCarty, 2001b). These are important because thicker and denser biofilms are more susceptible to becoming mass transport limited as diffusion is diminished.

Another important design consideration is the amount of oxygen that is provided to the biofilm. Heterotrophs and ammonia oxidizing bacteria are aerobic organisms and therefore need oxygen in order to process and remove ammonia and BOD. The oxygen must not be the limiting reagent in the microorganisms' metabolism, otherwise biodegradation rates will slow, leading to poor sludge settling and odors (Rittmann and McCarty, 2001e). Therefore, it is important to ensure that oxygen is always provided in excess to the wastewater. The rate flux of oxygen to the liquid is rate-limiting compared to that of the gas to the gas-liquid interface (Rittmann and McCarty, 2001e). Efficient transferring mechanisms are important to ensure that the oxygen is able to get to the water and not simply pass through and re-enter the atmosphere. Fine bubble diffusion leads to better transfer efficiency than course bubble diffusers (Schlegel and Koeser, 2007). However, the course bubbles are better for preventing clogging of the system, as they make for better mixers. (Schlegel and Koeser, 2007).

Another design consideration is the solids retention time (SRT) to be employed. The SRT needs to be sufficiently long such that bacteria in the biofilm can grow and conduct required removal of COD and ammonia. If assuming a steady state biofilm, in which the growth and decay rate over the whole biofilm is, on average, equal, the SRT is simply the inverse of the detachment rate of the bacteria (Rittmann and McCarty, 2001b). This means that if the detachment rate of bacteria from the biofilm is to be increased, the SRT will become shorter. This detachment rate of bacteria, b' , is positively related to the shear stress present within the bulk liquid (Rittmann and McCarty, 2001b), meaning that more shear will lead to more detachment and subsequently, a shorter SRT.

Shear is important to control because it can have a direct effect on the performance and characteristics of the biofilm. Shear will always cause some bacteria to be removed from a biofilm. However, constant shear can lead to a smooth biofilm that is both thinner and denser, while inconsistent shear can lead to uneven, thick, and less dense growth that is then sloughed away in the presence of shear. (Yang, Cheng, Li, Sun, and Huang, 2019; Ai et al., 2016). Additionally, the shear has an effect on the roughness of the biofilm itself, with smoother biofilms forming under high shear conditions and rougher biofilms forming under low shear conditions (Cowle et al., 2019).

2.2 Carrier Consideration and their Effects on Performance

2.2.1 Biofilm Thickness

Biofilm thickness also seems to play a role in how biofilms are affected. Novel Z-carriers have been invented that for the ability to select for biofilm thickness. These carriers have grid-like indentations that allow biofilm to form within them. The walls of these grids are a fixed height, such that the biofilm that forms within the grids is protected from abrasion. These carriers allowed for the effect of biofilm thickness on the biofilm itself to be studied. It has been found that thicker biofilms allow for higher specific biotransformation rate constants (Toressi et al., 2016), as well as having higher richness and evenness (Suarez et al., 2019). It was also found that thinner biofilms seem to be better suited for nitrification (Toressi et al., 2016; Suarez et al., 2019). Finally, different thicknesses led biofilms with different compositions of species, suggesting a preference for either thick or thin biofilm (Suarez et al., 2019).

2.2.2 Material Properties' Effects on Biofilm Development

The material chosen for use in a biofilm-based reactor has been shown to influence the biofilm that ultimately forms on the carrier. This effect is in addition to whatever effects the local environment is also having on the biofilm. Therefore, it is important that the design engineer understands how the chosen carrier might influence the biofilm that later develops on the carrier. Having carrier materials does seem to improve removal characteristics compared with having no carrier materials. This was demonstrated in a study by (Li, Li, Lee, Mok, and Hao, 2019), where nitrogen removal in a reactor packed with luffa sponge, polyurethane foam, or nothing, was 78%, 71%, and 62%, respectively. In another study by (Naz et al., 2015), it was demonstrated that using stone media as a carrier, as opposed to no carrier, improved removal of BOD, COD, nitrites, nitrates, and phosphates. However, lower sulfate removal was seen. Many carriers chosen for bacteria development are plastic based. Specifically, polypropylene seems to promote the best biofilm development in several studies conducted (Felfoldi et al., 2015; Sonwani, Swain, Giri, Singh, and Rai, 2019; Jurecska et al., 2012). In a study targeting limiting biofilm growth, it seems that titanium and titanium-alloy seemed to not allow biofilm growth, while steel did (Kim, Kim, and Hwang, 2012). Sections 2.3 and 2.4 will outline in more detail some of the properties and characteristics of materials and their surfaces that influence biofilm adhesion.

2.2.3 Surface Characteristics' Effects on Biofilm Development

In addition to material, the surface properties of the material also have an effect on the biofilm that forms. Surface properties become very important to bacteria during the initial adhesion stages of biofilm formation. One of the most important surface properties is how rough the surface

of attachment is. Bacteria seem to adhere better to rougher, sand-blasted surfaces than smooth surfaces (24-34 μm) (Cox et al., 2017). Smooth surfaces, such as those polished with diamond polishing paste in dentistry, seem to have the lowest biofilm formation, with a scale ranging from 0.5-0.7 μm (Kurt, Cilingir, Bilmenoglu, Topcuoglu, and Kulekci, 2019). Biofilm formation also seems to positively correlate with the surface roughness of a material at the scale of 0.1-19.8 μm (Kim, Ravault, Han, and Kim, 2012; Bolton, Tummala, Kapadia, Dandamudi, and Belovich, 2006). This roughness effect seems to play a larger role in biofilm formation than shear forces (Cowle, Webster, Babatunde, Bockelmann-Evans, and Weightman, 2019), although this particular study only explored a very small range of shear. Surface wettability, topography, presence or absence of crevices or corners, and surface modification can all also play a role in biofilm formation (Sarjit, Tan, and Dykes, 2015). Positive surface charges also seem to be more conducive to biofilm adhesion (Sun, Ding, Xi, Lu, and Yang, 2019; Siddique, Suraraksa, Horprathum, Oaew, and Cheunkar, 2019). Hydrophilic surfaces seem to be conducive to early biofilm adhesion (Saeki, Nagashima, Sawada, and Matsuyama, 2016; Siddique et al., 2019) but seem to have less significant effect as the biofilm propagates (Saeki et al., 2016).

3. Manufacturing

3.1 Additive Manufacturing and Architected Materials

Additive manufacturing (AM) has emerged in recent years as a means of bridging designs that are conceivable with designs that are actually possible to manufacture. 3D printing has allowed for the field of architected materials to become realized. The field of architected materials is the idea that materials and their methods of manufacture can be designed around their intended use, rather than designing the use to suit what materials and manufacturing methods are available (Ashby, 2012). Materials can have their characteristics modified by modifying their chemistry, microstructure, and architecture. According to (Fleck, Deshpande, and Ashby, 2010), chemistry and microstructure were exhausted during much of the 20th century. However, architecture remains an unexplored frontier due to the limited means by which man has been able to influence architecture on a small scale. Architected materials act as the bridge between superstructure and microstructure. Additionally, because the entire structure is designed for the end use, including both material properties and its architecture, rather than compromising for manufacturability, maximum efficiency of the part can be achieved (Brecht and Embury, 2012). 3D printing is the mechanism by which this unlimited design space can be achieved.

The market has been growing in recent years, making it more readily accessible to industries and people that previously would have had limited to no access. There has been a continual growth in the AM market, with it being a \$6.1 billion industry in 2016, and a \$7.3 billion industry in 2017 (Gutierrez-Osorio, Ruiz-Huerta, Caballero-Ruiz, Siller, and Borja, 2019), with an estimated 20% growth annually between 2017 and 2020 (Hettesheimer, Hirzel, and Roß, 2018). In this study, the field of AM is explored to provide an overview of 3D printing techniques.

There are several exciting advantages that 3D printing offers over traditional manufacturing methods. One advantage is design freedom. Because of the additive nature in which material is added during construction, there are very little physical constraints to what can be built (Pearson, 2018). Conversely, processes such as injection molding require a mold to construct the part. This would make it much more time and effort consuming to remove the mold in a design where the plastic totally encased the mold. Therefore, designs built using this and other conventional methods require the designer to consider the needs of the method when designing their parts. 3D printing does not have this limitation, and therefore highly complex geometries are possible. An example of a lattice cube is shown in **Figure 3-1**. Such a geometry would be difficult to construct via traditional methods due to the lattice structure that reaches all the way into the center of the cube.

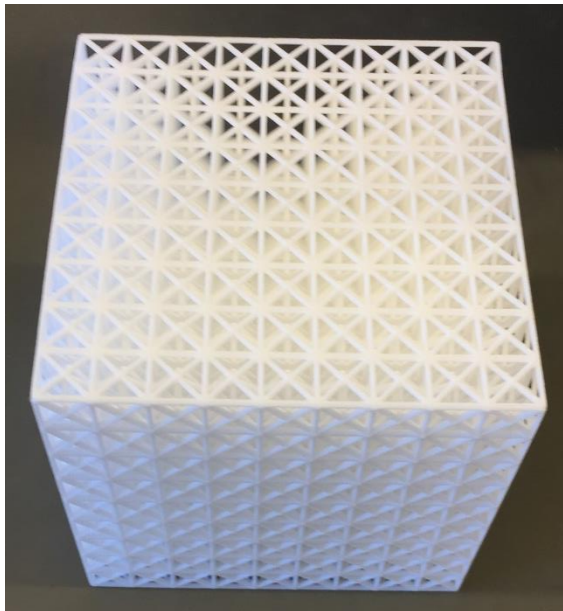


Figure 3-1: 3D printed cube (Octet + Simple Cube, 0.6 mm)

3D printing can also allow for rapid prototyping and changes to be implemented before a final design is reached. In traditional methods of

manufacturing, such as injection molding, whenever a change in design is made, experienced machinists must retool the mold, which can be costly and time-consuming (Pearson, 2018). However, 3D printing just requires the CAD design to be modified. The settings of the 3D printer would not require adjustments. A lattice plate designed with 3D printing can be seen in **Figure 3-2**. This plate was designed for flexural testing in 3-point bending. The lattice network would have been difficult to create without 3D printing, and the process also allowed for the easy addition of supports for use during testing. In addition to the ability to implement changes during prototyping, it is also well suited for industries where individualized parts are required. In industries like the medical industry, where parts such as prosthetics or ankle-foot orthoses (Wojciechowski et al., 2019) are needed, every patient has requirements that are unique to them. It would not be logical to design a mold for each patient's needs. Therefore, 3D printing allows these single-use products to be manufactured once and then redesigned, without adding any cost other than the cost of printing another part.

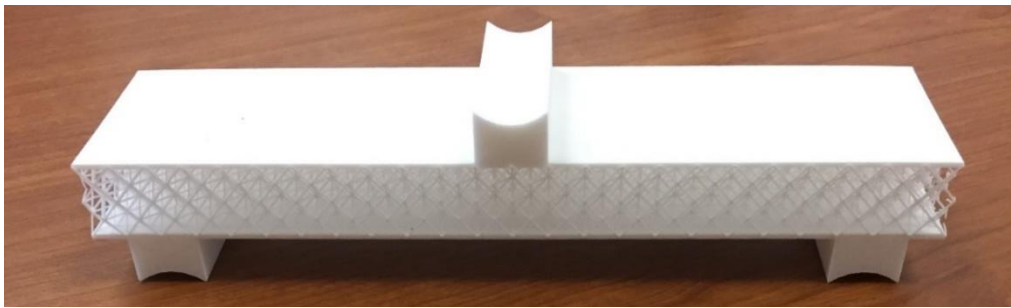


Figure 3-2: Octet sandwich plate designed for structural testing in 3-point bending

3D printing also has the potential to be both cost-effective and fast when compared with traditional methods of manufacturing, such as injection molding (10 Advantages of 3D Printing, 2019; Pearson, 2018). Injection molding is expensive to set up (Peng, Kellens, Tang, Chen, and Chen, 2018). However, once set up, it is cheap to produce parts quickly. The more plastic parts that are manufactured using the same mold, the more payback and profit that will be had. Printing a few parts via molding would be cost-prohibitive. Because 3D printing does not need time to setup a complicated mold, the parts can be made quickly, with the time required to print being the only time constraint. This allows quick turnaround times for parts that are needed within a few days, rather than waiting weeks for molds to be created via traditional methods. Additionally, additive manufacturing leads to very little waste of material. Typically, only material that is needed for printing is used to manufacture a part. Powder-based methods of 3D printing are also capable of reusing powder that was not used for making the part, allowing most of the material to be reused.

3D printing on a very small scale, such as micro and even nano, has allowed for a whole new field of materials research to present itself. As structures are designed on a very small scale, rather than just at the macro scale, the properties of materials can actually be changed. **Figure 3-3** shows a geometry that was designed using another lattice design. Normally, when an object is subjected to a force such as compression, the object undergoes some sort of deformation in both its lateral direction (parallel to the force) and its longitudinal direction (perpendicular to the force). The ratio of the two is a material's Poisson's ratio. This value is almost always positive and is usually between 0.25 and 0.33 (Philpot, 2013). Most materials have positive ratios, meaning that if one axis experiences expansion, the other must experience shrinkage. However, the lattice in **Figure 3-3**, when subjected to compression on the top and bottom, experiences shrinkage along both axes, leading to a negative Poisson's ratio. This is important because it allows materials

designed at the micro scale using 3D printing to exhibit properties that have never been exhibited using conventional materials or methods of manufacture.

Lattice architectures have opened up new avenues in terms of mechanical and multifunctional properties which were not available in the past. Although advances in AM and metamaterials have reached immense progress, there has not been a true connection between metamaterials and civil infrastructure. One of the research groups aiming at that goal is the Gerasimidis research group at UMass. The research efforts of this group inspired by past research on progressive collapse of building structural systems (Song et al., 2018; Pantidis and Gerasimidis, 2018; Gerasimidis, Khorasani, Garlock, Pantidis, and Glassman, 2017; Sideri, Mullen, Gerasimidis, and Deodatis, 2017; Pantidis and Gerasimidis, 2017; Gerasimidis, Deodatis, Yan, and Ettouney, 2016; Gerasimidis and Sideri, 2016; Stavridou, Efthymiou, Gerasimidis, and Baniotopoulos, 2015; Gerasimidis and Baniotopoulos, 2015; Gerasimidis, Kontoroupi, Deodatis, and Ettouney, 2014; Gerasimidis, 2014; Gerasimidis, Bisbos, and Baniotopoulos, 2013; Gerasimidis, Bisbos, and Baniotopoulos, 2012; Gerasimidis, Ampatzis, and Bisbos, 2012; Gerasimidis and Baniotopoulos, 2011a; Gerasimidis and Baniotopoulos, 2011b) has studied the effect of defects in truss-lattice architectures of architected materials (Gross, Pantidis, Bertoldi, and Gerasimidis, 2019). Another aspect of connecting metamaterials to infrastructure is through plate lattice structures and the group's work on shells is the first step towards exploring this option (Gerasimidis, Viot, Hutchinson, and Rubinstein, 2018; Yadav and Gerasimidis, 2020a; Yadav and Gerasimidis, 2020b; Yadav and Gerasimidis, 2019). The current work is part of this research group's efforts to bring AM and architected metamaterials into civil infrastructure and utilize the unprecedented potential in this case to improve wastewater treatment facilities.

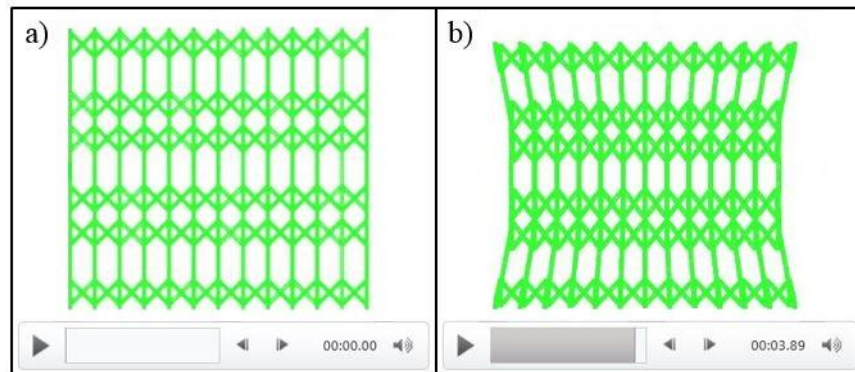


Figure 3-3: Lattice structure with a negative Poisson's ratio. a) Before compression starts. b) After compression is complete. Note the negative Poisson's ratio that occurs as both the sides and the top and bottom are inwardly compressed.

AM can also allow for very lightweight parts to be manufactured. Because 3D printing can allow for complicated designs, it is possible to design parts that are highly efficient, with only as much material as necessary being used. Additionally, the material that is used can be organized in a highly efficient manner. This can allow for strong, lightweight structures to be manufactured. These structures can be constructed to withstand the shear forces that will be imposed by moving water in a wastewater treatment plant. As visualized in **Figure 3-4**, a metal lattice plate was constructed that was actually light enough to be placed on top of a dandelion, yet strong enough to retain its structure.

Finally, AM has also allowed for the creation of materials that can actually react to some environmental response, such as light, temperature, or some other variable (Zafar and Zhao, 2019). These materials can be designed by using “smart materials”, which are materials that respond to environmental conditions by expanding or contracting (Zafar and Zhao, 2019). Based on where materials connect, this movement causes the whole structure to achieve specialized motions, such as folding into a cube for transportation and unfolding after reaching a destination.

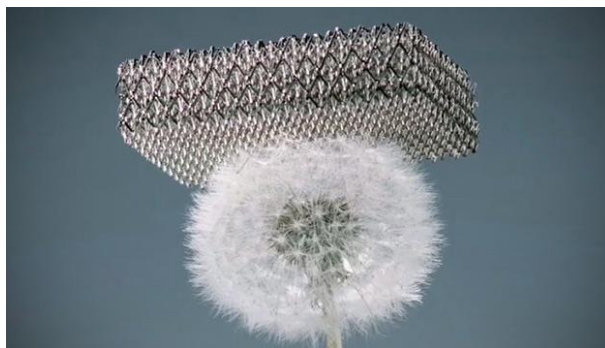


Figure 3-4: A metal lattice plate that is light enough to sit on a dandelion

Generally, the topics of cost, energy efficiency, and quality of 3D printing are discussed in the following sections. However, selective laser sintering was ultimately chosen as the method used for printing our carriers. Therefore, an in-depth description is only given for selective laser sintering in its own section. Finally, we conclude with a section of the conventional biofilm carriers chosen for comparison in our study, which were carriers for a moving bed biofilm reactor.

3.1.1 Cost of Additive Manufacturing

Additive manufacturing can offer reduced costs over traditional manufacturing in certain conditions. While both have their applications, 3D printing is well-suited for niches where traditional manufacturing is not appropriate. The unit price of the material used and the initial investment into the 3D printer itself are the main drivers of the cost of 3D printing (Yang and Li, 2018). Additive manufacturing can also offer less wasted material than conventional manufacturing. For example, while fused deposition modelling was found to only waste 12.8% of material, injection molding was found to waste 18% of material (Franchetti and Kress, 2019). Material volume used during printing and the time it takes to print a part are the two operating costs associated with additive. Therefore, designing parts to minimize support material volume is important. Additionally, minimizing the surface area of the printed part itself, without compromising its ability to perform its function, will also reduce print time, which equates to cost savings. Minimizing both of these variables can lead to optimized print designs (Sabiston and Kim, 2018).

AM suits itself better to smaller lot runs, as the unit cost to produce a part is fixed and based on the price of the material. Conventional manufacturing is better suited for large lot runs, as it is expensive to reconfigure the process for different types of parts but is cheap to operate once the process is configured. The point where one process becomes cost effective over the other varies based on the part design, but in one study it was about 200 units (Franchetti and Kress, 2019). 3D printing offers faster lead times, as there is little preparation work needed to print a part once an STL file exists (Westerweel, Basten, and van Houtum, 2018; Emelogu, Marufuzzaman, Thompson, Shamsaei, and Bian, 2016). Many 3D printers have the capability to print multiple parts at once during a single build. This can reduce the operating costs associated with 3D printing, as single prints can be combined rather than manufactured separately. Printing multiple geometries within a single build can lead to cost savings of up to 26%, depending on the specific variables of the geometries to be printed (Yang and Li, 2018). Additive manufacturing also allows for a

customizable product to be manufactured (Emelogu et al., 2016), which lends itself well to industries like the medical industry where every patient requires a unique experience.

There are many types of 3D printers that all work on their own principles. Three of these are fused deposition modelling (FDM), selective laser sintering (SLS), and multi-jet fusion (MJF). All of these printers are capable of using polyamide 12 as a material, which is a nylon type. By using the same material, the costs of printing were able to be compared between the three printers. In a study looking at a variety of part types, it was found that the selective laser sintering printer had the cheapest cost per part, while the FDM printer had the highest cost per part. The SLS and MJF are both capable of producing multiple parts at once, while the FDM is not. Finally, the SLS printer was the most profitable for 3 of the 6 parts produced, but it also has a long recovery time due to its high investment cost (Tagliaferri, Trovalusci, Guarino, and Venettacci, 2019).

3.1.2 Energy Efficiency and Environmental Impacts of Additive Manufacturing

Additive manufacturing offers a much higher material reuse fraction than conventional manufacturing. According to (Hettesheimer et al., 2018), up to 70% of the materials used in manufacturing can be saved by switching from conventional manufacturing to additive manufacturing. Theoretically, it is said that additive manufacturing has the potential to be up to 91% material efficient, but in practice, this efficiency is typically lower as some of the powder becomes non-reusable. Additive manufacturing also offers the potential for up to 90% waste reductions when compared against some conventional, or traditional, manufacturing processes. (Peng et al., 2018).

However, there is a lot of electricity use associated with additive manufacturing. In order from most environmental impact to least environmental impact, four printers were ranked: HP JetFusion 3D (MJF), sPro60 HD (SLS), EOS P396 (SLS), and Fortus 450mc (FDM). This was primarily based on the electricity usage during printing of each of these printers. Specific energy consumption during printing may be a function of layer thickness, with thicker layers yielding more specific energy consumption (Tagliaferri et al., 2019). In a particular study, three methods of 3D printing were explored, and the order of specific energy consumption of the three methods, in increasing order, was material jetting, vat photopolymerization, and material extrusion (Gutierrez-Osorio et al., 2019).

There is also a high energy consumption of the raw materials themselves, adding to overall energy use (Tagliaferri et al., 2019). Electricity is used at every step of the way in additive manufacturing, from material generation to post-creation (Nagarajan and Haapala, 2018). However, this use of energy can be offset by the lack of wasted material that is used by additive manufacturing when compared with conventional manufacturing (Walachowicz et al., 2017). In fact, AM could reduce the total primary energy demand of manufacturing by about 5% by 2025 in the industrial sector (Walachowicz et al., 2017). The type of additive manufacturing that occurs also affects how much of the energy is wasted. For direct metal laser sintering, only 10% of the energy input contributed to material processing, while 90% of the energy was lost as bulk waste, heat, and work. For fused deposition modeling, 7% of the energy input contributed to material processing, while 93% was lost. (Nagarajan and Haapala, 2018). 3D printing has the potential to be environmentally friendly. Because the energy demand of additive manufacturing is tied so strongly to electricity use, this method can become environmentally friendly if the source of electricity is of a renewable form (Walachowicz et al., 2017; Nagarajan and Haapala, 2018).

3D printing has the potential to be less harmful in terms of the fate of the waste plastics, as most of the plastics that are used are non-toxic. However, these powders are usually in a powder form, so care must be taken to ensure that they do not become aerosolized in an unvented environment (Peng et al., 2018). However, the toxicity of materials is still being explored. In a study of fused deposition modelling, three common filaments used in fused deposition modeling were studied: polyactic acid (PLA), acrylonitrile butadiene styrene (ABS), and polyethylene terephthalate glycol-modified (PETG). PLA is generally considered to be the most eco-friendly and sustainable option, but limited research suggests that this may be offset by the resources needed to produce its source crops. Additionally, all three filaments produce volatile organic compounds and ultrafine particles that may lead to skin, pulmonary, and mucosal irritation. Generally, it is concluded that more work is needed to create health and safety data sheets that are more universal and available for users to have a better understanding of material properties. In addition to this, more regulation regarding transparency from the manufacturers is needed due to the proprietary nature of how the materials are made (Banashek, 2019).

3.1.3 Quality of Additive Manufacturing

Process variables during building can affect the overall print quality of a 3D printed part. AM can be used to 3D print medication. It was found that printing chamber temperature, laser scanning speed, and lactose monohydrate concentration all had effects on the qualities of the printlets. These qualities were weight, hardness, disintegration time, and dissolved drug fraction in 15 min. It was found that the printlets had a porosity of about 37.89%. Additionally, chemical images suggested uniform distribution of the drug. The results of this study suggested that SLS could provide a viable method of printing drugs for personalized medications in a pharmacy or hospital setting (Barakh et al., 2019).

The method of 3D printing does not seem to affect the strength of the part. In a study, three different techniques of 3D printing were explored: material extrusion (ME), vat photopolymerization (VP), and material jetting (MJ). The materials identified for each technique were PC® for ME, RIGUR RGD450® for MJ, and DL260® for laser-based VP. These materials were chosen such that their mechanical properties were similar. These materials were 3D printed into coupons and tested for their tensile strength by conducting tensile tests, and it was found that they all did in fact contain similar mechanical properties, which was defined as being within 10% of each other. This suggests that all three 3D printers were capable of producing parts that lived up to their mechanical expectations and could perform similarly (Gutierrez-Osorio et al., 2019).

In a study by (Borisenko et al., 2019), a proposed improvement to SLS using metals is described. The paper claims that some drawbacks of the process itself are the need for powder quality of a certain sphericity, particle size distribution, and conditions of their production and storage. Additionally, because each layer is formed by adding material in layer thicknesses at the micron level, a final product of high porosity is obtained. This has the potential to be unacceptable, depending on what the metal's final task is to be. This article proposes using an electrical arcing technique to weld metal together in an additive way. It was found that the print speed could be improved and the porosity reduced to near zero using this method over regular metal SLS (Borisenko, Borisenko, Zhokhov, Redkin, and Kolesnikov, 2019).

There is a tradeoff between fast printing and a higher degree of accuracy. Typically, conventional processes can achieve higher accuracy than 3D printing. Combining the two can allow one to combine the benefits of additive manufacturing, such as reduced waste, with the

benefits of conventional manufacturing, such as higher accuracy (Jackson, Asten, Morrow, Min, Pfefferkorn, 2018). Additionally, there are tradeoffs within 3D printing itself. Nano-scale printing is more accurate than macro-scale printing, but nano-scale printing cannot print large objects. However, high-precision 3D-printing via two photon absorption, allows the bridging of both macro- and nano-scale printing (Stender et al., 2019). This technology is a method of 3D lithography. This technology allows for switching between 3D lithography for high precision nano-prints and bath 3D lithography for larger, less precision parts (Stender et al., 2019).

3.1.4 Selective Laser Sintering Process – an Overview

Selective laser sintering (SLS) was the method of 3D printing that was conducted in this research. The printer used was an EOS Formiga P110 3D Printer. This printer was chosen because it was readily available for printing in the UMass Amherst Advanced Digital Design and Fabrication (ADDFab) Core Facility. It has an advertised build volume of 200 mm x 250 mm x 330 mm and a layer resolution of 0.100 mm (Advanced Digital Design and Fabrication (ADDFab): Core Facilities: UMass Amherst, n.d.). In our study, we used a polyamide, nylon powder, PA 2200. This material was chosen for its high strength and stiffness, high detail resolution, and its bio compatibility. Additionally, this material was readily compatible with the EOS Formiga P110 3D-printer. Finally, all models for 3D printing were designed using AutoCAD (Autodesk®, AutoCAD 2018). Files were then exported as stereolithography (STL) files for manufacturing. Because the SLS process was used in this study, we will focus on this method of additive manufacturing for the remainder of this thesis. Additionally, we will provide a detailed overview of this process.

The selective laser sintering process (SLS) uses lasers to “sinter” powder together to form a solid object. A schematic of the process is shown in **Figure 3-5**. Prior to beginning on the machine, a model must be designed and exported as an STL file, which is comprehensible by the SLS printer. The chamber in which the object is 3D printed is heated to just below the melting point of the powder (Wellington, 2014). This powder can be metallic (Hettesheimer et al., 2017), plastic, glass, or ceramic (Wellington, 2014), depending on the system. The system consists of a laser, which performs the sintering, a mirror, which directs the laser beam, a movable platform, which houses the object, and a levelling roller, which brings in new powder. The object is created layer by layer in this system. First, the levelling roller spreads new powder across the movable platform. The laser then sinters the powder along the movable platform in the areas of the current layer of the object in which solid object is desired (Hettesheimer et al., 2017). This laser is controlled by the computer. It is directed at the platform, and traces cross-sections of the designed object at each slice of the object (Wellington, 2014). These particles of powder fuse into the first layer of the object. The platform is then lowered and cooled. The distance that this platform is lowered is the resolution of the machine. For example, if the platform lowers 0.1 mm, it will have a 0.1 mm resolution (Wellington, 2014). The process then repeats by sintering the next layers until the object is fully constructed (Hettesheimer et al., 2017).

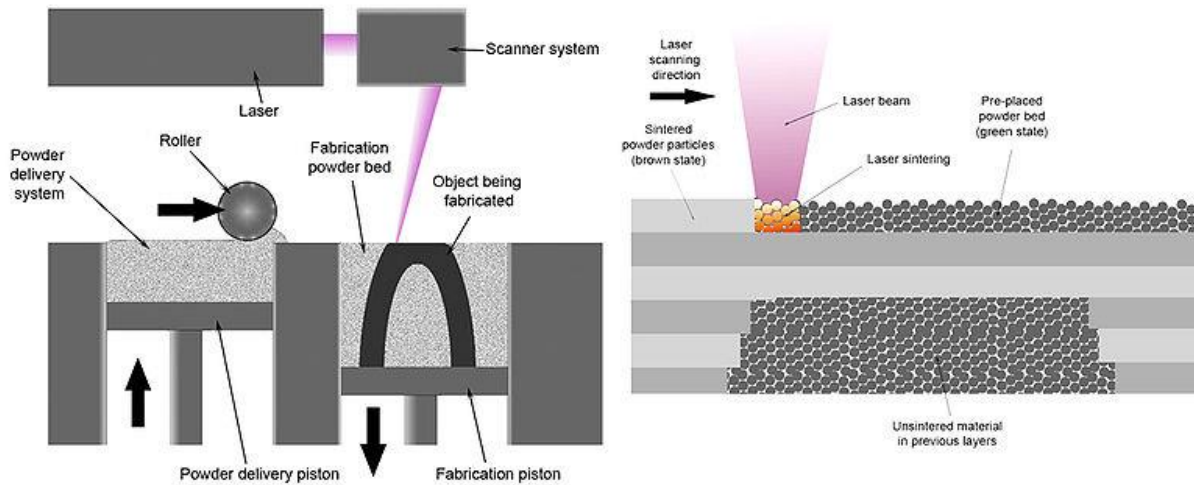


Figure 3-5: The selective laser sintering process. This schematic shows the selective laser sintering system. (Image credit: Materialgeeza/Creative Commons) (From Palermo, 2013)

After the part is fully printed, it will still be encased in the unsintered powder. Therefore, it must be cleaned before it can be used. This is typically done at a cleaning chamber using compressed air or a media blaster (Guide to Selective Laser Sintering (SLS) 3D Printing, n.d.). If the part is more fragile however, a gentle cleaning method, like washing with hot, soapy water or alcohol, may be better (Five Things to Consider When Cleaning Your SLS Prints, 2017). The parts will have a slightly rough grainy surface finish similar to medium grit sandpaper. The part is also very porous, which may allow dust and bacteria to be trapped (Five Things to Consider When Cleaning Your SLS Prints, 2017). Post-processing is needed if a smoother surface finish is necessary. The excess remaining powder can then be filtered to remove larger particles. The used powder, which is now slightly degraded from used, can be recycled with new powder for further printing (Guide to Selective Laser Sintering (SLS) 3D Printing, n.d.).

Selective laser sintering has some important advantages over other methods of additive manufacturing. SLS technology does not require a support material (Wellington, 2014; Dimensional accuracy of 3D printed parts, n.d.). Because the part is submerged within the powder during its sintered construction, the unsintered powder acts as the support for the material. Additionally, the lack of support material allows for even more complex, previously difficult to construct geometries, such as interlocking or moving parts and parts with interior components, to be 3D printed.

While selective laser sintering can have a resolution of 0.1 mm, its accuracy is typically around ± 0.3 mm (Laser Sintering Accuracy Study, n.d., & Dimensional accuracy of 3D printed parts, n.d.). This value is the lower limit of the accuracy. Quality control can be implemented to ensure part accuracy. One study found that 95% of 1859 data points were within ± 0.35 mm of nominal (Laser Sintering Accuracy Study, n.d.). At larger dimensions, this can be $\pm 0.3\%$ of the total dimension length. Additionally, there is the potential for both warpage and shrinkage when one area of the part is exposed to high heat temperature, while printed areas are allowed to cool somewhat. Shrinkage can occur in the range of 2-3%, but most SLS print providers can account for this in their design (Dimensional accuracy of 3D printed parts, n.d.). Due to its versatility, the

technology is well-suited for printing the proposed geometries to be studied later in this thesis for the purpose of assessing biofilm formation.

3.2 Conventional Biofilm Carrier Technologies

3.2.1 Moving Bed Biofilm Reactor (MBBR) Technology

Moving bed biofilm reactors (MBBR) have proven to be a robust technology for growing biofilms. Generally, effective mixing and aeration with a good carrier can lead to good performance with low-maintenance requirements (Wang et al., 2019). For our study, we chose to use the moving bed biofilm reactor (MBBR) as our comparison for our 3D printed biofilm carriers. This technology is relatively new, and it is becoming very popular in new installations utilizing biofilm technology (Phillips et al., 2010). Our goal was to use this technology as a benchmark for the 3D printed carriers, not to improve upon the design of the MBBR itself. Therefore, we only chose one technology to use for comparison in our studies. The MBBR technology lent itself well to a lab-scale study, as its volume could easily be scaled up or down based on how much media you choose to use. In our case, we chose to use 729 cm³ of media. Additionally, the media was easily obtainable.

For our carrier type, we chose the Cz1 7*10 mm, k1 Kaldnes carrier. This carrier type was made of virgin polyethylene for its material type. Additionally, it had an overall size of 10 mm in diameter by 7 mm in height. We chose this carrier because it was readily available. Additionally, the K1 Kaldnes is widely adopted in areas with moving bed biofilm reactor technology, such as fisheries (Elliott et al., 2017). The other factor that we considered was the high specific surface area offered by the K1 carrier of 1000 m²/m³. This would theoretically allow more biomass to grow on the carriers. However, some of the surface area was on the outside of the carriers, meaning that it was not all protected from abrasive forces as multiple carriers collided with one another. It was our hope that we could use the removal performance data from these carriers as a benchmark with which to compare our removal performance obtained from our 3D printed carrier geometries. In the following section, the plastic extrusion process, the process by which these carriers are typically manufactured, is described.

3.2.2 The Plastic Extrusion Process – an Overview

In the plastic extrusion process, a plastic is fed through a mold in which it is hardened into a final product. A schematic of the process can be viewed in **Figure 3-6**. When melted polymer passes through the die that shapes the plastic, it experiences some form of molecular orientation. However, after the polymer passes through the die and begins to cool, post-extrusion problems can arise such as non-uniform shrinkage and warpage. These changes in orientation can be linked to differences in velocity across the die gap. In simple shapes, such as plastic sheet, ensuring consistent dimensional properties of the die can allow for uniform velocity. However, in more complicated cross-sectional shapes, it is very difficult to eliminate this non-uniform velocity, requiring post-extrusion heat treating to stabilize the shape if necessary (EXTRUSION: Orientation: The Good and the Bad, n.d.). These variations are inevitable in plastic extrusion processes. Profile dimensions and wall thicknesses that are less than 2 mm typically experience variations of +/- 0.25 mm. The major factors influencing the level of tolerance that can be maintained are the shrink rate of the material, the complexity of the profile design, and the process conditions under which its manufactured (Plastic Extrusion Tolerances, 2019).

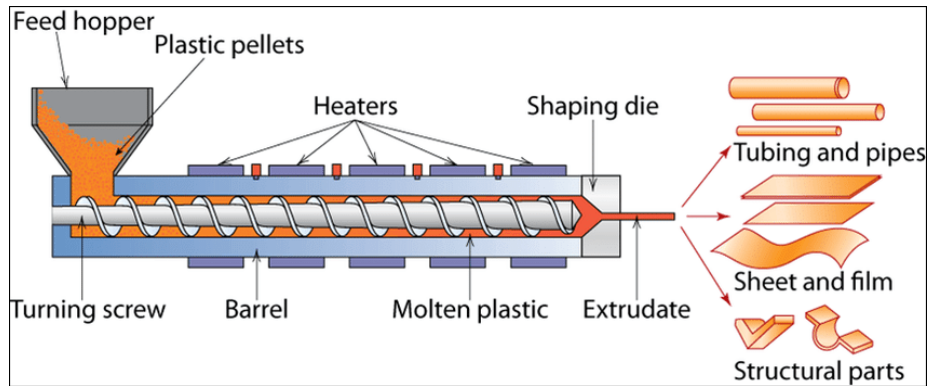


Figure 3-6: Schematic of the plastic extrusion process (From Bacalhau et al., 2017)

Depending on the final application of what is developed via plastic extrusion, deviations from nominal sizes may or may not be acceptable. Plastic extrusion does allow for rapid development of parts, making it suitable for large lot sizes of parts that can be expressed in a cross-sectional fashion. In the following section, we will explore the geometry designs specific to our study involving both 3D printed architectures and the conventional carriers.

4. Geometry Design and Fidelity of 3D Printing

4.1 Geometry Selection

To explore which 3D-printed architectures were ideal for growing biofilm, we conducted a preliminary study to narrow down what architectures worked the best for growing biofilm and treating municipal wastewater. Five base topologies were chosen that spanned a spectrum of relative densities and coordination numbers. The relative density is a measure of how much of an occupied volume is actually material, and the coordination number is a measure of the average amount of struts that come together at a node. An architecture with a higher coordination number will have higher connectivity between struts and therefore may be able to better retain biofilm than more open architectures. This will be explored in **Section 6**. An architecture with more relative density will contain more solid material and may yield different flow characteristics in a wastewater treatment setting. This was not explored in this thesis. A schematic drawing of the difference between a node and a strut is shown in **Figure 4-1**. These topologies were the simple cube, the octahedron, the body-centered cubic + simple cube, the octet, and the octet + simple cube (Gross et al., 2019; Zok, Latture, and Begley, 2016), as illustrated in **Figure 4-2**. The variables that could be altered for each geometry were their topology, strut size, and density of unit cells within a volume. The topology is defined as the configuration of struts within a geometry, and this was altered by utilizing the five topologies described above. The strut size was altered by increasing the strut radius within the same topology. Finally, the effect of unit cells within the geometry was altered by scaling a single unit cell down, while maintaining the same overall carrier size.

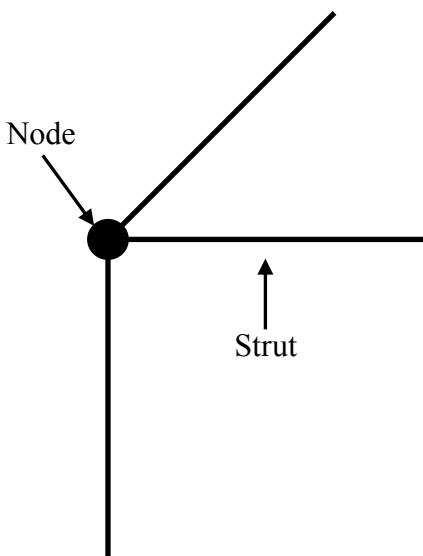


Figure 4-1: Schematic diagram depicting a node and a strut

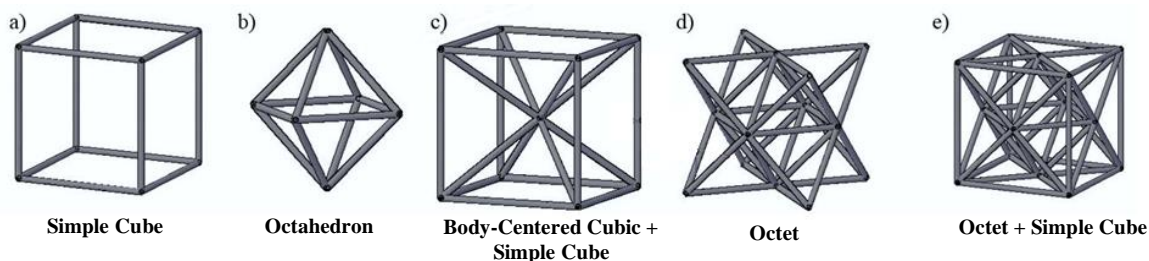


Figure 4-2: Geometries chosen for preliminary biofilm study

For our 3D printed carriers, the material used was a polyamide, nylon powder (PA 2200). This material was chosen for its high strength and stiffness, high detail resolution, and its bio compatibility. (EOS Manufacturing Solutions, n.d.). Additionally, this material was readily compatible with the EOS Formiga P110 3D-printer available for use at UMass Amherst. All files that were sent for 3D-printing were designed using AutoCAD (Autodesk®, AutoCAD 2018). Files were then exported as STL files for manufacturing. For our conventional biofilm carriers, Cz1 7*10 mm, k1 carriers were selected (Cz Garden Supply). These carriers were used in our assessment of treatment performance as a benchmark with which to compare our 3D printed carriers. They were made of virgin polyethylene material, with an overall size of 10 mm (diameter) x 7 mm (height). The specific surface area was approximately 1000 m²/m³. These carriers, as visualized in **Figure 4-3**, were considered “conventional carriers” in that they are a carrier than is often implemented in conventional moving bed biofilm reactors (MBBRs). **Table 4-1** outlines the dimensions and properties of both the conventional carriers and the 3D printed carriers.

Table 4-1: Material properties used in this study

Geometry	Material Type	Density (g/cm ³)	Melting Temperature (°C)	Tensile Strength (MPa)	Source
Simple Cube	Polyamide - PA 2200	0.93	176	52	1
Octahedron					
Body-Centered Cubic + Simple Cube					
Octet					
Octet + Simple Cube					
Conventional Carriers	High Density Polyethylene (HDPE)	0.94 - 0.97	120 - 140	10 - 30	2

1. (EOS Manufacturing Solutions, n.d.), 2. (HDPE LDPE LLDPE Comparison, n.d.)

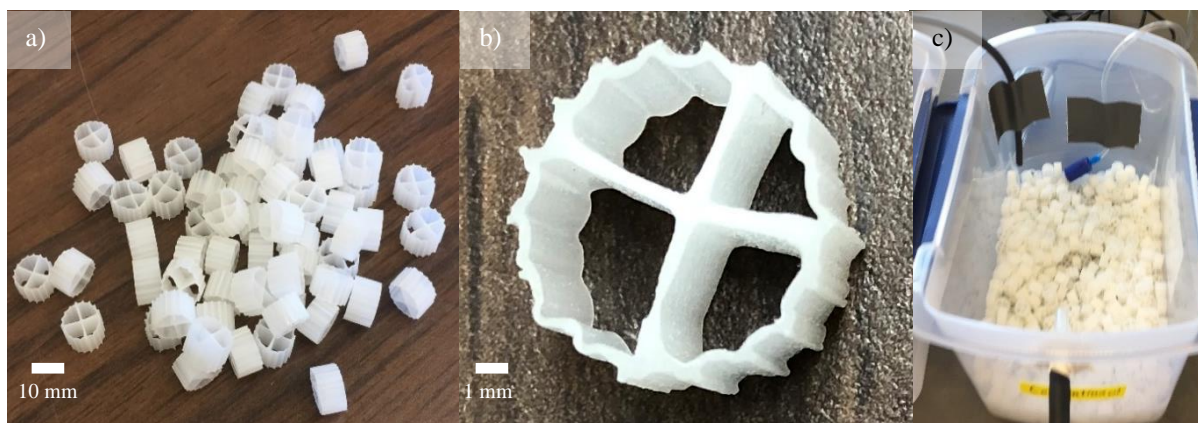


Figure 4-3: Conventional carriers used in study. a) Conventional carriers, as seen in a pile. b) A closeup view of one conventional carrier. c) The occupied volume of conventional carriers that was equivalent to the occupied volume of one of the 3D printed cubes.

4.2 3D Printing of Plates and Corresponding Error

As described above, a preliminary study was conducted to narrow the geometries to be used in the treatment and MicroCT studies. Therefore, 50 different geometries were designed and 3D printed. These geometries were printed in the form of plates, with each plate occupying a volume of 10 x 10 x 1 cm. A sample plate can be viewed in **Figure 4-4**. The topologies used to design these plates were the same as listed in **Section 4.1**. For each topology, there were five geometries described as “2 unit cells”, and five geometries described as “1 unit cells”. These labels refer to the height in unit cells of the plates. Maintaining the same overall occupied volume, the unit cells were either repeated as 2 x 2 x 20 unit cells or 1 x 1 x 10 unit cells. Finally, within each group of unit cell types, there were 5 different strut sizes used. For the 1 unit cell group, strut radii of 0.2, 0.4, 0.6, 0.8, and 1.0 mm were used, while strut radii of 0.1, 0.2, 0.3, 0.4, and 0.5 mm were used for the 2 unit cell group. An open design space existed for the design of these plates.

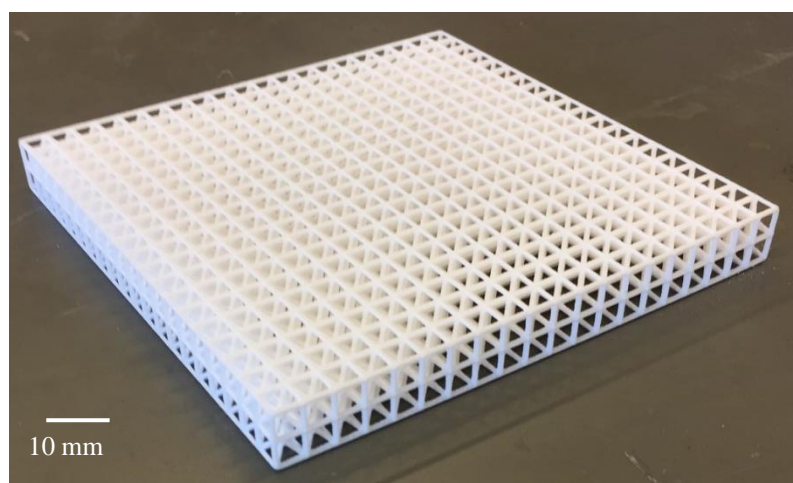


Figure 4-4: Example of a 3D-printed plate (Body-Centered Cubic + SC, 0.5 mm radius)

Therefore, strut size, unit cell density, and relative density spans were aimed at targeting a wide range of design possibilities. **Table 4-2** outlines the specific design parameters for each of the 50 geometries used in this study.

After 3D printing, a caliper was used to verify the strut diameters of the plates. Generally, it was found that the error in printed strut diameter was +/- 0.3 mm. However, the struts were more

Table 4-2: Parameters used in the design of the fifty plates studied preliminarily

Geometry	Coordination Number	Unit Cell Height	Strut Radius (mm)	Relative Density	Surface Area (cm ²)
Simple Cube	6	1	0.2	0.0070	70
			0.4	0.0282	141
			0.6	0.0634	211
			0.8	0.1128	282
			1.0	0.1762	352
		2	0.1	0.0053	107
			0.2	0.0214	214
			0.3	0.0481	321
			0.4	0.0855	428
			0.5	0.1336	534
Octahedron	8	1	0.2	0.0107	107
			0.4	0.0427	213
			0.6	0.0960	320
			0.8	0.1706	427
			1.0	0.2666	533
		2	0.1	0.0107	213
			0.2	0.0427	427
			0.3	0.0960	640
			0.4	0.1706	853
			0.5	0.2666	1066
Body-Centered Cubic + Simple Cube	11	1	0.2	0.0158	158
			0.4	0.0630	315
			0.6	0.1418	473
			0.8	0.2521	630
			1.0	0.3939	788
		2	0.1	0.0141	281
			0.2	0.0562	562
			0.3	0.1265	843
			0.4	0.2248	1124
			0.5	0.3513	1405
Octet	12	1	0.2	0.0256	256
			0.4	0.1024	512
			0.6	0.2303	768
			0.8	0.4095	1024
			1.0	0.6398	1280
		2	0.1	0.0235	469
			0.2	0.0938	938
			0.3	0.2111	1408
			0.4	0.3753	1877
			0.5	0.5865	2346
Octet + Simple Cube	13.5	1	0.2	0.0326	326
			0.4	0.1306	653
			0.6	0.2938	979
			0.8	0.5223	1306
			1.0	0.8160	1632
		2	0.1	0.0288	576
			0.2	0.1152	1152
			0.3	0.2592	1728
			0.4	0.4608	2304
			0.5	0.7201	2880

likely to be oversized than undersized. This corresponds to a radius error of ± 0.15 mm. As several of the plates printed had strut sizes that were smaller or around this 0.15 mm error, these plates had errors as high as being twice its nominal size. Because of this, struts that were nominally small in diameter tended to have much higher relative errors when compared to its nominal size than struts that were larger in diameter. In addition to having oversized strut diameters, it was also found that some geometries were uneven in terms of their strut sizes. Three topologies in particular, the simple cube, the body-centered cubic + simple cube, and the octet + simple cube, all had an exterior shell of the simple cube geometry. It was found, however, that these three topologies, when printed as 2 unit cell geometries, had simple cube struts that ran in one direction that were larger than the simple cube struts that ran in the other direction. An example of this can be seen in **Figure 4-5**. In addition to some geometries being printed with error, we also found that the smaller strut sizes were not strong enough to withstand the required handling as part of the experiment. Before even starting, the body-centered cubic + simple cube, 2 unit cell, 0.1 mm, and the octet, 1 unit cell, 0.2 mm geometries were not successfully printed. There was some initial damage associated with these geometries. Throughout the duration of the study, all of the 1 unit cell, 0.2 mm geometries were damaged in some way. Additionally, the octahedron, 2 unit cell, 0.1 and 0.2 mm geometries were damaged. The octahedron unit cells were connected by a single node, due to their design, so it is logical that small, weaker struts were more vulnerable to failure. However, geometries with larger struts were sturdy and withstood the stresses induced during this study. Generally, it was the less dense geometries (1 unit cell vs. 2 unit cell) with smaller strut sizes that were the most prone to damage. This makes sense because these struts are slenderer and less connected, making them less resistant to forces that could cause them to buckle and or break.

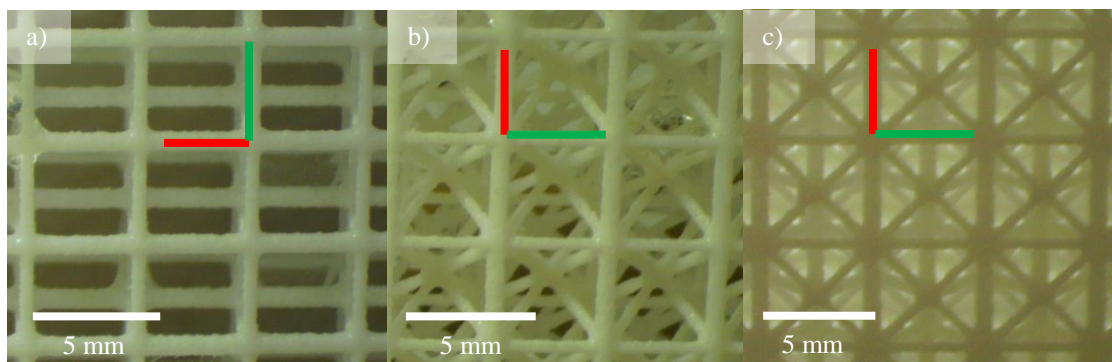


Figure 4-5: Depictions of three geometries with uneven strut sizes. The white bar indicates the scale size of each picture. The green bar represents the direction of struts that were printed smaller, while the red bar represents the direction of struts that were printed larger. a) Simple Cube, 2 Unit Cell, 0.2 mm. b) Body-Centered Cubic + Simple Cube, 2 Unit Cell, 0.3 mm. c) Octet + Simple Cube, 2 Unit Cell, 0.3 mm.

4.3 Biofilm Imaging via Microscopy

After printing all of the plates, special racks were also designed such that the plates could be maintained in an upright position. The goal of this study was to qualitatively assess the biofilm that formed on the plates, so all of the plates were housed in the same reactor. A schematic of this setup can be viewed in **Figure 4-6**. To ensure the biofilms had sufficient nutrients to promote their

growth, they were fed with a high COD media solution (**Table 4-3**) and provided with three aerators to ensure enough dissolved oxygen. These aerators were moved around the reactor daily to ensure that all of the plates were subjected to the same conditions. The ingredients were used to generate a 16 mM phosphate buffer solution. 20 L of solution were used to fill the reactor. This solution was changed approximately every 3 days to ensure that food was not a limiting factor in biofilm development in an effort to explore unrestricted growth. The biofilm was inoculated using 50 mL of activated sludge obtained from the Amherst wastewater treatment plant.

To monitor biofilm growth over time, the plates were imaged using an Amscope stereozoom microscope with an 18 MP microscope camera attached to the objective. Plates were removed from the tank and placed in a 1 L beaker containing tap water. This beaker was used to transfer the plates from their holding reactor to the camera. Once at the camera, the plates were setup to be viewed by the camera as seen in **Figure 4-7**. A clip was lightly applied next to the plate such that it could stand on its own without falling over. Microscopy was conducted every other day for the first 2 weeks, then weekly for an additional 4 weeks, for a total of 6 weeks. The images were then qualitatively examined.

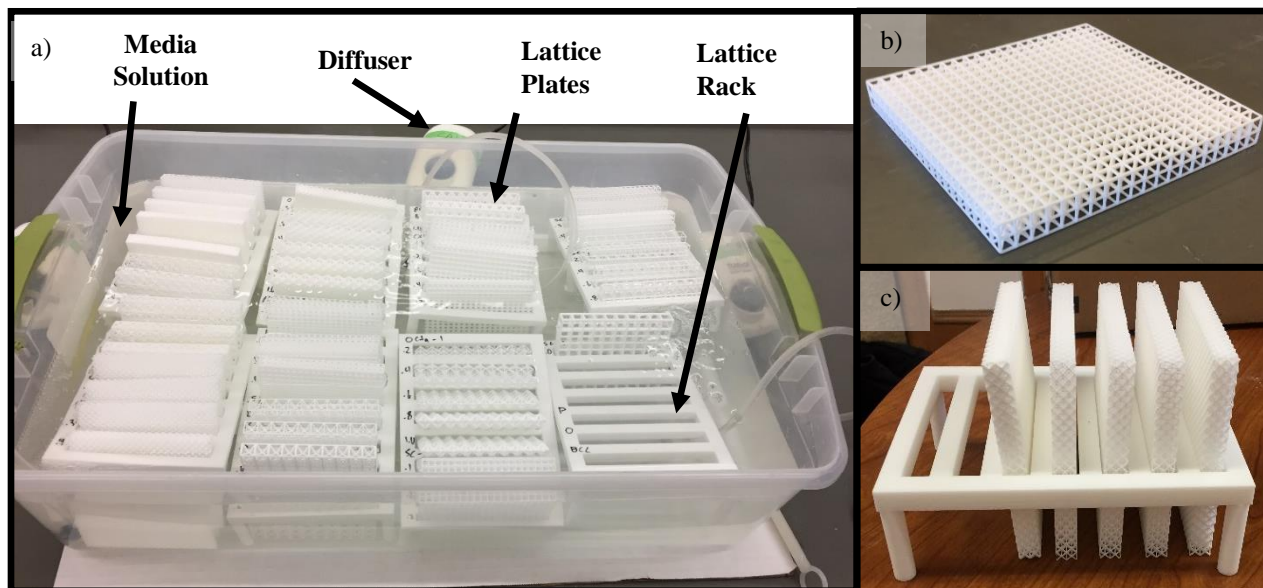


Figure 4-6: A schematic of the setup for the microscopy study. a) The setup used to house the plates in growth media solution and provide aeration to all of the plates. b) One of the 50 plates used in the study that are housed in the reactor. c) A closeup view of one of the racks used to hold the plates in an upright position.

Table 4-3: Media solution composition used

Compound	Concentration
Sodium Phosphate Dibasic Anhydrous	1.40 g/L
Potassium Phosphate Monobasic	0.85 g/L
Ammonium Chloride	0.05 g/L
Magnesium Sulfate Heptahydrate	0.10 g/L
Potassium Acetate	1.65 g/L

Trace Mineral Solution	1 mL/L
Calcium Iron Solution	1 mL/L



Figure 4-7: Microscopy setup

The images of the plates were analyzed qualitatively. The biofilm that formed around struts was assessed, as was the biofilm formed around the nodes. Patterns of early biofilm growth and how biofilm grew between different geometries were assessed. **Figure 4-8** depicts 5 geometries biofilm images over time. In this figure, the 5 different topologies are depicted with the same number of unit cells ($10 \times 10 \times 1$) and strut radius (0.6 mm). It was immediately noticed that biofilm propagation seems to form first at the nodes of the geometries. This is logical, as biofilm is known to adhere more to rougher, oblong shapes than to smooth,

obstruction-free shapes (Cox et al., 2017; Kurt et al., 2019; Kim et al., 2012; Bolton et al., 2006; Sarjit et al., 2015). It should be noted that this is also known to occur on small scales. Because the nodes form an oblong shape as struts come together, it is logical that bacteria would prefer to aggregate in the nodes during early biofilm formation. This is also evident even in the matured biofilm seen in day 42, as the biofilm appears to be the thickest where struts come together to form nodes.

While this study helped to give insight into the biofilm-forming trends of the architectures, we were unable to accurately gather quantitative data. It was apparent that the nodes seemed to play a role in the formation of biofilm on the architectures, but this was difficult to quantify due to the 2-dimensional nature of the image. Biofilm thickness could be quantified around a strut and then extrapolated around the strut into a volume, but biofilm formation around a node could not be quantified in this way. Additionally, the 2-dimensional photo did not allow us to quantify any biofilm inside of the plates, despite the fact that the inside is likely more protected from abrasive and shear forces than the outside. Finally, it was difficult to assess thin biofilm on these struts as the biofilm did not have a drastic contrast difference from its support lattice due to the fact that the biofilm itself was somewhat clear.

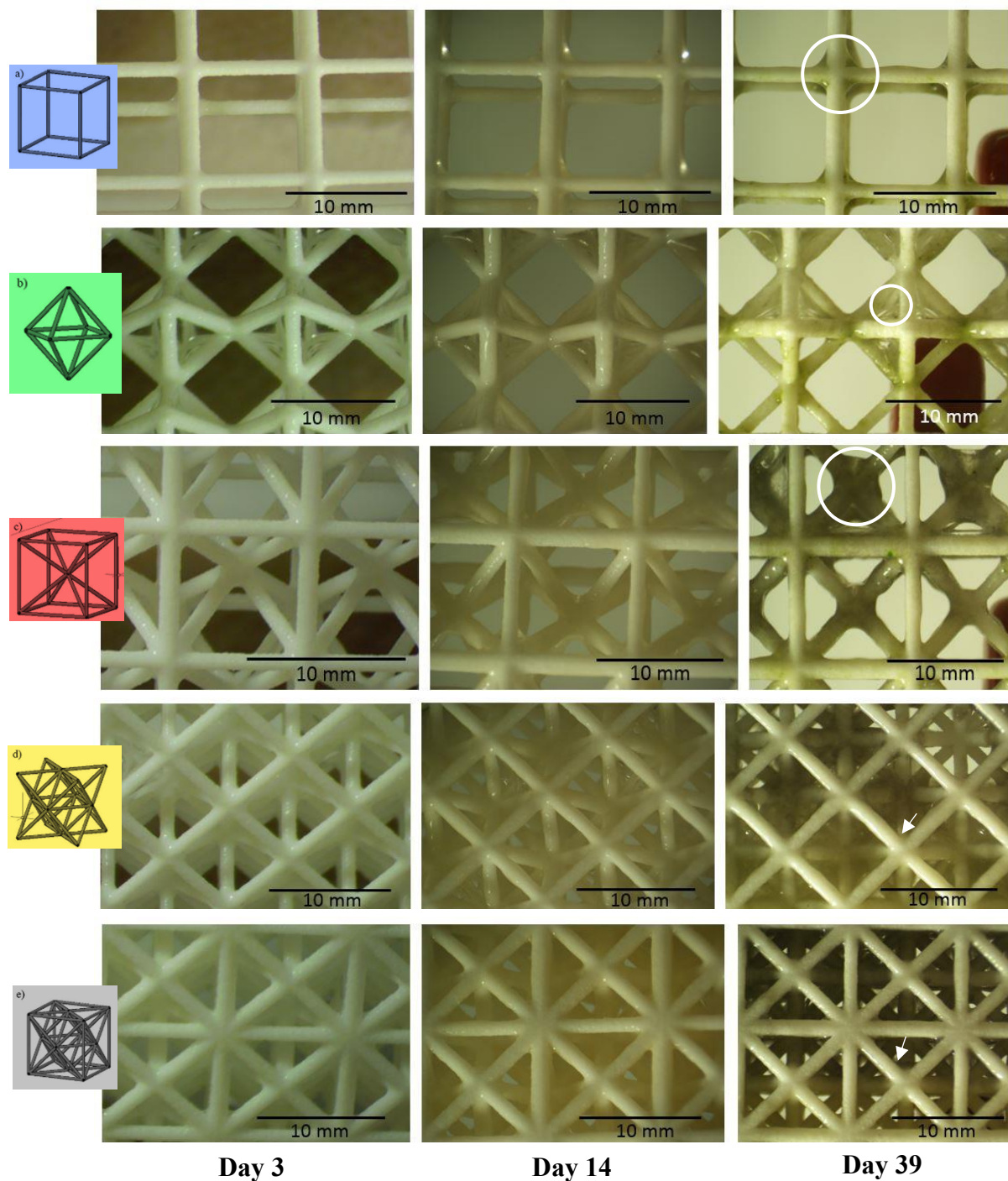


Figure 4-8: Biofilm growth on five geometries at 3 points in time. All geometries are the 1 unit cell, 0.6 mm version of the topologies. The topologies are, from top to bottom, the simple cube, the octahedron, the body-centered cubic + simple cube, the octet, and the octet + simple cube. The time images, from left to right, are day 3, day 14, and day 39. Note: the colors of the topologies on the left side of the images correlates with the colors of results that will be shown of the topologies in sections 5 and 6 of this thesis. Note that the white circles and arrows on Day 39 highlight the presence of biofilm that grew on the geometries. See appendix for the other geometries.

This study was used as a preliminary study to dictate how subsequent studies were conducted. Despite limitations of the microscopic qualification, we did learn some valuable information. As described in Section 4.2, smaller strut sizes were both more prone to printing error and damage during studying. Therefore, it was decided that strut radii of 0.3 mm or smaller would not be used for subsequent studies. However, the struts with smaller radii seemed to form thicker biofilm as there was more void space for these geometries. Therefore, strut sizes in the middle of the range were chosen for future analysis. Specifically, the 0.4 and 0.6 mm strut sizes were chosen. Our two hypotheses were that we could use new architectures to grow biofilm that could achieve higher levels of COD and ammonia removal and that these architectures would yield unique biofilm volumes. To target these hypotheses, we created a treatment study that could quantify the removal characteristics of the biofilms, and a quantification study that could quantify the biofilm formation patterns.

5. Biofilm Treatment Performance

To assess the performance of the biofilm that formed on the 3D printed architectures, both a lab-scale pilot study and a batch study were conducted. The first allowed us to assess performance of the carriers were they to be placed into a wastewater treatment application, while the second allowed us to more carefully assess the performance of the biofilm that formed on the carriers. This is important because our goal is to determine if architecture can lead to a biofilm carrier that yields biofilm with higher removal of ammonia and COD. Specifically, this study allows us to target answering our second hypothesis, which is composed of two main research questions: Can we use 3D printing to develop architected biofilm carriers that can achieve a higher performing biofilm carrier, in terms of better ammonia and COD removal, for use in a wastewater treatment setting? How is the biofilm performance of the architected biofilm carriers better than those of the conventional carriers?

5.1 Methods

To assess which architectures performed the best wastewater treatment, 10 cubes were 3D printed, using the topologies previously described in **Section 4**. These cubes contained 2 of each topology, with one of these having a strut radius of 0.4 mm and the other having a strut radius of 0.6 mm. These cubes were 9 x 9 x 9 cm, with 9 x 9 x 9 unit cells, meaning that each unit cell was 1 cm³ in volume. This size provided a large carrier volume while maximizing the volume capacity that could be printed by the ADDFab facility. In addition to the cubes, an equivalent volume of conventional carriers was measured such that 729 cm³ of carriers were added. This equivalent volume was the volume of space that each cube occupied (9 x 9 x 9 cm). This provided a benchmark for comparison, as all carriers occupied a volume of 729 cm³. **Figure 5-1** depicts the carriers that were printed, as well as the conventional carriers. Note that only the 0.4 mm strut carriers are shown in the figure. **Table 5-1** depicts the geometric characteristics of each of the carriers.

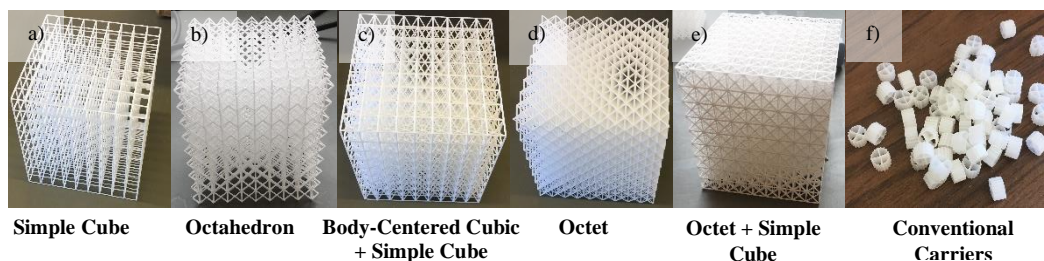


Figure 5-1: Carriers used in the treatment study. All geometries above are the 0.4 mm strut radius versions of the topologies. a) Simple Cube. b) Octahedron. c) Body-Centered Cubic + Simple Cube. d) Octet. e) Octet + Simple Cube. f) Conventional Carriers

Table 5-1: Geometric characteristics of the carriers

Carrier	Abbreviation	Volume (cm ³)	Surface Area (cm ²)	Relative Density (mm ³ / mm ³)	Coordination Number	Number of Pieces
Simple Cube (0.4 mm)	S-4	729000	679	0.0186	6	1
Simple Cube (0.6 mm)	S-6	729000	1018	0.0419	6	1
Octahedron (0.4 mm)	O-4	729000	1555	0.0427	8	1
Octahedron (0.6 mm)	O-6	729000	2332	0.0960	8	1
Body-Centered Cubic + Simple Cube (0.4 mm)	B-4	729000	1948	0.0534	11	1
Body-Centered Cubic + Simple Cube (0.6 mm)	B-6	729000	2922	0.1202	11	1
Octet (0.4 mm)	OT-4	729000	3282	0.0900	12	1
Octet (0.6 mm)	OT-6	729000	4923	0.2026	12	1
Octet + Simple Cube (0.4 mm)	OS-4	729000	3961	0.1087	13.5	1
Octet + Simple Cube (0.6 mm)	OS-6	729000	5941	0.2445	13.5	1
Conventional Carriers	Conv	729000	7290	0.1702	N/A	633

As previously described, the conventional carriers were chosen in part due to their high surface area to volume ratio. Because of this high ratio, these carriers have a high surface area in a small volume and should be well suited to growing biofilm. As seen in **Figure 5-2**, the surface area to volume ratio of the conventional carriers is actually higher than the surface area to volume ratios of the 3D printed carriers. Were the role of architecture to play no role in biofilm formation, then the 3D printed carriers would be at a disadvantage when compared with the conventional carriers. Geometries with more struts, like the octet + simple cube, have more surface area than geometries with less struts, like the simple cube. Additionally, increasing the thickness of the strut radii from 0.4 mm to 0.6 mm also increases the available surface area for the biofilm to attach to and grow on. In this section, we explored the architecture's ability to treat wastewater at the bench-scale level.

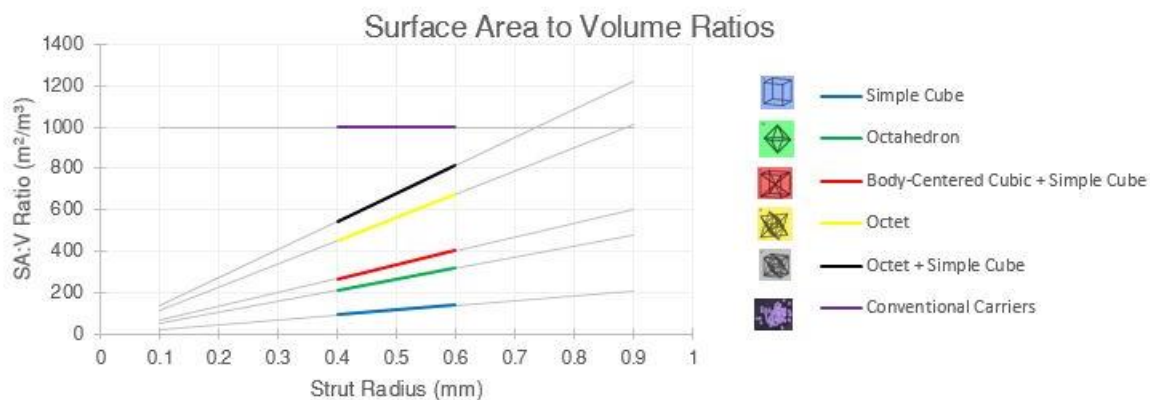


Figure 5-2: Surface area to volume ratios (SA:V) for all 3D printed carriers and the conventional carriers. For each of the 3D printed topologies, the SA:V ratio is a function of the strut radius. For the conventional carriers, the SA:V ratio is fixed, and is represented as a straight line. Only the colored areas of the graph were used in this study as the 0.4 and 0.6 mm points, with the gray areas being theoretical SA:V ratios that were not explored in this study.

5.1.1 Pilot Treatment Study

To assess how the carriers might perform in a wastewater treatment plant, a bench scale study was conducted. Each carrier was placed in an individual reactor for treating a synthetic wastewater solution. Each reactor was inoculated using 50 mL of activated sludge from the Amherst WWTP. **Figure 5-3** provides a schematic of the reactors. Media was first added to 20 L, where it was pumped to each reactor at a fixed flow rate (**Table 5-2, Table 5-3**) until empty. This served as the “influent” media to the system. Each of these carboys was connected to another 20 L carboy that was filled with nitrogen gas. This gas served two purposes. The first was to purge the system of oxygen, which is a common electron acceptor, to prevent biomass from growing in the carboys themselves, and the second was to maintain pressure in the media carboys such that a vacuum would not develop. This solution was then pumped via a media peristaltic pump to each of the reactors at a constant flow rate. Each reactor contained one of the 11 total carriers, 10 of which being the cubes and the 11th being the conventional carriers. Because the 3D material was less dense than water, the cubes were predisposed to floating. Therefore, a rubber stopper was placed on each of the 3D printed cubes to prevent them from floating. Media from the pumps entered these reactors at the back of the reactors. Additionally, a porous aquarium air stone was used with an aquarium pump to provide the system with dissolved oxygen. After a certain hydraulic residence time (HRT) (**Table 5-2, Table 5-3**), the water flowed out of the reactor via gravity to a waste collection bucket.

During sampling, the effluent hoses were removed from the waste collection bucket and into a 50 mL Corning sample vial for sample collection. 50 mL of unfiltered sample was collected. These vials were then filtered with a 0.45 μm filter into a 15 mL Corning sample vial, where mL of filtered sample was obtained. These vials were used in COD and NH_4^+ Hach kits (2125815, TNT 832), following the manufacturer specifications. To get an estimate of the amount of suspended biomass that grew in the reactors, optical density was measured on the unfiltered

samples by measuring their absorbance at a wavelength of 450 nm. While not a direct measurement of the concentration of suspended biomass, with all other reactors experiencing the same conditions, a higher optical density absorbance correlated with a higher amount of suspended biomass.

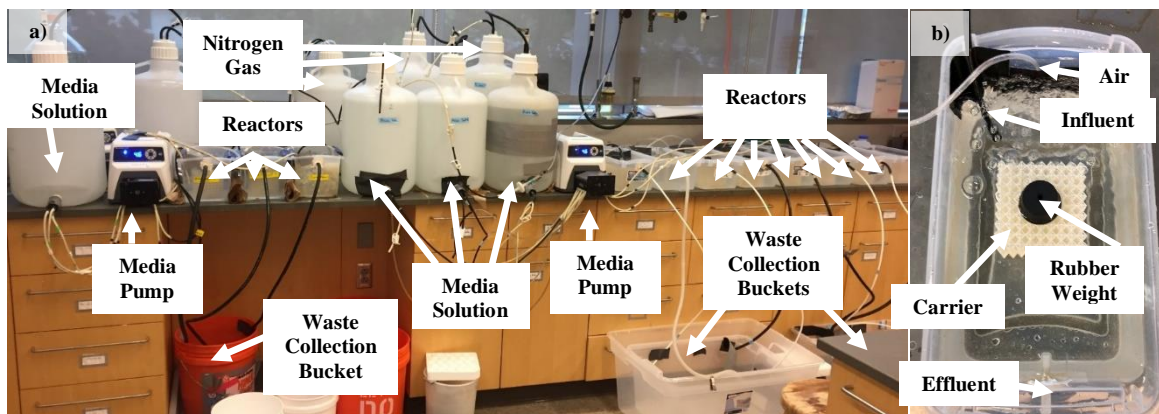


Figure 5-3: Schematic of flow through the reactors. a) A wide view of all of the reactors, showing how the media gets pumped to the reactors and then drained via the effluent ports. b) A closeup view of a single reactor (octahedron, 0.4 mm radius) that shows the media solution and the carrier, as well as defining key parts of the reactor.

The reactors were subjected to several different operating conditions throughout the continuous flow operation of the reactors. These conditions can be broken down into three distinct phases: 1000 mg/L of COD, 500 mg/L of COD, and 100 mg/L of COD (**Table 5-2**, **Table 5-3**, **Table 5-4**). Briefly, the reactors were operated first at a buffer concentration of 16 mM and a COD concentration of 1000 mg/L. Next, the reactors were operated at a buffer concentration of 16 mM and a COD concentration of 500 mg/L. After this, a batch study was conducted, which will be described in more detail in **Section 5.1.2**. Finally, after this study, the reactors were operated at a buffer concentration of 4 mM and a COD concentration of 100 mg/L. In addition to changing the buffer concentration and COD concentration, the HRT was also varied (**Table 5-2**) with it being longer prior to the first batch study and shorter after. In the 1000 mg/L study, COD, ammonia, and optical density were measured. The Octahedron, 0.4 mm, Octet + Simple Cube, 0.4 mm, and the Conventional Carriers reactors were started before the rest of the reactors. To compensate for this, all time readings are reported as days since start, and the other reactors were operated after the first three reactors stopped. In the 500 mg/L study, only COD and optical density were measured. Additionally, after operating the 500 mg/L study, the reactors were all put on the same time cycle. Therefore, the 500 mg/L study was operated for two weeks less in the case of the eight later reactors than the first three reactors.

Table 5-2: Operating conditions of the reactors. (1) and (2) refer to the reactor labels in **Table 5-3**.

COD Concentration (mg/L)	Ammonia Concentration (mg/L)	Days in Operation	Flow Rate (mL/min)	HRT (Hours)	Horizontal Flow Velocity (mm/min)
1000	13	36	2	45.0 (1), 50.4 (2)	0.11 (1), 0.07 (2)
500	13	33 (1), 21 (2)	2	45.0 (1), 50.4 (2)	0.11 (1), 0.07 (2)
100	13	72	2.8	32.1 (1), 36.0 (2)	0.16 (1), 0.10 (2)

Table 5-3: Definitions of the reactors

Reactor Label	Reactor Volume (mL)	Carriers	Depth of Liquid (cm)
1	5400	S-4, S-6, O-6, B-4, B-6, OT-4, OT-6, OS-6	10
2	6048	O-4, OS-4, Conv	18

Table 5-4: Chemicals used throughout study

Compound	16 mM Phosphate Buffer – Chemical Concentration	4 mM Phosphate Buffer – Chemical Concentration
Sodium Phosphate Dibasic Anhydrous	1.40 g/L	0.35 g/L
Potassium Phosphate Monobasic	0.85 g/L	0.21 g/L
Ammonium Chloride	0.05 g/L	0.05 g/L
Magnesium Sulfate Heptahydrate	0.10 g/L	0.025 g/L
Potassium Acetate (if COD = 1000 mg/L)	1.65 g/L	N/A
Potassium Acetate (if COD = 500 mg/L)	0.825g/L	N/A
Potassium Acetate (if COD = 100 mg/L)	N/A	0.16 g/L
Trace Mineral Solution	1 mL/L	1 mL/L
Calcium Iron Solution	1 mL/L	1 mL/L

5.1.2 Biofilm Performance

To assess the performance of the biofilm that formed on the carriers, two batch studies were conducted. The first was conducted between the 500 mg/L and 100 mg/L continuous flow studies. The second was conducted after the 100 mg/L continuous flow study. A standalone reactor was created for each carrier. In the second batch study that was conducted, a reactor with no carriers was also added, for a total of 12 reactors. This reactor was inoculated with 50 mL of activated sludge. This reactor served as a control to ensure that suspended growth was not

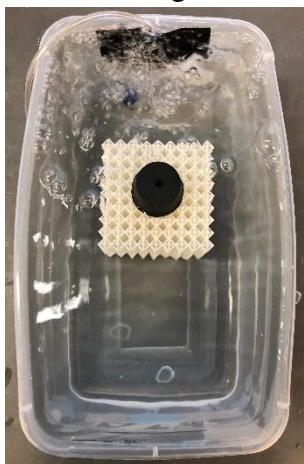


Figure 5-4: Image of Octahedron, 0.4 mm batch reactor (Note: Image is of setup only, not of the biofilm from the batch study)

significant when compared with the biofilm. Each reactor was given their own aquarium pump and aeration stone, as seen in **Figure 5-4**. Synthetic media was prepared as a 4 mM phosphate buffer with 200 mg/L of COD. It was prepared in bulk and placed in each reactor without a pumping system to continuously move the media through the system. Instead, each carrier was placed in its new reactor and COD and ammonia were measured over a shorter time scale to assess how the biofilm removes these parameters. Only COD was measured in the first batch study, while both COD and ammonia were measured in the second batch study. The timescale for this experiment was relatively short, with the study being conducted for only 48 hours. Samples were taken every 2 hours for 10 hours, then again at 24 and 51 hours. Removal over the first 10 hours was used to determine biofilm performance, while the 48 hours allowed COD removal to progress to near complete removal. 10 hours was chosen because it was the time period during which the most readings were taken. Additionally, this time period was short enough to prevent large accumulations of suspended biomass. Because only the carrier was

moved from the old reactors to the new ones, only attached biomass could enter the new reactor to remove the contaminants in this experiment. Therefore, the biofilm contribution to removal efficiency was quantified here.

5.1.3 Biomass Quantification

After the conclusion of the second batch study, the biomass on each of the carriers was quantified in an effort to compare the mass of biofilm that formed on each carrier type. Prior to growing biofilm at the beginning of the study, the weight of each of the cubes was determined. After the batch study, 11 pieces of tin foil were labelled with each carrier type. These pieces were weighed, and their masses were recorded. The cubes were then removed from their hydrated states and allowed to drain for at least 30 seconds such that the water stopped draining from the cubes and only what was attached to the carrier remained. They were placed on the tin foil and wrapped such that only the top sections of the carriers were exposed and the top and bottom of the carriers were securely wrapped in the foil. Their “hydrated biomass weights” were weighed and determined. For the conventional carriers, each piece was drained in a similar fashion, with less time being needed for each piece. The carriers were then dried in a drying oven at 115° for 24 hours. After drying, the carriers were then weighed again, this time their “dry biomass weights”

being determined. The known masses of the tin foil and carriers could be subtracted to determine the weight of just the biomass.

5.2 Results

5.2.1 Pilot Treatment Study

In the first phase of the flow-through study, the 1000 mg/L COD data was explored. **Figure 5-5** depicts the performance of all of the reactors over the whole study. Note that the data is designated after 7 days of startup, meaning that removal fractions were only considered after the first 7 days. This was to allow time for biomass to grow in all reactors and ensure that treatment could actually take place. **Figure 5-5a, b, and c** show average COD removal for each of the reactors, average ammonia removal, and average optical density, respectively. The error bars in each reactor represent the standard deviation of all data points collected throughout the phase, after 7 days of start-up time. It should be noted that for three of the reactors (octet + simple cube, 0.6 mm, body-centered cubic + simple cube, 0.6 mm, and octet, 0.4 mm), acetate was not added to the media bottle that fed these reactors on day 0. After day 3 and subsequent media changings, acetate was added as intended. In terms of COD removal, the conventional carriers yielded an average removal of 85.8% +/- 6.2%. This was the lowest removal of all of the carriers studied in this phase. The highest removal was seen in the body-centered cubic + simple cube, 0.4 mm, with an average removal of 93.7% +/- 2.8%, and the second highest removal was seen in the octet + simple cube, 0.6 mm, with an average removal of 92.5% +/- 3.6%. In terms of ammonia removal, the octet + simple cube had the lowest average ammonia removal after the 7 days of start up time (86.0% +/- 25.7%). The conventional carriers had the next lowest performance, with an average ammonia removal of 95.8% +/- 6.5%. Finally, the highest ammonia removal was seen in the octet, 0.4 mm geometry, with an average of 99.5% +/- 0.7%. Most of the carriers had very high ammonia removal, with 10 of the carriers achieving greater than 95% ammonia removal.

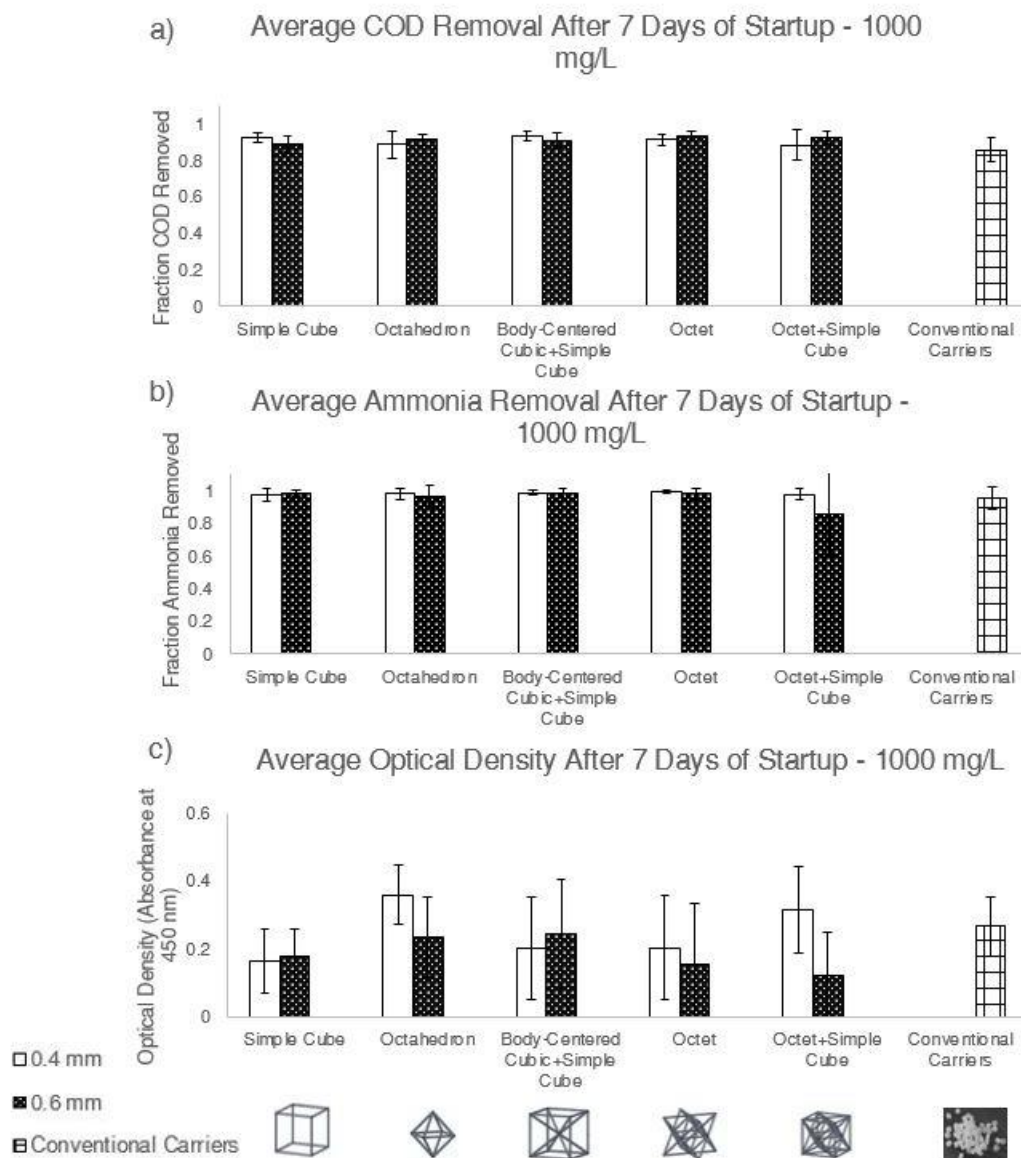


Figure 5-5: Average performance of the reactors at 1000 mg/L COD. a) Average COD removal. b) Average ammonia removal. c) Average optical density. Note that all averages are taken after a 7 day startup period to allow biomass to accumulate in the system.

The second phase of the flow-through study involved a COD concentration of 500 mg/L. The COD concentration and optical density measured during this phase can be seen in **Figure 5-6**. Ammonia removal was not measured during this phase of operation. This phase was not run for the same amount of time for all of the carriers. For the octahedron, 0.4 mm, the octet + simple cube, 0.4 mm, and the conventional carriers, the reactors were started two weeks earlier and therefore ran for two weeks longer than the other reactors. The error bars represent the standard deviation of the values.

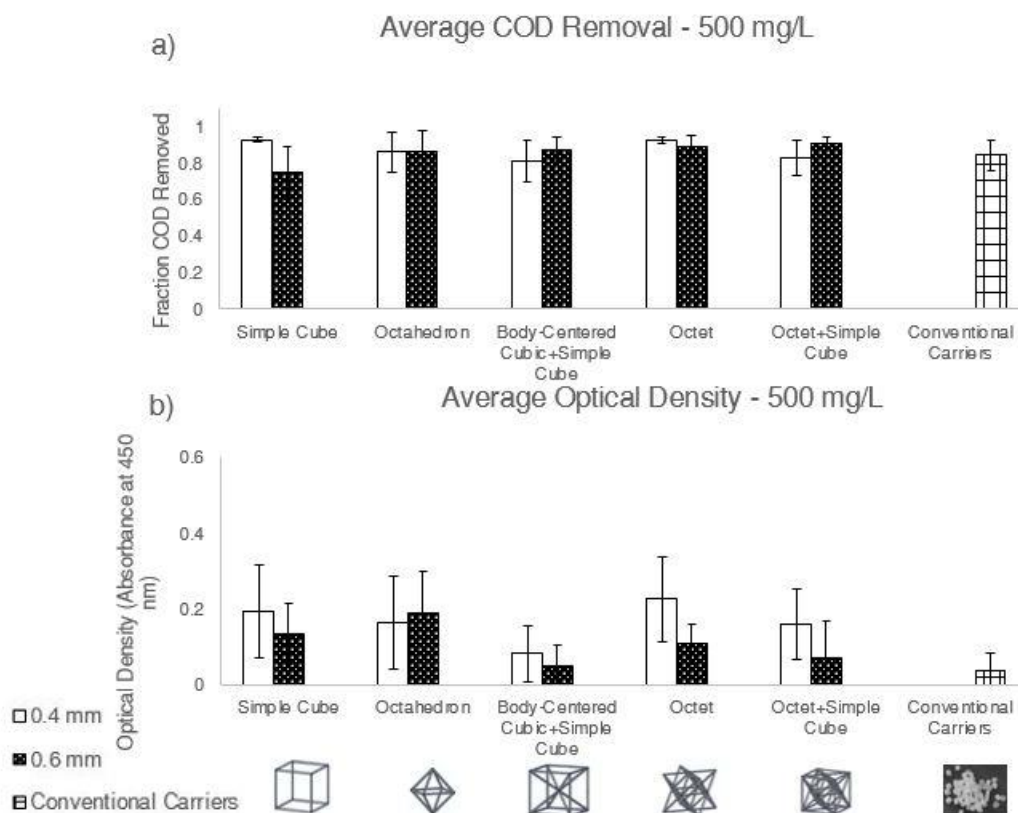


Figure 5-6: Average performance of the reactors at 500 mg/L COD. a) Average COD removal. b) Average optical density.

In the third phase of the flow-through study, the 100 mg/L COD data was explored. After conducting the flow through scenario for 86 days, the COD removed was calculated as the COD influent concentration minus the COD effluent concentration divided by the COD influent concentration. These values were then averaged for each of the samples taken over the time period and plotted as shown in the figure above for each carrier. The COD performance of all of the reactors over this phase can be seen in **Figure 5-7**. The error bars in each reactor represent the standard deviation of all data points collected throughout the phase. Performance was similar between the reactors. The highest performing geometry, the octahedron, 0.6 mm, had 86.2% +/- 8.1% average removal efficiency. This was followed by the octet, 0.4 mm (84.8% +/- 13.2%) then by the octahedron, 0.4 mm (82.7% +/- 9.0%), then by the octet + simple cube, 0.4 mm (82.6% +/- 13.4%), and finally by the conventional carriers (81.7% +/- 18.3%). The remaining 6 architected geometries then followed this.

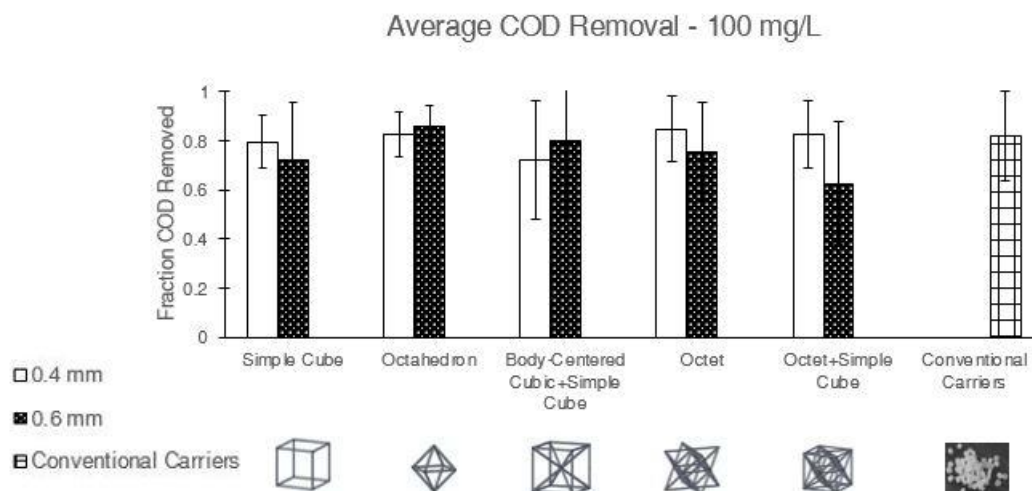


Figure 5-7: Average COD removal at 100 mg/L COD

The ammonia performance data throughout this phase is depicted in **Figure 5-8**. This figure provides ammonia removal data vs. time for each of the reactors (**Figure 5-8a**), with the metric being the fraction of ammonia removed from the initial concentration at any given time. The time to achieve near full ammonia removal, which was defined as the time when the fraction removed reached greater than 95% removal was also depicted (**Figure 5-8b**, **Figure 5-8c**). The optical density measured in each of the reactors is provided in **Figure 5-9**, with both the average (**Figure 5-9a**) and the time series (**Figure 5-9b**) versions of the data being shown. For the first 65 days, the optical density between all of the reactors was similar. It can be seen from the time plot that the conventional carriers had the highest optical density after day 72. Prior to this, most of the carriers had similar optical densities, with various carriers exhibiting some spikes. On average, the optical density was the highest in the case of the conventional carriers. However, the high optical density in the conventional carriers over time is indicative of a large presence of suspended biomass in this reactor. This, coupled with similar and in some cases better performance in the architected carriers, suggests that the suspended biomass is playing a larger role in the conventional carriers. Finally, there was settled biomass that formed in the corners of the conventional carriers' reactor in both the 1000 mg/L and 100 mg/L phases of operation (**Figure 5-10**). This biomass was not apparent in any of the 3D printed carriers.

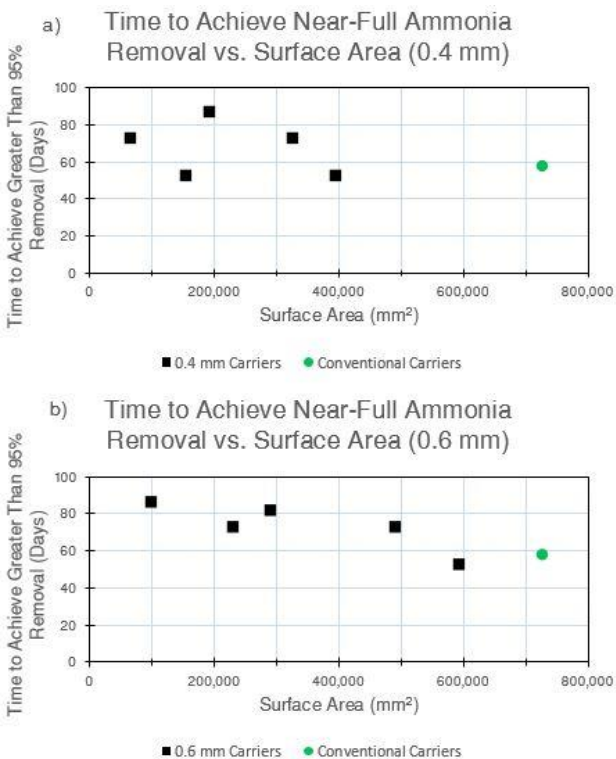
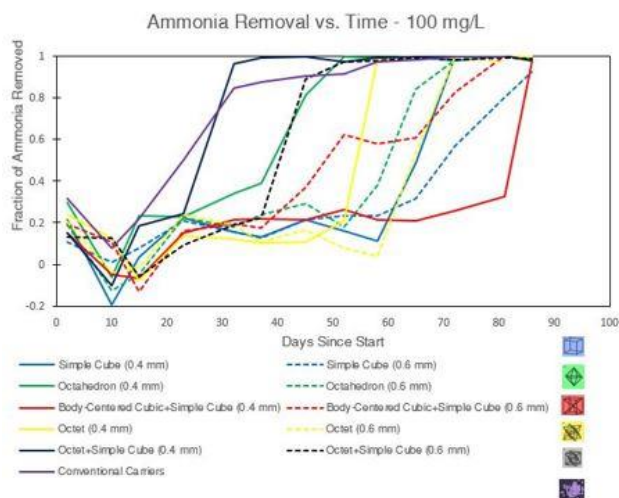


Figure 5-8: Ammonia performance data at 100 mg/L COD. Left: ammonia removal vs. time of operation. Right: a) Time to achieve near-full ammonia removal vs. surface area for the 0.4 mm carriers. b) Time to achieve near-full ammonia removal vs. surface area for the 0.6 mm carriers. Near-full ammonia removal was defined as 95% removal or higher.

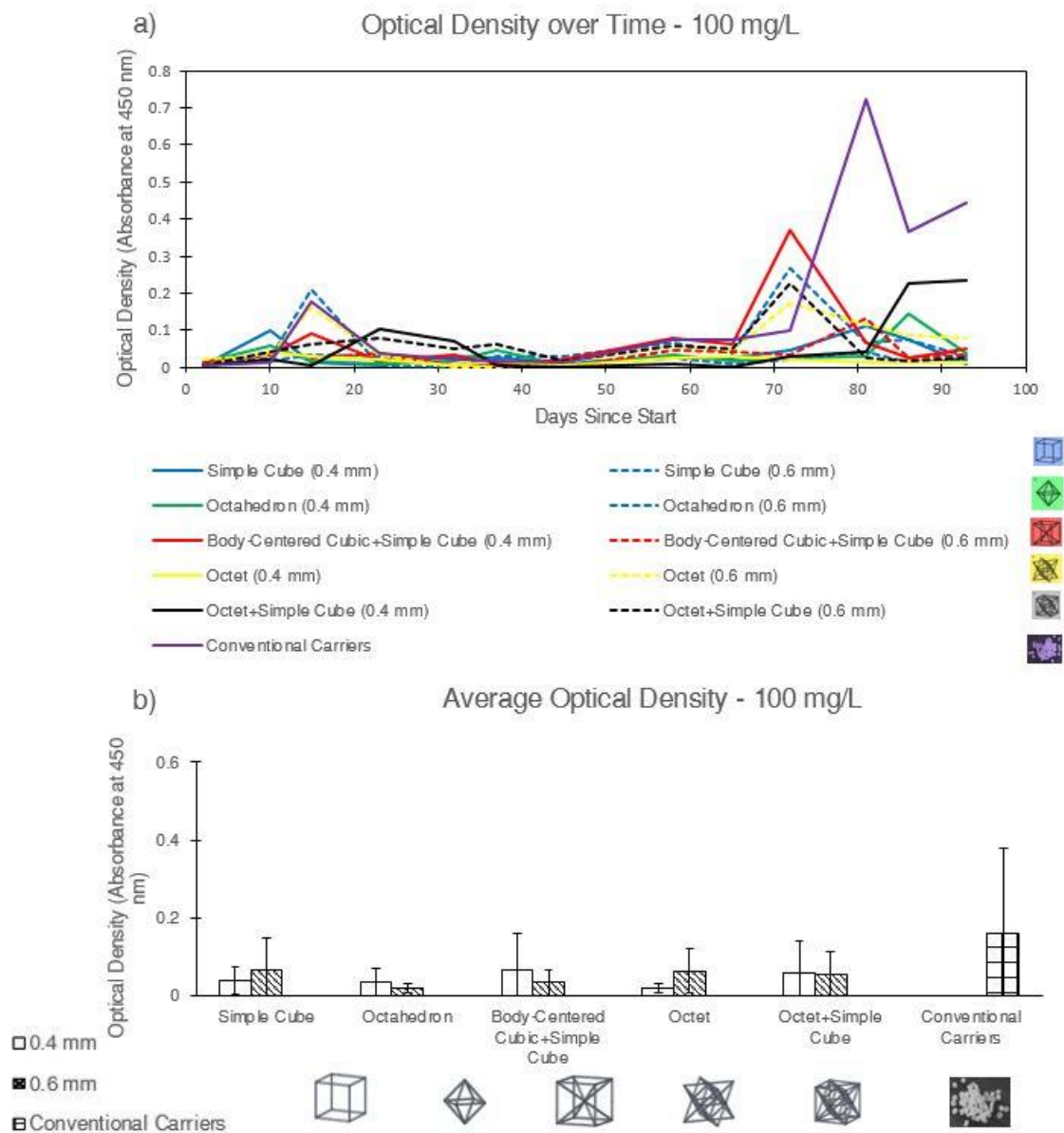


Figure 5-9: Optical density data at 100 mg/L COD. a) Optical density vs. time. b) Average optical density.



Figure 5-10: Images depicting settled biomass in the conventional carriers reactor. Images a-c depict the Octahedron-0.4 mm, Octet + Simple Cube-0.4 mm, and the Conventional. Carriers, respectively after startup (1000 mg/L COD). Images d-e depict the Octahedron-0.4 mm and the Conventional Carriers, respectively after visible biofilm has developed on the carriers (100 mg/L COD). Note that in both cases, the Conventional Carriers had large quantities of black, settled biomass.

5.2.2 Biofilm Performance

After growing biofilm on the carriers, two batch studies were conducted in which biofilm performances could be assessed for each of the carriers. The first batch study was conducted after biofilm was grown in the 1000 mg/L and 500 mg/L phases of continuous flow operation. The second batch study was conducted after biofilm was grown additionally in the 100 mg/L phase of continuous flow operation. There was not much biofilm present in the first batch study, as conditions of the 1000 and 500 mg/L study favored suspended biomass. Therefore, we did not see many differences in the performances of the biofilms alone. However, after the 100 mg/L phase of continuous flow operation, biofilm was apparent, and the COD and ammonia concentrations vs. time can be seen in **Figure 5-11**. The figure shows both COD and ammonia concentration from its initial value at time 0 to its concentration at various time intervals. In this study, a steeper slope corresponds to a faster removal rate, while a flatter, further to the right slope corresponds to a slower removal rate. A control was provided in which no carrier or biofilm were added, but activated sludge was added. All carriers exhibited some form of removal during the first 10 hours. 10 hours was used to compare the geometries and the conventional carriers because measurements were taken the most frequently during the first 10 hours, and the time scale was relatively short, limiting the amount of suspended biomass that could develop in the new reactors. In terms of COD

removal, the body-centered cubic + simple cube, 0.4 mm geometry performed the best, with a removal over 10 hours of 158.4 mg/L. This is compared to the conventional carriers, which had a removal over 10 hours of 9.4 mg/L. In terms of ammonia removal, the octahedron, 0.6 mm geometry performed the best, with a removal over 10 hours of 8.59 mg/L. This is also compared to the conventional carriers, which had a removal over 10 hours of 2.5 mg/L.

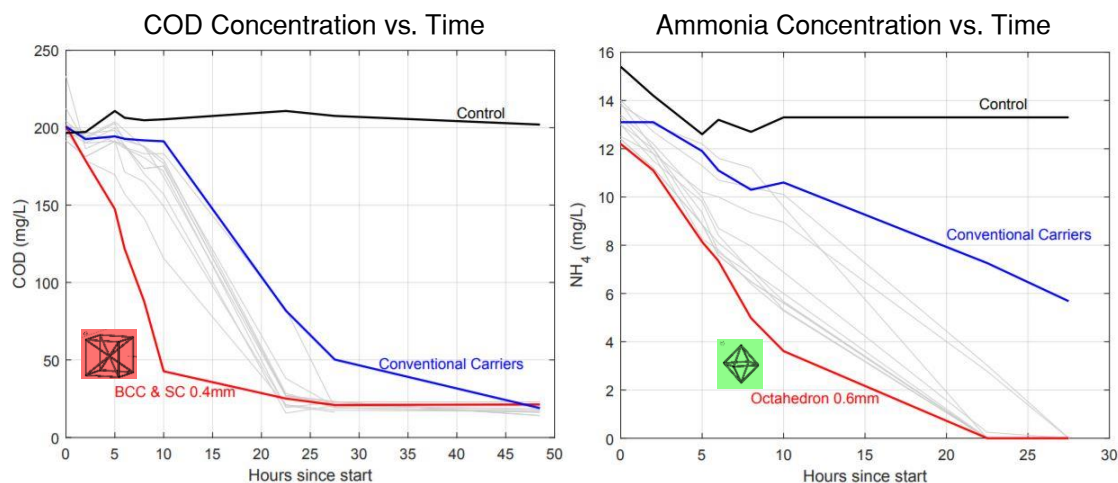


Figure 5-11: Batch study: COD and ammonia concentrations vs. time

After assessing the concentration over time for both COD and ammonia, the removal over the first 10 hours for COD and ammonia was more carefully assessed in **Figure 5-12** and **Figure 5-13**, respectively. The left side of these figures provide the total removal of either COD or ammonia over 10 hours vs. surface area for both the 0.4 mm and 0.6 mm carriers. These are compared to the conventional carriers, which are indicated as a green dot on the figures. In addition to providing information about the substrate removed, the same removal is also presented as a normalized removal per unit surface area. These are presented on the right side of the figures. These graphs follow the same format as the left graphs, with normalized substrate removal being plotted against the surface area of the carrier. The top graph represents the 0.4 mm geometries and the bottom graph represents the 0.6 mm geometries. The conventional carriers had a COD removal of 9.4 mg/L over 10 hours, a normalized COD removal of 1.3×10^{-5} (mg/L)/mm², an ammonia removal of 2.5 mg/L over 10 hours, and a normalized ammonia removal of 3.4×10^{-6} (mg/L)/mm². By comparison, all of the architected carriers outperformed the conventional carriers in all four of these metrics.

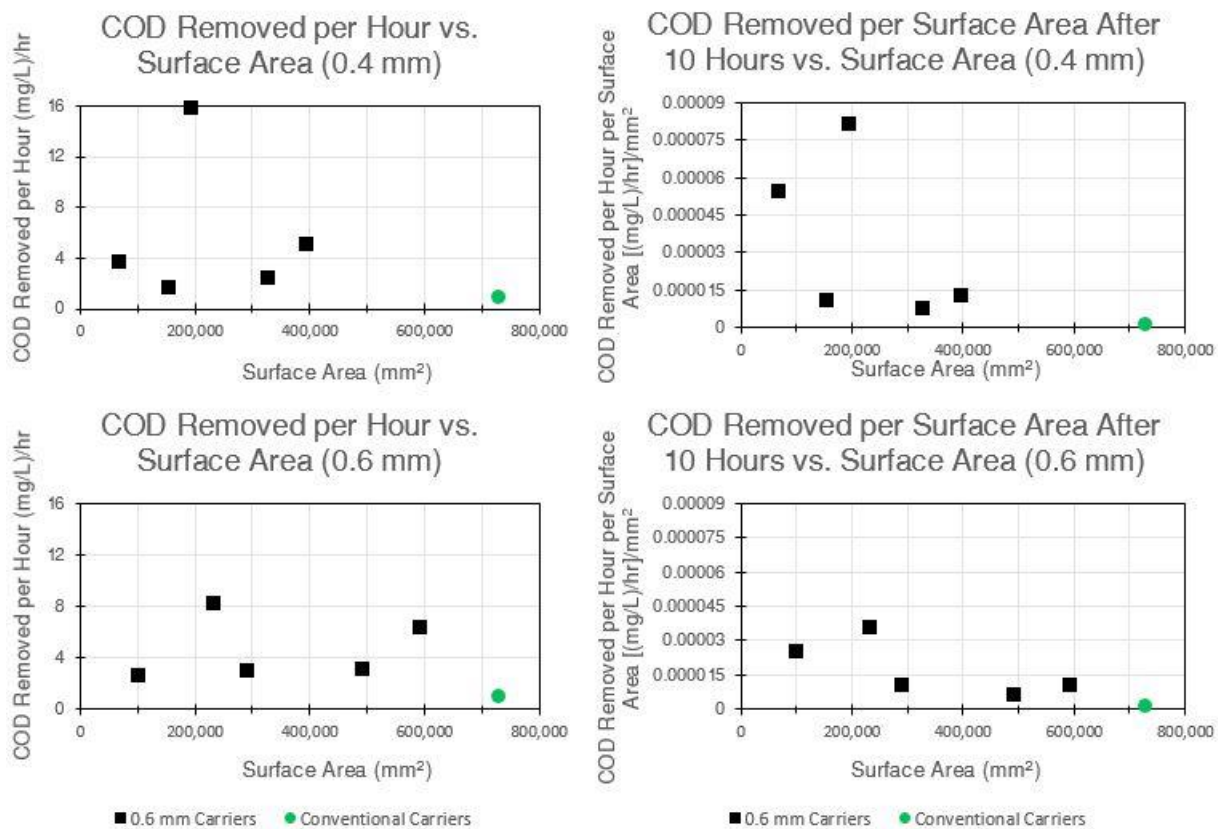


Figure 5-12: COD removed after 10 hours vs. surface area for all carriers

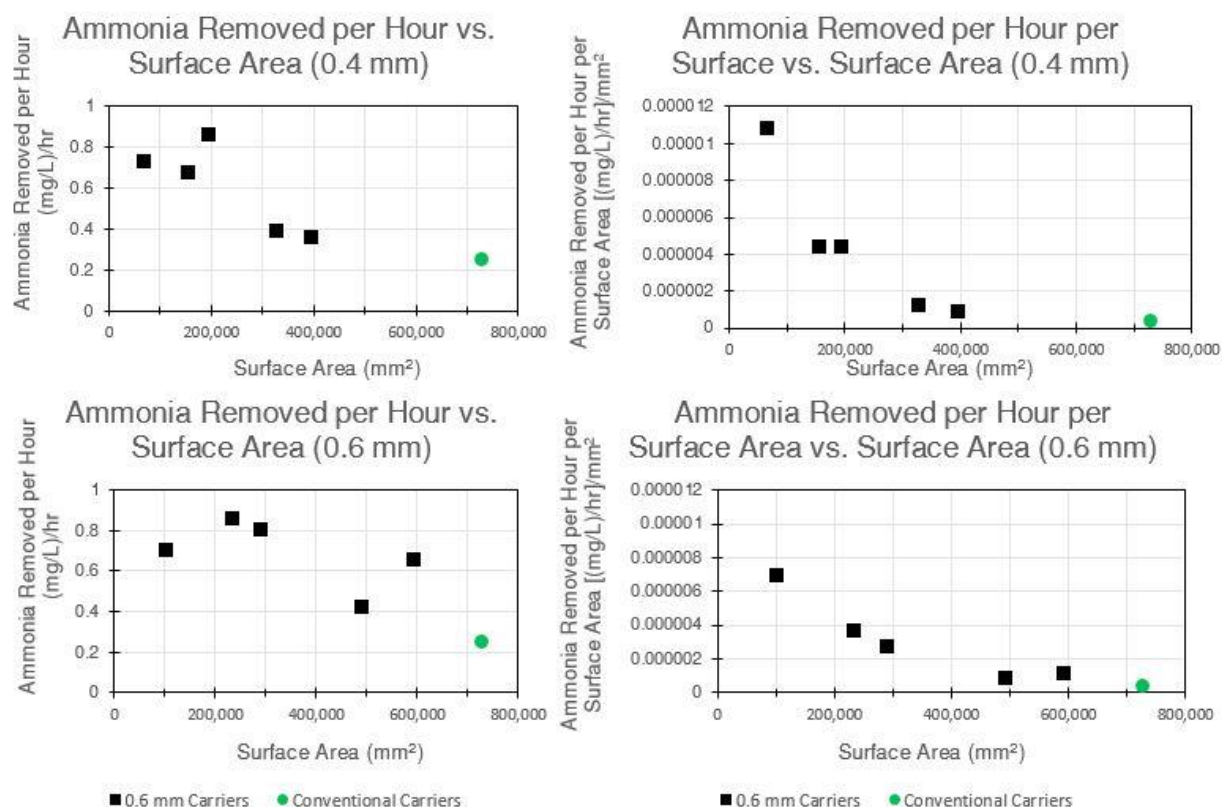


Figure 5-13: Ammonia removed after 10 hours vs. surface area for all carriers

After calculating the performance of each of the carriers in terms of both COD and ammonia removal, the carriers were normalized by the average COD and ammonia removal of all 11 carriers and plotted in **Figure 5-14**. Here, the horizontal axis is a measure of COD performance and the vertical axis is a measure of ammonia performance. The numerical values of these axes are the relationship of a single carrier's performance to the average. All of the carriers are represented as points on the graph as a graphic of the carrier based on where it performed in relation to the average of both COD and ammonia removal. All points above the horizontal red line represent higher than average ammonia removal and all points below the horizontal red line represent lower than average ammonia removal. Similarly, all points to the left of the vertical line represent lower than average COD removal, while all points to the right of the vertical line represent higher than average COD removal. This provides us with four possible zones that were achieved based on the intersection of the two lines. The bottom, left zone represents all carriers that had below average performance in both metrics. Conversely, the top, right zone represents all carriers that had above average performance in both metrics. Finally, the top, left zone represents carriers that had above average ammonia removal, but below average COD removal, while the bottom, right zone represents carriers that had below average ammonia removal, but above average COD removal. Different architectures fell into each zone based on the metrics previously used for the batch study.

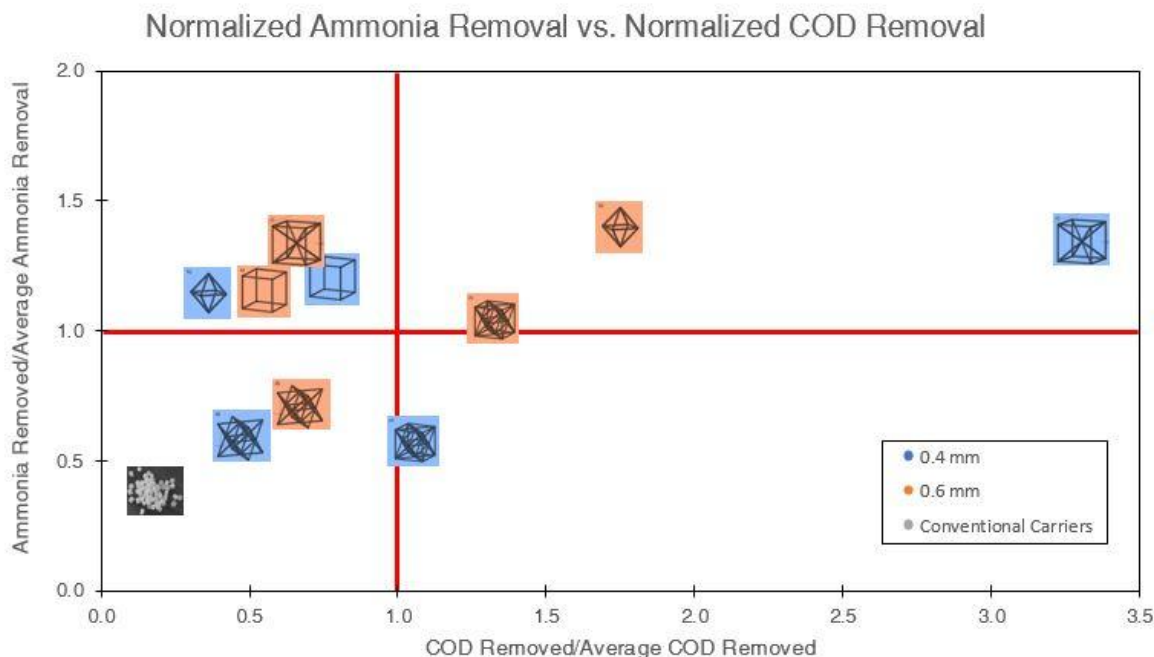


Figure 5-14: Normalized ammonia removal vs. normalized COD removal

5.2.3 Biomass Quantification

After completing the batch study, the biomass present on each of the reactors was quantified. This was quantified as a weight on a scale. This was measured both pre- and post-oven drying. The pre-oven drying weights were defined as hydrated biomass, as water was not evaporated, while the post-oven drying weights were defined as dry biomass, as water was evaporated. Here, we were primarily interested in assessing the component of the biomass that was not hydrated to gain insight into the amount of organic matter that was present in the biofilm, not the water content of the biofilm. Therefore, the dry biomass for each of the carriers is presented here in **Figure 5-15**. The hydrated biomass for each of the carriers is presented in **Section 9**, the Appendix. The octet + simple cube, 0.4 mm geometry had the most biomass, with 2.5 g of biomass. This was followed by the conventional carriers, with 1.6 g of biomass. Finally, all other carriers followed this, as outlined in **Figure 5-15**. The carrier with the highest amount of biomass was the octet + simple cube, 0.4 mm geometry, with 2.48 g of dried biomass. This was followed by the conventional carriers, which had 1.64 g of dried biomass. The conventional carriers had more dried biomass than the other 9 architected carriers.

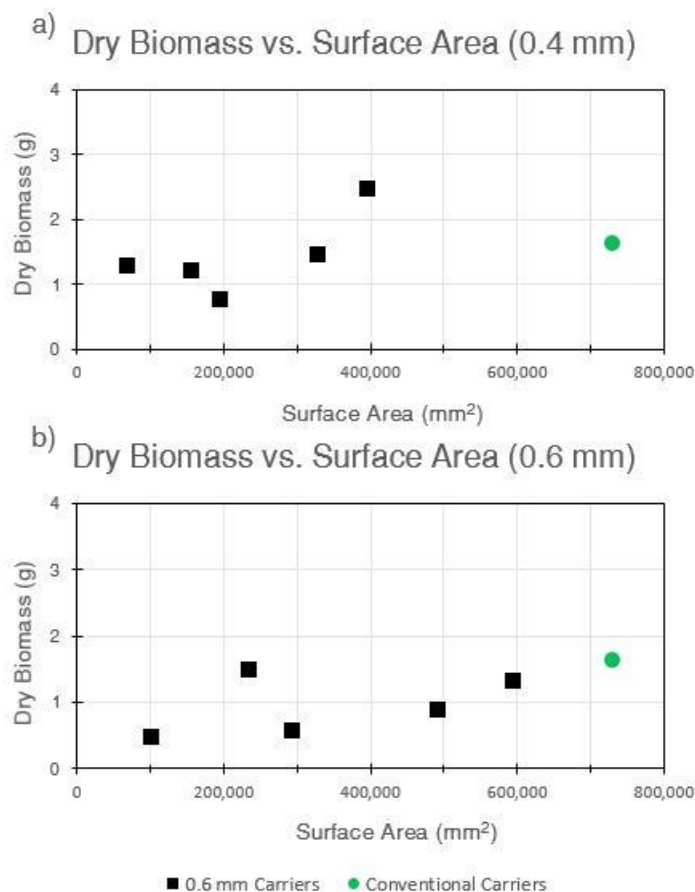


Figure 5-15: Dry biomass vs. surface area for all carriers. The top graph is representative of the 0.4 mm carriers, while the bottom graph is representative of the 0.6 mm carriers. The architected carriers are represented by black squares, with a line of best fit plotted through them for reference. The green dot on both graphs represents the conventional carriers.

After looking at the removal of COD and ammonia vs. time for each of the carriers, the kinetics of the biofilms that formed on each of the carriers was assessed by fitting a first order kinetic model to each of the carriers for both COD and ammonia. Using a first order kinetic equation, $\ln[C] = -kt$, where C is the concentration of either COD or ammonia in mg/L and t is the time passed during the batch study in hours, the biofilm kinetics, k (hr^{-1}) for each of the carriers was determined (**Figure 5-16**). Ammonia removal occurred primarily during the first 10 hours for most of the carriers. However, COD removal took longer in most cases, with the 22.5 hour mark indicating near full removal. Because of this, COD kinetics rates were calculated for both the first 10 hours of the study as well as the whole study. This allowed us to see how the kinetics between the architectures compared initially, as well as how they compared over a longer time.

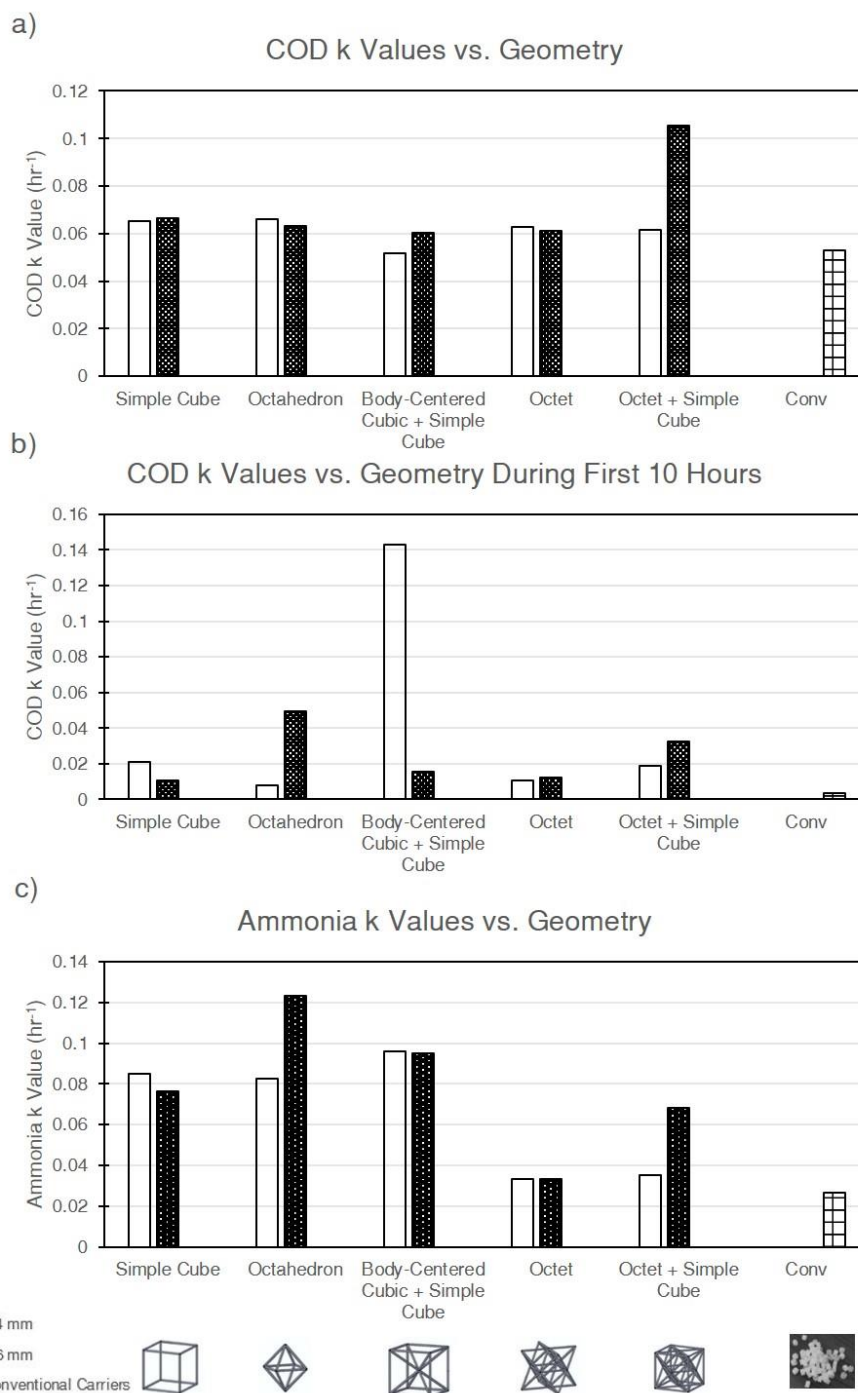


Figure 5-16: Kinetics "k" values for each of the geometries based on performance during the batch study. These values are calculated using a first order fit of kinetics reaction rates. a) k values for COD removal for each of the geometries, using the whole duration of the batch study. b) k values for COD removal for each of the geometries, using the first 10 hours of the batch study only, the period in which the most measurements were taken and any suspended biomass growth would still be minimal. c) k values for ammonia removal for each of the geometries, using the first 10 hours of the batch study only. Ammonia concentration was near 0 at 22.5 hours

when the next measurement after 10 hours was taken, but the actual time that ammonia concentration went to zero is unknown.

5.3 Discussion

During the 1000 mg/L COD operational phase (**Figure 5-5a**), high COD removal was achieved in all of the reactors. The removal patterns were similarly high between all of the reactors, with some of the architected carriers possibly having a slight advantage over the conventional carriers. These advantages were still within the standard deviations of the reactors. This high removal was also seen during the 500 mg/L COD operational phase (**Figure 5-6a**). Similarly, ammonia removal was very high in all carriers (**Figure 5-5b**). 10 of the reactors had ammonia removal that was greater than 95%, with only the octet + simple cube, 0.6 mm geometry having an ammonia removal that was 86.0% +/- 25.7%. Both COD and ammonia removal were high in all reactors, suggesting that at high COD concentrations, the carriers are well-equipped to treat the wastewater. Finally, optical density was also measured between all of the reactors (**Figure 5-5c**, **Figure 5-6b**). With this metric serving as a surrogate measure for suspended biomass, a higher value of optical density would correlate to a higher proportion of suspended biomass present in the reactor. All reactors had high optical density, suggesting a high presence of suspended biomass. The conditions of high COD and a relatively long HRT of approximately 2 days were favorable to supporting suspended growth, and therefore limiting the need of the bacteria to form biofilms. Additionally, the reactors were somewhat overdesigned for the size of the biofilm carriers, further making conditions favorable to suspended biomass. This made it difficult to initially assess differences in biofilm performance between the reactors. Therefore, conditions were modified to promote more biofilm and less suspended biomass by reducing the HRT and the COD concentration to 100 mg/L.

Finally, at a 100 mg/L COD concentration, COD (**Figure 5-7**), ammonia (**Figure 5-8**), and optical density (**Figure 5-9**) were once again measured in a similar manner. At a lower COD concentration all of the reactors experienced some loss in removal efficiency, with a smaller fraction of the influent being treated. At a first glance, it appeared that the removal rates were somewhat comparable between all of the geometries, and the error bars, represented as the standard deviations of the individual samples, somewhat overlapping with one another. Aerobic, heterotrophic, COD-removing bacteria are relatively quick growing compared to ammonia removing bacteria (Rittman and McCarty, 2001c). Therefore, these bacteria are more likely to benefit more from being present in both a suspended bacteria form and a biofilm. Due to the presence of suspended bacteria in all reactors, even with more abundant biofilm during this phase, COD performance less likely to be clearly influenced by the design of the carrier than ammonia performance.

It was apparent that all reactors achieved near full ammonia removal at different points during the operating period (**Figure 5-8a**). Therefore, this ammonia removal was assessed more carefully by comparing it to the surface area available to the carrier (**Figure 5-8b-c**). When comparing the conventional carriers to the architected carriers, it is apparent that 3 carriers, the octahedron, 0.4 mm, the octet + simple cube, 0.4 mm, and the octet + simple cube, 0.6 mm, all achieved faster ammonia removal than the conventional carriers did. What is also seen is that they

achieved this much less surface area available on the carrier. The octahedron, 0.4 mm geometry in particular had a surface area of about 155,000 mm², compared to the 729,000 mm² available to the conventional carriers. This is approximately 21% the surface area of the conventional carriers. This suggests that surface area may not be the most important design consideration when designing biofilm carriers. Architecture seems to play a role in efficient treatment.

Additionally, the ammonia removal took much longer to reliably establish itself than the COD removal, which was established throughout the study. Ammonia oxidizing bacteria (AOB) require longer solids retention times (SRTs) to grow within a community because they have slower specific growth rates when compared to heterotrophic bacteria (Rittmann and McCarty, 2001d). Therefore, AOBs would be more likely to grow in the form of a biofilm because they would be better-retained in the system. The time to establish near full removal (greater than 95%), appeared to be inversely correlated to the available surface area, with larger available surface area seeming to yield faster establishment of AOB populations that remove nearly all available ammonia. This trend was seen in both 0.4 mm geometries and the 0.6 mm geometries. However, more research would be needed before it can be concluded that there is a direct correlation between the two variables. More geometries spanning a larger range of surface areas could be explored. Additionally, while there does seem to be a trend, there is some scatter in the trend, making it difficult to conclude definitively that the time to achieve full ammonia removal is correlated with surface area.

Finally, the optical density was also explored for this phase (**Figure 5-9**). The conventional carriers had the highest presence of suspended biomass compared to the architected carriers. Additionally, the conventional carriers also had settled biomass consistently develop in the corners of the reactor (**Figure 5-10**). This biomass was likely the result of biofilm growing on the conventional carriers but then becoming detached and settling. Because removal of the reactor was a function of both the suspended biomass and the biofilm's removal capabilities, having a larger presence of suspended biomass (conventional carriers) would likely mean less biofilm efficiency. Several of the architected carriers yielded similar, if not higher, removal of both COD and ammonia, with less suspended and settled biomass, suggesting higher biofilm efficiency. However, it was impossible to directly measure the removal of just the biofilm in this study due to the presence of the suspended bacteria. Therefore, a batch study was conducted to assess the performance of the biofilm only.

The hydraulic retention times between the reactors fell into two categories (**Table 5-2**). Specifically, the octahedron, 0.4 mm, octet + simple cube, 0.4 mm, and the conventional carriers had an HRT that was shorter than those of the other architected carriers. Hydraulic retention time is a variable that certainly affects the solids retention time of biomass in the system, as solids recycling was not conducted in this study. Therefore, the SRT of suspended biomass was directly dependent on the HRT of the system. However, when comparing the conventional carriers to just the two architectures with similar HRTs, the same conclusions of this work still hold. COD removal between the three phases of continuous operation were similar between the three cases. In the 1000 mg/L case, where suspended biomass was present in all reactors in abundance, ammonia removal was also similar. However, in the 100 mg/L case, where biofilm was apparent,

the architected carriers were able to achieve near-full ammonia removal at a time sooner than the conventional carriers, despite having less available surface area.

In the second batch study, COD and ammonia removal over time were analyzed (**Figure 5-11**). The batch study was conducted over a short time period to prevent the accumulation of suspended biomass. The relatively stable performance of the control in both studies confirmed that there was not an abundance of suspended growth during the short time scale of this study. Additionally, in both the ammonia and COD removal plots, it can be seen that all of the architected carriers outperformed the conventional carriers. In terms of COD removal, the body-centered cubic + simple cube, 0.4 mm was the most efficient. In terms of ammonia removal, the octahedron, 0.6 mm was the most efficient. While the conventional carriers had an overall surface area of 729,000 mm², the body-centered cubic + simple cube, 0.4 mm geometry had an overall surface area of 194,800 mm², and the octahedron, 0.6 mm geometry had an overall surface area of 233,200 mm². The body-centered cubic + simple cube, 0.4 mm geometry had a surface area that was 27% of the conventional carriers, while the octahedron, 0.6 mm geometry had a surface area that was 32% of the conventional carriers. Despite the fact that the architected carriers had much smaller surface areas when compared to the conventional carriers, they were able to achieve much better biofilm performance, suggesting that architecture is in fact an important design consideration when designing a biofilm carrier. Not only did these carriers have surface areas that were smaller than those of the conventional carriers, they did not even have the highest surface areas when compared to the other architected carriers (**Table 5-1**).

After looking at the removal of COD and ammonia vs. time for each of the carriers, more careful attention was given to the carriers' removal characteristics over the first 10 hours. First, COD removal was explored. Once again, it should be stressed that all of the architected carriers had better COD removal than the conventional carriers (**Figure 5-12**). This was despite the fact that the conventional carriers had a larger surface area available for growing biofilm than all of the architected carriers. In fact, the body-centered cubic + simple cube, 0.4 mm, the geometry that had the best COD performance, had a surface area of about 194,800 mm², only 27% the total surface area of the conventional carriers. When COD removal over 10 hours is normalized by the surface area of the carriers, all of the architected carriers had more removal per unit surface area than the conventional carriers did. Additionally, there did not seem to be a strong correlation between the amount of COD removed per hour and surface area in any of the carriers, suggesting that surface area may not be the only controlling parameter in the efficiency of the biomass. It seems that the architecture of the geometries is in fact playing a role in biofilm performance in terms of COD removal, with more efficient placement of struts yielding better biofilms than simply designing a carrier with high surface area.

Ammonia removal was also assessed more carefully in a similar manner to COD removal. Like COD removal, all of the architected carriers had better performance when compared to the conventional carriers (**Figure 5-13**). The highest performing geometry, the octahedron, 0.6 mm, had a surface area of 233,200 mm², about 32% the surface area of the conventional carriers. Once again, these removal values were normalized by surface area, and the conventional carriers had the lowest ammonia removal per unit surface area. Like in the COD removal data, the ammonia

removal data was not correlated with surface area. However, there did seem to be negative relationship between ammonia removal and surface area. As surface area was increased, the amount of ammonia removal in both the 0.4 mm and 0.6 mm graphs seemed to decline when plotted against the surface area of the carrier. However, it should be noted that only 5 of each type of geometry were studied and therefore it is still early to conclude that there is a direct correlation between increasing surface area and reduced ammonia removal in architected carriers. It does seem to warrant future evaluation. Additionally, when looking at ammonia removal per unit surface area, it seems that geometries with less surface area were more efficient per unit surface area. This finding does suggest that, as seen in the COD removal data, increased surface area did not equate to better ammonia removal. The architecture of the strut configuration played a valuable role in better-performing biofilm.

Both COD and ammonia removal are important to the operation of a wastewater treatment plant. Additionally, many plants are tasked with removing other constituents that were not explored in this study. However, with the two contaminants explored in our study, there is still value in seeing how each carrier removed COD and ammonia in relation to the other 10 carrier types. In **Figure 5-14**, the performance of each carrier, in terms of both COD (X-axis) and ammonia (Y-axis) removal, was plotted in relation to the average COD and ammonia removal of all 11 carriers (as indicated by the vertical and horizontal lines). The conventional carriers, as already analyzed in previous figures, had the worst performance. Compared to the average COD removal of all 11 carriers, the conventional carriers removed about 20% as much COD. Compared to the average ammonia removal of all 11 carriers, the conventional carriers removed about 41% as much ammonia. Geometries that are more to the right of this plot were better at removing COD from the batch study, while geometries that are higher up on the plot were better at removing ammonia. The top right corner was the most efficient region of the plot, with above average COD and ammonia removal. The octet + simple cube, 0.6 mm, octahedron, 0.6 mm, and the body-centered cubic + simple cube, 0.4 mm geometries were the most efficient geometries as they had above average COD and ammonia removal.

In this study, architecture was partially explored. In terms of removal efficiency of biofilm kinetics, topology was the main variable of exploration, and to a lesser extent, so was strut radius. However, all of the geometries studied were periodic in nature, meaning that each carrier was composed of only one topology. However, as seen in **Figure 5-14**, different topologies were better suited to either COD or ammonia removal to varying degrees. It was seen in the batch study that the carrier that achieved the highest COD removal was not the carrier that achieved the highest ammonia removal. In the COD removal data, the body-centered cubic + simple cube, 0.4 mm geometry had the best performance, with 15.8 mg/L-hr COD removed, while in the ammonia removal data, the octahedron, 0.6 mm geometry had the best performance, with 0.86 (mg/L-hr)-N removed. There is no rule that the architectures have to be designed with only one topology. This was done in this study only because it seemed the logical starting place. Additionally, there is also no rule that all unit cells have to be the same size, or that the whole carrier has to be designed with unit cells filling the whole volume. For example, were a carrier to be designed larger, tunnels where there are no struts could be created that allow for wastewater to circulate through the carrier and reach sections of the biofilm that otherwise may be diffusion limited. Concentrated areas of

unit cells could be established for one type of removal and larger unit cells could be established for other types of removal. However, in this study, only topology was explored, so future work should involve a deeper exploration of how different architectural considerations affects biofilm performance and structure.

After completing the batch study, the biofilm present on the carriers was quantified by oven-drying and measuring the amount of dry biomass present (**Figure 5-15**). It appeared that the dry biomass was positively correlated with surface area in both the 0.4 mm and 0.6 mm geometries. This does suggest that increasing surface area seems to promote more biofilm formation. However, this increased quantity of biofilm did not correlate with higher performing biofilms, with the conventional carriers performing poorly in terms of COD and ammonia removal (**Figure 5-11**). Additionally, we have seen that topologies like the simple cube and octahedron, which had lower surface areas relative to the other carriers, had relatively high performing ammonia removal (**Figure 5-13**). Therefore, it appears that carriers that are designed with high surface area do seem to promote more biomass, but the architecture of the carrier seems to promote higher efficiency of the biofilm.

The biofilm kinetics were estimated using first order reaction rates after the batch studies were conducted (**Figure 5-16**). There was generally no pattern between surface area and the kinetics found on the COD biofilm. Most of the geometries had relatively similar performance. Over the whole study, the octet + simple cube, 0.6 mm seemed to have the highest kinetics. However, when looking at the first 10 hours, during which the most measurements were taken, the body-centered cubic + simple cube had the best kinetics. Because this geometry went to zero COD during the first 10 hours, including more data after the fact, as was done in the graph considering the whole study, skewed the kinetics of this biofilm to seem worse than they were. The conventional carriers had the lowest biofilm kinetics, suggesting that they were less well-equipped to treat the COD than were the carriers. Additionally, the COD kinetics were similar between the architectures over the whole batch study, suggesting that architecture may play less of a role in COD removal.

Ammonia removal did seem to yield a difference between the architectures. The kinetics values were generally highest in the simple cube, the octahedron, and the body-centered cubic + simple cube architectures compared to the other architectures, and the conventional carriers. These geometries had both the lowest surface area as well as the lowest coordination numbers, making them the geometries with the most open space. The octahedron, 0.6 mm architecture had a kinetics, k , value of 0.123 hr^{-1} , compared to a value of 0.033 hr^{-1} for both the octet, 0.4 mm, and the octet, 0.6 mm. For the conventional carriers, this kinetics value was found to be even lower, at a value of 0.027 hr^{-1} , which was the lowest kinetics value for ammonia removal when compared to all of the 3D printed, architected carriers. Generally, as surface area was increased on the carriers, the carriers became less effective at removing ammonia. The coordination number, and subsequently the number of struts present in an architecture, was also increased through increasing surface area. It seemed that architectures that had more void space through less relative density and a lower coordination number yielded biofilms with better ammonia removing kinetics.

Ultimately, we were successful in proving our second hypothesis, which was that 3D printing could be used to develop architected biofilm carriers that could achieve a biofilm that yields better removal of ammonia and COD for use in a wastewater treatment setting. Additionally, the communities of bacteria that formed on these carriers could achieve enhanced biofilm performance beyond those of conventional, non-architected carriers. Under high COD operating conditions, the architected carriers were capable of removing nearly all of the ammonia and COD present in the wastewater. At lower COD operating conditions with less suspended biomass, we saw improved times to achieve ammonia removal with carriers having less surface area available when compared to conventional carriers. After more carefully assessing the performance of the biofilms present on both the architected and conventional carriers, we saw that the architected carriers had biofilms that could remove more COD and ammonia than the conventional carriers. This was despite the fact that the conventional carriers had the most surface area available to them, and that they had more biomass than most of the architected carriers. This meant that the architected carriers yielded biofilms were more efficient than the conventional carriers in removing COD and ammonia, both per unit surface area and per unit biomass. The architecture of the carriers seemed to have more influence on the performance of the biofilms in a wastewater treatment setting than did the surface area of the carrier alone.

6. Biofilm Volume Quantification

Our first hypothesis was that different architectures would yield different biofilm structures to form on different 3D-printed architected biofilm carriers. This means that different geometries could yield different amounts of biofilm to form on the carrier. In **Section 4** of this thesis, we attempted to qualitatively assess the structures of the biofilms that formed on different architectures. However, we could not quantify the biofilm accurately using this technique, as we only had two-dimensional data. Subsequently, we assessed the treatment performance of the biofilms that formed on the carriers in **Section 5** of this thesis. Therefore, to quantitatively assess

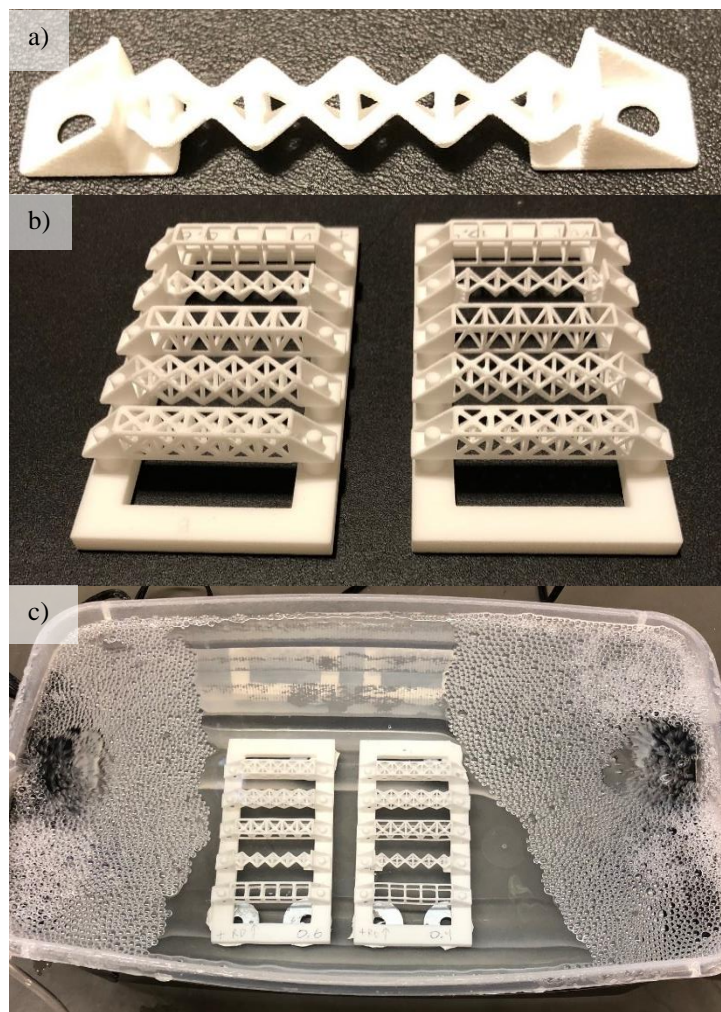


Figure 6-1: Architectures used for Micro-CT study. a) Example of one of the carriers used (Octahedron, 0.4 mm). b) Example of the holding racks used, with the carriers placed in the rack. c) The reactor that housed the carriers where biofilm would ultimately form on them.

located in the Life Sciences building at UMass Amherst). Therefore, to make these carriers fit into the sample holder, they were designed with an 8 mm unit cell length, rather than the 10 mm unit cell length used in the treatment studies (**Section 5**). The unit cell was repeated three times in

the volume of the biofilm that formed on the 3D printed architectures, micro-CT technology was used. Micro-CT, or micro computed tomography, uses X-rays to visualize an object in 3 dimensions. It is similar to the CT technology used in biological settings like hospitals, but it can image objects at a much smaller scale. This three-dimensional rendering of physical objects allowed us to be able to quantify the biofilm volume that formed on our 3D printed architectures. Specifically, micro-CT technology allowed us to test our third research question: What effect does the architecture of the biofilm carrier have on the structure of the biofilm that develops on the architected carriers?

6.1 Methods

To assess how biofilm structure differed with the architecture of the carrier, 10 carriers were 3D printed. The same topology and strut radii combinations were chosen as in the treatment performance study. However, these carriers were designed specifically such that they could fit into an *In-Vivo* X-Ray Microtomograph (Bruker MicroCT SkyScan 1276,

length to provide three unit cells-worth of biofilm volumetric data. Each carrier was fitted with two holding point at the ends of the carrier such that it could fit into a holding rack during the biofilm growth stage. Therefore, two additional unit cells were provided at both ends of the three main unit cells, such that the three central unit cells would not be affected by the edge holding points (**Figure 6-1**). **Table 6-1** provides a detailed overview of the geometric characteristics of the carriers used in this study.

Table 6-1: Geometric characteristics of the carriers used in Micro-CT

Carrier	Abbreviation	Surface Area of One Unit Cell (mm ²)	Solid Volume of One Unit Cell (mm ³)	Coordination Number
Simple Cube (0.4 mm)	S-4	192.2	60.0	6
Simple Cube (0.6 mm)	S-6	275.7	108.6	6
Octahedron (0.4 mm)	O-4	268.8	34.1	8
Octahedron (0.6 mm)	O-6	377.3	76.8	8
Body-Centered Cubic + Simple Cube (0.4 mm)	B-4	401.2	84.8	11
Body-Centered Cubic + Simple Cube (0.6 mm)	B-6	601.9	190.7	11
Octet (0.4 mm)	OT-4	536.2	102.4	12
Octet (0.6 mm)	OT-6	721.1	230.3	12
Octet + Simple Cube (0.4 mm)	OS-4	791.9	150.6	13.5
Octet + Simple Cube (0.6 mm)	OS-6	1131.0	338.9	13.5

The X-ray microtomograph was capable of taking many X-ray images of the carriers with biofilm on them, rendering these images into a 3D model, and quantifying the biofilm on each of the carriers. This was achieved via the concept of back projection. Optical microscopy can only provide two-dimensional information. Additionally, the method can only detect what is visible. Therefore, objects that are obstructed can not be seen using optical microscopy. However, X-ray scans use measured absorbance through objects to image objects. Differences in object density are what is detected by this method, with denser objects absorbing more radiation. In a single scan, one X-ray image from one vantage point is taken. This scan is taken in a conical orientation (**Figure 6-2c**). In the scanning technique used in this study, this scanner is rotated after each scan at a defined rotation angle, and many images are taken. Because the machine measures absorbance and keeps track of the angular rotation where each scan is conducted, the images can be reconstructed using the concept of back projection (**Figure 6-2b**). This can be accomplished using a reconstruction software, which can relate the absorption and measured positions to volume and intensity, allowing a 3D model of the original scan to be generated. Finally, because there is overlap between the many X-ray scans, there is some blurriness that can occur around the objects scanned. Therefore, the software is capable of applying a convolution (**Figure 6-2a**) that can increase the contrast between the object that was scanned and the background (Bruker, 2017). A more detailed description of how the software for the microtomograph was used during scanning will be provided.

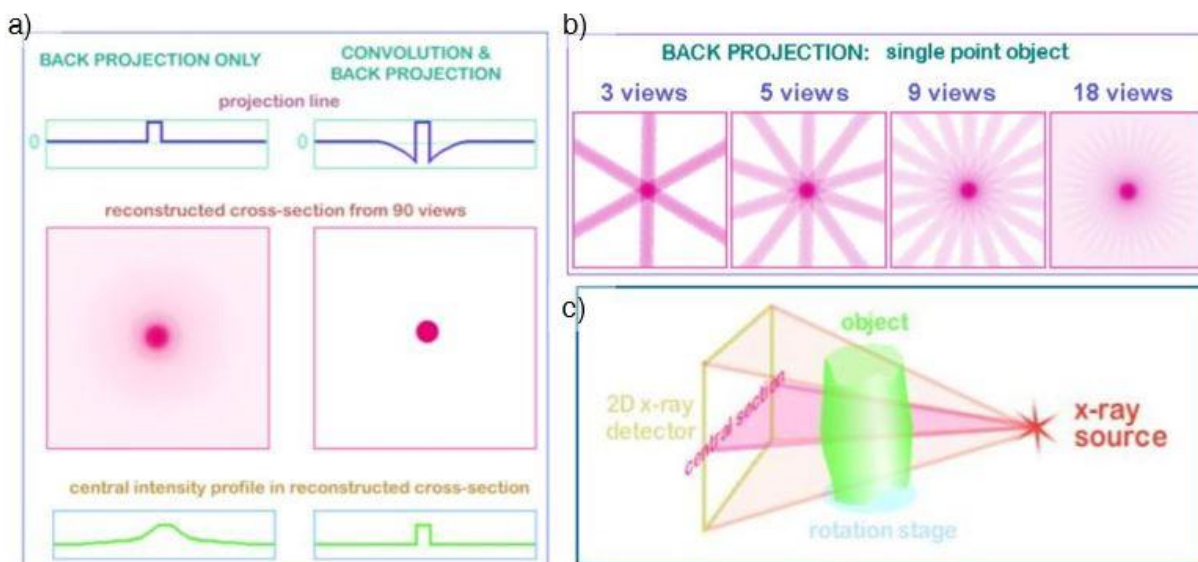


Figure 6-2: Back projection, convolution, and object scanning. Retrieved from (Bruker, 2017).

a) Concept of how convolution can be applied to a back projection to improve contrast of scanned model. b) Schematic of how back projection allows many views or scans of an object to provide a 3D replication of the object. c) Schematic of how a scan is conducted at a single rotation step.

Prior to beginning the growth of biofilm, each of the carriers was carefully measured with a caliper. Each strut was serialized within a unit cell and all of the struts were measured. These readings were then used to determine the surface area and volume of the three central unit cells, which were the unit cells analyzed with the Micro-CT software. Some struts were impossible to directly measure due to the fact that they were in the center of the geometry and were covered by external struts. Therefore, it was assumed that these struts had diameters that were the average of the readings obtained by the measurable struts. Details of the serialization structure used to distinguish struts can be viewed in the appendix.

The goal of this study was to use this Micro-CT technology to assess the structure of the biofilm that formed on the carriers, not to assess their treatment capacity. Therefore, all of the carriers were placed in the same reactor. This reactor included two aquarium air pumps to ensure excess of oxygen to the biofilms. COD was fed to the biofilms in the form of acetate, and was fed via a synthetic media solution, as outlined in **Table 6-2**. This media solution was high in COD (1000 mg/L) compared to the last phase of the continuous flow study. A total of 3 biofilm studies were conducted, as described in **Table 6-3**. The first two were conducted under similar conditions, where each biofilm was grown under batch conditions, with the solution being refreshed as COD was depleted. The third biofilm study was a continuation of the second biofilm study, with further growing time being given after the second scan via Micro-CT. The biofilms were inoculated using 50 mL of activated sludge from the Amherst wastewater treatment plant. After biofilms reached the time outlined in **Table 6-3**, the reactor was transported from the Engineering Laboratory II at UMass Amherst to the Life Sciences building.

Table 6-2: Chemicals used throughout micro-CT study

Compound	4 mM Phosphate Buffer – Chemical Concentration
Sodium Phosphate Dibasic Anhydrous	0.14 g/L
Potassium Phosphate Monobasic	0.21 g/L
Ammonium Chloride	0.05 g/L
Magnesium Sulfate Heptahydrate	0.025 g/L
Potassium Acetate	1.65 g/L
Trace Mineral Solution	1 mL/L
Calcium Iron Solution	1 mL/L

Table 6-3: Descriptions of biofilms analyzed using Micro-CT

	First Biofilm Study	Time 1 - Second Biofilm Study	Time 2 - Second Biofilm Study
Biofilm Age (Days)	51	46	69
Number of Feedings	18	18	21
First or Second Biofilm	First	Second	Second

Each carrier was placed in the microtomograph so that its volume could be quantified. The sample holder was capable of holding two carriers in it, so two carriers were scanned during a single run. The sample holder was then inserted into the microtomograph machine and the door was securely closed. A 0.25 mm Al filter was used during scanning, with a voltage of 55 kV and a current of 72 μ A. The exposure time was set to 370 ms. The overall resolution chosen was 1008x672, with a 26.1 μ m exposure. These were chosen to balance having higher resolution while maintaining reasonable scan times (~30 min), to allow the biofilms to be placed back in their hydrated states. During scanning, X-rays were taken at 0.3° increments, with 2 scans taken at every rotation step and averaged together during reconstruction.

After scanning was completed, the images were reconstructed into a 3D model using NRecon, which is a part of the Bruker software package. First, the region of interest (ROI) was set such that a little more than the three central unit cells were selected. The region of interest would be refined further in the analysis software, CT-An. After selecting the region of interest, the lineup was adjusted to ensure that the images lined up to prevent misalignment. Mismatching occurs when the centerline of what is scanned by the X-ray camera does not line up exactly with the virtual centerline of the object being scanned (Bruker, n.d.). Compensation can be added in the software to realign parts of the volume that are mismatched. The software first calculated a default value, then this value was adjusted as needed by previewing sections of the volume and ensuring that the alignment was correct. The software was then run to reconstruct the X-ray scans into a model of the specimen.

Once the 3D rendering was completed, CT-An was used to perform quantification on the biofilm. The volume was quantified individually for each of the three unit cells of interest. As

mentioned, the VOI selected in NRecon was refined further to include just one unit cell at a time. This unit cell was selected from the outermost sections of struts that formed a unit cell of a topology as outlined in **Figure 4-2**. For example, the unit cell selected of the simple cube includes all of the struts defined by the simple cube topology. Therefore, two unit cells next to each other that share a strut would have the shared strut selected in both analyses. Due to the hydrated state of the biofilm, the bottom half of the carrier was left with more water than the top half. Therefore, only the top half of the biofilm and carrier were selected for analysis, and the bottom half was extrapolated by multiplying the obtained results by 2. The midpoint of each carrier was carefully measured using the in-software measuring tool and was the boundary of the volume of interest (VOI). This volume was then binarized using the software's automatic thresholding capability. This threshold was selected such that all of the biofilm-water mixture and the carrier were rendered white and the background air was rendered black. Once the threshold was defined, the morphometry feature was used to quantify the biofilm volume and surface area by quantifying the 3D characteristics about the white area. From this, volume and surface area characteristics were used for further analyses. As this volume included both the biofilm and the carrier for just the top half of the carrier, it was multiplied by 2 and the known carrier volume was subtracted from it.

After quantifying the results of the Micro-CT biofilm volume analyses, a principle component analysis (PCA) was conducted using R software (R Core Team, 2019) to compare both the results of the Micro-CT study and the results of the biofilm performance study to the geometric characteristics of the carriers themselves. The variables used in this analysis, and their descriptions, can be viewed in **Table 6-4**. Due to the limited number of variables that could be included in the PCA, only the time 2, second biofilm Micro-CT scan data was included here. The PCA plot provides two dimensions, which are composites of the variables inputted to the PCA. These dimensions are selected by the software such that they account for the maximum amount of variance in the data that could be explained by two dimensions. The closer the individual vectors that correspond to each variable are to this circle, the more impact they have in explaining the variance. However, the shorter these vectors are, and subsequently the further they are from the circle, the less impact they have in explaining the variance. Any two vectors that have angles close to 0° are positively related, while vectors that have angles of 180° are negatively related. Finally, vectors with angles of 90° are not related to each other.

Table 6-4: Variables used in the Principle Component Analysis and Their Meanings

Variable	Meaning
Weight Biomass	Weight of biomass from after batch study, after oven drying (g)
Hydrated Biomass	Weight of biomass after batch study, before oven drying (g)
Number of Struts	Number of struts in a cube carrier
Cube Surface Area mm ²	Surface area of a cube carrier (mm ²)
MicroCT mm ³ Third Scan	Volume of biofilm obtained in the third micro-CT study, per unit cell (mm ³)
Relative Density	Relative density of a cube carrier
Strut Radius mm	Strut radius of either a cube or micro carrier
COD Removed	COD removed over 10 hours during the second batch study
Ammonia Removed	Ammonia removed over 10 hours during the second batch study
Max Distance Between Nodes Struts	Maximum distance between any two points of a geometry on the cubes (measured from center of strut)

6.2 Results

After running micro-CT studies three times, the biofilm volume for each geometry was quantified. This information can be viewed in **Figure 6-3**. **Figure 6-3a** depicts the volume data for the first micro-CT scan, **Figure 6-3b** depicts the volume data for the second micro-CT scan, and **Figure 6-3c** depicts the volume data for the third micro-CT scan. During the first two scans of biofilm volume, the overall volume of biofilm that formed was relatively low. In the first biofilm study, all geometries had a biofilm volume of less than 100 mm³, with overlap between error bars and no real trend between the geometries. In time 1 of second biofilm study, there was more biofilm present on the carriers, but there was still no visible trend between the geometries. Finally, in time 2 of the second biofilm study, there was the most biofilm compared to the first two studies. The geometries filled the unit cells with biofilm in this study. A trend was observed, that with increasing the number of struts from topology to topology, the biofilm volume generally increased.

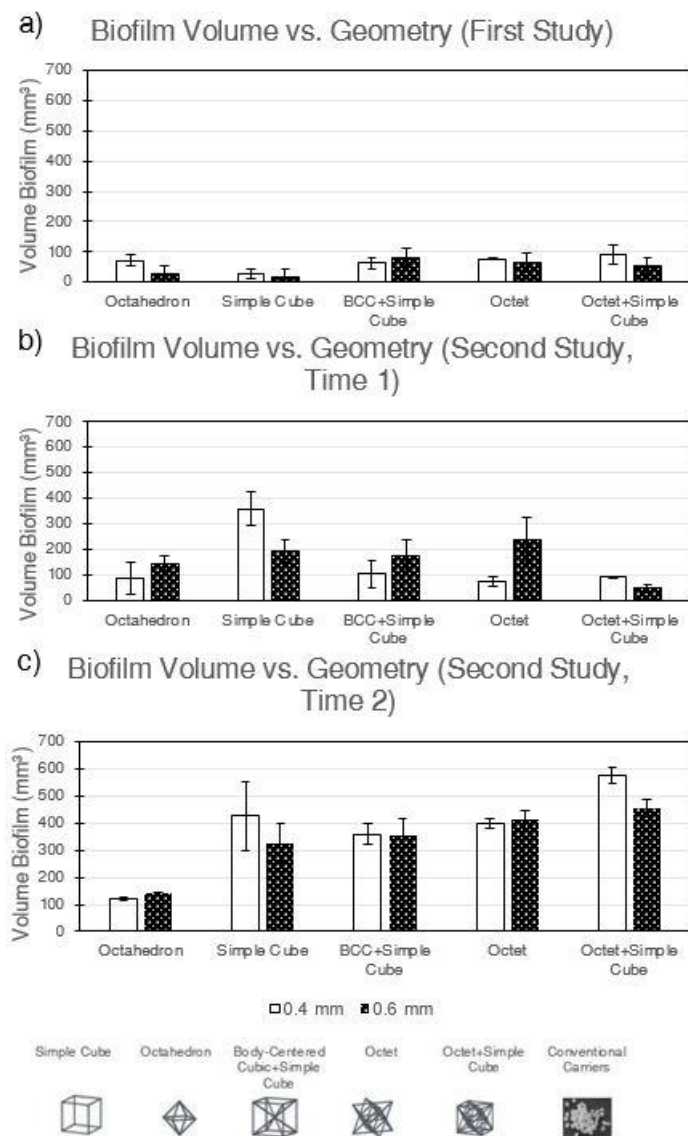


Figure 6-3: Biofilm volume vs. geometry for all 3 micro-CT studies. a) First biofilm study. b) Second biofilm study, time 1. c) Second biofilm study, time 2.

A more detailed view of the biofilm developed during the third micro-CT scan is shown in **Figure 6-4**. In this figure, both the quantitative images exported from the microtomograph and the qualitative volume analysis are presented. Images are provided from the simple cube, 0.4 mm, the body-centered cubic + simple cube, 0.4 mm, and the octet + simple cube, 0.4 mm. These geometries were selected for image selection because they span a spectrum of low to high amounts of struts per unit cell and therefore, a spectrum of surface area as well. These images include screen shots of the 3D models generated, as well as cross-sections throughout a single unit cell. The quantitative information provided in this figure is a plot of biofilm volume per unit cell vs. the surface area of one unit cell of the carrier.

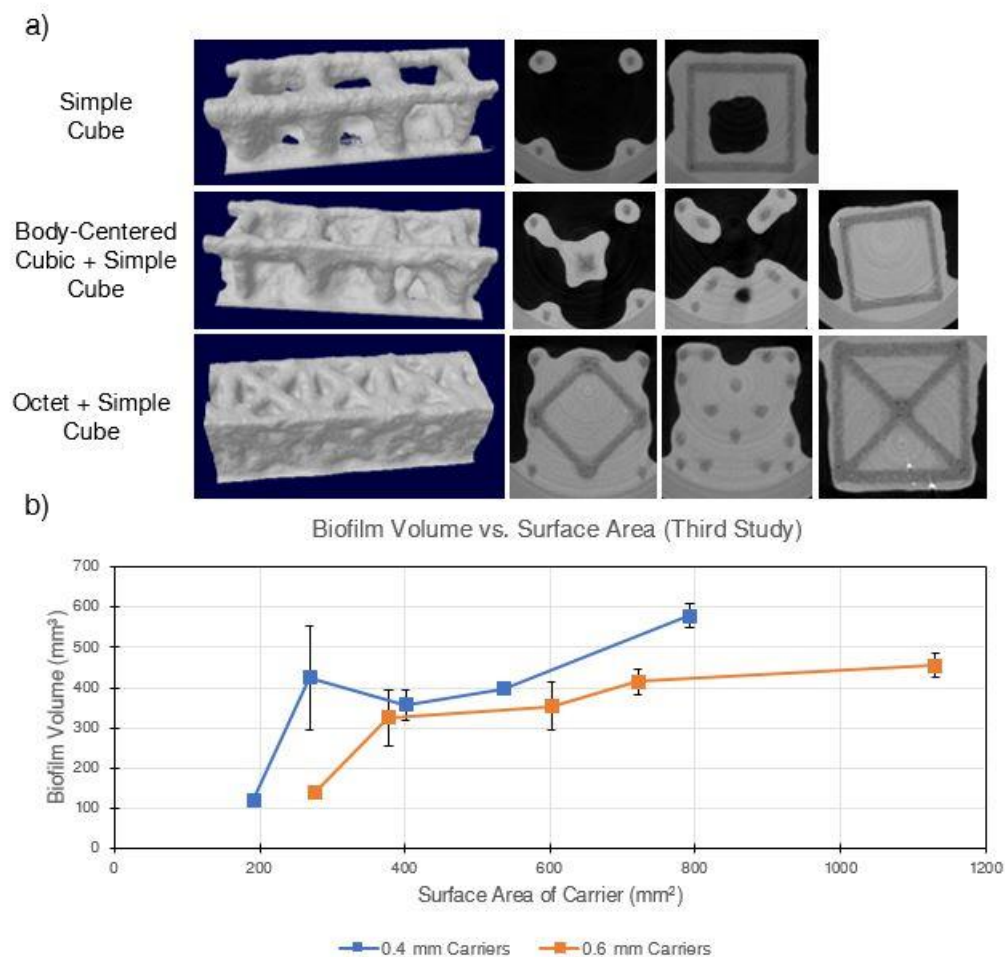


Figure 6-4: Biofilm volume vs. surface area for the third Micro-CT study. a) On the left side are pictures of the 3D models generated. On the right are cross-sectional two-dimensional images of the lattices taken at various positions throughout one unit cell. Note that as you move from the top to the bottom of the pictures, the number of struts, and the surface area of the carrier, increases. Also note that the geometries shown above are all the 0.4 mm geometries. b) A plot of biofilm volume vs. surface area for the third micro-CT study. Averages represent the average of 3 unit cells, and error bars represent the standard deviations.

The principle component analysis that was conducted is depicted in **Figure 6-5**. The two dimensions are shown are composites of the variables that were inputted into the plot. Dimension 1 accounts for 43.9% of the total variance, while dimension 2 accounts for 23.4% of the total variance, with a total of 67.3% of the variance being explained by the two dimensions in this plot. The circle overlay of the plot represents this 67.3% of explained variance.

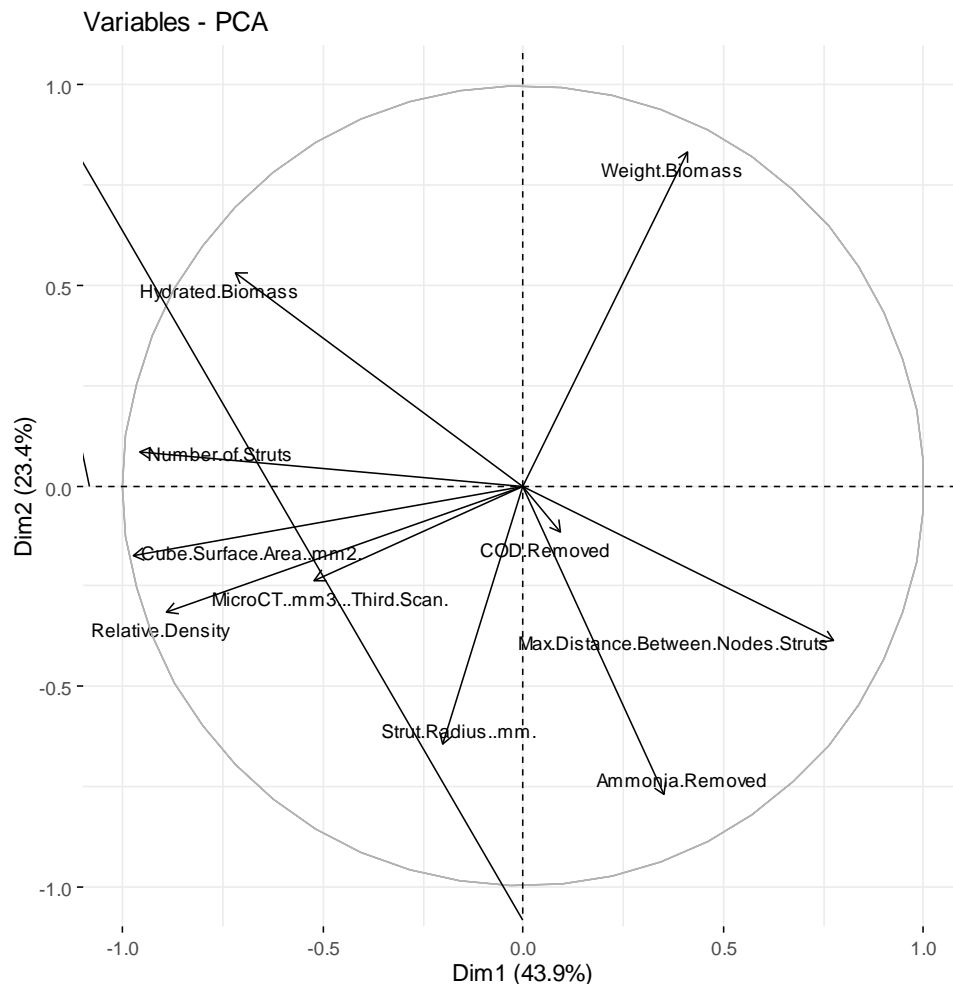


Figure 6-5: Principle component analysis relating biofilm performance, micro-CT, and carrier properties

6.3 Discussion

In the first two biofilm volume scans, the biofilm that developed was similar when compared to other geometries within the same scan. However, the second biofilm generally had more biofilm volume form overall compared to the first biofilm. Each of these biofilms were grown under similar conditions. They were each fed a total of 18 times, meaning that the mass of COD provided to each of the biofilms was the same. The first biofilm was 5 days older than the second biofilm. Therefore, with both biofilms being fed the same amount of times, the second biofilm had an average of 0.39 feedings per day, compared to the first biofilm which had an average of 0.35 feedings per day. This could explain the added biofilm from the second biofilm to the first. However, there were no distinct patterns of biofilm formation between the architectures, as the biofilm volume was minimal on these architectures.

While the first two biofilm scans did not have a lot of biofilm formed, the third biofilm scan did yield a higher biofilm volume. This biofilm was exposed to the most shear of the first two scans, as it was subjected to shear when it was transferred to the Life Sciences building during the

second scan, when it was transferred back to the Engineering Laboratory II, and when it was transferred again to the Life Sciences building for the third scan. This shear exposure may have led to the rise of a more shear-resistant biofilm. Additionally, this biofilm was also allowed to grow for a longer duration with three more feedings, which may have also contributed to the increase in biofilm volume obtained in this scan. The biofilm that was ultimately obtained in the third scan was unique in that this biofilm seemed to conform to fill in most of the unit cells. Additionally, a trend of increasing biofilm volume with increasing the number of struts in the architecture was apparent. Therefore, this effect was further explored in **Figure 6-4**.

Biofilm in the third scan seemed to be positively correlated with the surface area of a single unit cell (**Figure 6-4**). This increase in surface area is achieved by adding more struts to change a topology from one type to another. The increasing trend of surface area was observed in both the 0.4 mm and 0.6 mm geometries. This increasing trend of biofilm volume as the number of struts is increased can also be seen qualitatively in the same figure. Here, 3D models of the simple cube, the body-centered cubic + simple cube, and the octet + simple cube topologies are shown. As you move from the top to the bottom of these three models, which is the order of increasing number of struts, the biofilm fills in the cubic space that it occupies more, as you move from top to bottom. For example, the simple cube geometry has biofilm formed around the struts, but there are clear holes that you can see through the structure with. As you move to the body-centered cubic + simple cube geometry, there is more biofilm. The biofilm is still mostly present around the struts, but the structure is now entirely filled with biofilm to the point that there are no holes. Finally, the octet + simple cube geometry has the most biofilm. Not only are there no holes apparent in the structure, but the whole cubic structure of the unit cells are filled in. Adding more struts to the geometry seems to allow for higher connectivity within the architecture, which in turn provides more of a scaffolding for biofilm to occupy the space. This suggests that the architecture does in fact influence the biofilm's structure as it ultimately forms on the carriers. Unlike the biofilms grown during the treatment study in **Section 5** of this thesis, these biofilms were grown in batch conditions, meaning that these biofilms were not exposed to the same shear conditions as the flow-through biofilms.

There was a diminishing effect of increasing biofilm volume with increasing the number of struts. When the surface area is low, small increases in the surface area lead to large increases in the biofilm volume. For example, in the 0.4 mm data, a relatively small increase in surface area from 192 mm² to 269 mm² yielded an increase in biofilm volume from 121 mm³ to 425 mm³. However, at larger surface areas, a relatively large increase in surface area from 269 mm² to 791 mm² yielded an increase in biofilm volume from 425 mm³ to 577 mm³. This was also seen in the 0.6 mm data. A relatively small increase in surface area from 276 mm² to 377 mm² yielded an increase in biofilm volume from 139 mm³ to 375 mm³. However, an increase from 377 mm² to 1130 mm² yielded an increase in biofilm volume from 325 mm³ to 454 mm³. This may be due to the diminished benefit that providing extra scaffolding gives once the existing scaffolding is sufficient. If biofilm is already able to span the distance between two struts, adding a third strut in between is unlikely to have a significant effect. Therefore, the architecture becomes very important as the placement of the struts will lead to optimized biofilm volume without providing too many

struts. It is important to design an architecture that is able to achieve both biofilm volume without reducing the ability of the carrier to allow nutrients to diffuse through it.

It is also important to consider the fact that more biofilm volume does not directly equate to more biofilm treatment. As seen in **Section 5** of this text, biofilms with less surface area and less overall biomass can still achieve highly effective biofilms. Biofilms can have different volumes densities, and the conditions to which they are exposed all play a role in how efficient the biofilm ultimately is at removal. To begin to bridge the gap between the two studies, a principle component analysis was conducted that relates the variables of both the biofilm volume obtained via micro-CT to the efficiency results obtained in the second biofilm performance study. This was described in **Figure 6-5**. It should be noted that the variables given in this figure that pertain to the geometries is based on the cubes, not the carriers used for the micro-CT studies. However, the relative increase from one topology to another in these geometric parameters was similar for both the cubes and the micro-CT carriers. The first relationship that was noticed is that the biofilm volume obtained in the third micro-CT study was correlated with relative density, the surface area of the cube, and the number of struts of the cube carrier. This is in agreement with what was seen visually in **Figure 6-4**, as more support seemed to allow for more biofilm volume to form. Relative density and surface area are both related to the number of struts with the latter having an increasing effect on the former.

The ammonia removal achieved during the batch study seemed to correlate with the COD removal achieved during the batch study, with high values of one leading to high values of the other. However, it should be stressed that the vector length of the COD removal is very short, meaning that it is not well represented by the other variables present. This is also in agreement with what was seen in the treatment study, as COD removal was not correlated with the surface area of the carrier (**Figure 5-12**). There also appears to be some correlation between ammonia removal and both strut radius and distance between struts. This means that larger struts may yield higher levels of ammonia removal. This also means that larger distances, or larger void spaces, may also yield higher levels of ammonia removal. It should be noted however, that this correlation was not as strong as that seen between biofilm volume and the number of struts. However, it was seen in the treatment study that there was some relationship between ammonia removal and surface area, with less surface area yielding higher levels of ammonia removal in the batch study. Geometries with less overall struts, and therefore less carrier surface area, also had larger distances between struts due to the fact that there was less uninterrupted space between two struts. This relationship of better ammonia removal with lower surface area could be due to the fact that more space was available between struts to allow for some form of diffusion of ammonia that the biofilm could then remove. The relationship between ammonia removal and strut configuration seems to warrant future study.

In addition to the positive relationships seen, there were also some inverse relationships seen in the PCA. It seems that the distance between struts was negatively correlated with the amount of hydrated biomass that formed on each of the cubes. This is logical. As the distance between struts is small, biofilm is able to span the distance and attach to multiple struts without collapsing. However, as this distance increases, it must reach some critical point beyond which the

biofilm cannot bridge the gap, and the overall biofilm that would be able to form would be diminished. The other inverse relationship that was seen was that strut radius and the amount of dry biomass that formed were inversely correlated. This would suggest that geometries with smaller strut radii tended to yield more biomass. This was also observed with biofilm volume in the micro-CT study when biofilm was able to grow to a point where it occupied most of the unit cell volume. The geometries with 0.4 mm strut radii had more biofilm volume per unit surface area than the geometries with 0.6 mm strut radii.

In assessing the structure of the biofilm that formed on the architected carriers, we tasked ourselves with using micro-CT to quantify the volume that formed on the biofilm carriers to see what effect modifying the architecture had on these carriers. What we found was that the biofilm volume that formed on a carrier was positively correlated with the number of struts present on an architecture. This correlation was seen when biofilm volumes were large and the unit cells were filled in. However, this effect became diminished as more struts were added. When geometries did not have high connectivity, such as in the octahedron and the simple cube geometries, increasing the surface area by adding struts had a large effect on the increase in biofilm volume. However, as more struts were added, such as in geometries like the octet and the octet + simple cube, the increase in struts only led to marginal increases in biofilm volume, as adding struts became somewhat redundant. The observed trend was that adding more struts to an architecture increases the ability of the geometry to act as a scaffold, which allows for more biofilm to be retained in a given volume. Ultimately, we were successful in achieving our goal of seeing patterns related to the architecture of the biofilm carrier. This pattern was that more struts seem more equipped to retain more biofilm volume as the magnitude of biofilm volume approaches that of occupying the whole unit cell.

7. Conclusions and Future Work

The ultimate objective of this work was to explore the utility of using architected geometries that could be designed by 3D printing to improve treatment performance of a biofilm carrier. The open design space offered by 3D printing allowed us to explore the effect that architecture had on biofilm performance and structure when used in a wastewater treatment plant. To reach this objective, we tasked ourselves with 3 main goals, which were asked in the form of research questions. The first of these questions was as to whether we could use 3D printing to develop architected biofilm carriers that could achieve a higher performing biofilm carrier for use in a wastewater treatment setting. The ultimate answer to this was yes. We were able to 3D print several **architectures that not only outperformed the conventional carriers in terms of COD and ammonia removal, but they did so with less suspended biomass**, as evidenced by the lower optical density readings.

The second research question we tasked ourselves with was assessing how the biofilm performance of the architected carriers could be better than those of the conventional carriers. Ultimately, this was answered by conducting a batch study. This batch study allowed us to separate the biofilm that formed directly on the carriers from any suspended biomass that may have also formed in our reactors. We were able to determine that **the biofilm formed on the architected carriers was more efficient at removing both COD and ammonia than were the conventional carriers**. Additionally, we challenged the idea that maximizing surface area alone is the only way to promote more efficient biofilms. More biofilm could be generated by increasing surface area, but the architecture of the carrier ultimately affected how effective the biofilm was at performing treatment.

Knowing that architecture played a role in the efficiency of the biofilm that formed on the carrier, we tasked ourselves with our third research question, which was to what effect the architecture has on the structure of the biofilm that develops on the architected carriers. Micro-CT was used to answer this question. Biofilms were grown on a small-scale version of the architectures used in the treatment study and analyzed for their volume retention. It was found that **architectures with increased strut connectivity seemed to be better at retaining biofilm volume**. This increased connectivity did become redundant after a point, with increases in surface area via adding struts had only marginal effects on increasing biofilm volume.

These three research questions led us to our ultimate goal of using architecture to improve biofilm carriers. Architecture does in fact seem to play a role in developing improved biofilm carriers for use in a wastewater treatment setting. However, architecture was only explored to a limited extent in this work. There are several areas upon which this work can be improved upon and continued. In this work, the only cross-sectional shape of struts that was explored was a circular cross-section. However, this cross-section could also be something else, such as a cross. Continuing off this concept, corrugations could continue to be added to this cross until it forms a rough, round shape with many ridges. This would allow for increased surface area on the carrier itself, while also preserving the architectural designs of the topology. Additionally, while the size of a unit cell was briefly explored qualitatively in the initial, optical microscopy study, its effects on treatment capability and biofilm structure have yet to be explored. For example, it was observed

that at the size of unit cells that we studied, biofilm is able conform to different architectures and achieve different levels of treatment and biomass retention. However, if this unit cell were increased to a larger size, such as a meter in length, width, and height, it is unknown what effect the architecture might have on the biofilm. It would be important to explore what order of magnitude, if any, does architecture no longer play a role in biofilm formation.

Future study should also involve further assessment of the ammonia removing capabilities of the carriers. It was observed that the ammonia removed during the batch study was inversely correlated with the surface area of the carrier, which was in itself a function of the architecture of the carrier (i.e. how many struts were present in the architecture). However, only 5 data points could be collected for each of the two strut sizes observed (0.4 mm and 0.6 mm). Future work could involve growing biofilm for a fixed period of time under similar conditions and seeing if this trend remains true. This could also be done by adding more architectures. Additionally, this experiment did not give insight into the different microbial populations that developed on the different architectures. Perhaps some carriers developed populations better suited to ammonia removal, while others did not. Future work should involve assessment of these microbial compositions. Additionally, ammonia is not the only contaminant that a wastewater treatment plant must deal with. Future work should also assess other contaminants, such as nitrite and nitrate removal, in addition to ammonia removal.

Finally, this study looked only at periodic architectures, where the same topology was repeated to achieve a 3D printed cube. This was done to begin to assess which architectures were best suited for use as a biofilm carrier. However, such a requirement as periodicity would be imposing a limitation on the open design space that is offered by 3D printing. Future work should most certainly explore the possibility of non-periodic biofilm carriers. It was determined in this work that an architecture that is well suited for one type of biofilm characteristic, such as ammonia removal, may not be best suited for another type of biofilm characteristic, such as COD removal. More treatment variables exist beyond just these two explored in this study. An optimized biofilm carrier architecture would likely involve designing a structure that has different architecture in different sections of the carrier to promote different biofilm interactions to occur. Additionally, in this work, the idea of exploring what happens in internal sections of the biofilm carrier was not explored. The cubes that were designed were relatively small (9 cm x 9 cm x 9 cm). However, to be useful in a wastewater treatment plant, much larger structures, or at least some configuration of many smaller structures, would be needed to achieve and reach significant treatment objectives. Our carriers were relatively small, possibly preventing the possibility that sections of the carrier may become diffusion limited and therefore unable to conduct treatment in these sections. However, a large carrier may become diffusion limited if substrate cannot reach the entire architecture, making large sections of the architecture inefficient. Therefore, another potential design consideration for exploration would be providing tunnels and access points for the wastewater to reach all parts of the biofilm that forms on the carriers. As mentioned earlier, the design freedom offered by 3D printing is enormous. Therefore, our work here has just begun to scratch the surface of what may be possible.

Using architecture to improve biofilm carriers is one avenue of achieving improved wastewater treatment. Biofilm carriers themselves are one of many innovations that can be added to an existing wastewater treatment plant. As described earlier, they offer several benefits over the conventional activated sludge process alone, such as smaller volume requirements, lower hydraulic retention times, less chance of bacteria washout due to heavy weather events, increased resilience to changes in the environment, high biomass retention, high active biomass concentrations, and lower sludge production (Wang et al., 2019). Because biofilms can offer potential benefits over the conventional activated sludge process alone, improving the biofilm carrier can lead to a better biofilm, making gains in treatment even more impressive. It is the hope of the authors that improved biofilm carriers is one of many ways upon which wastewater treatment processes are improved.

Finding cost-effective solutions to wastewater treatment problems is an emerging concern that is unlikely to be going away on its own in recent years. With stricter wastewater treatment regulations likely to come in future years, wastewater treatment plants are tasked with the goal of improving their process to accommodate increased contaminants removal. However, these added expectations often come with limited assistance being given to wastewater treatment plants to achieve these goals. Therefore, wastewater treatment plants need to be able to accomplish more effective treatment without added resources. It is unlikely that there will necessarily be one solution to this problem, but rather a plethora of small solutions that each push the wastewater treatment field further. Low-cost, high benefit solutions are going to be needed as we transition further into the twenty-first century.

8. References

- 10 Advantages of 3D Printing. (2019, May 3). MakerBot.
<https://www.makerbot.com/stories/design/advantages-of-3d-printing/>
- Advanced Digital Design and Fabrication (ADDFab): Core Facilities: UMass Amherst.* (n.d.). Retrieved March 26, 2020, from <https://www.umass.edu/ials/addfab>
- Ai, H., Xu, J., Huang, W., He, Q., Ni, B., & Wang, Y. (2016). Mechanism and kinetics of biofilm growth process influenced by shear stress in sewers. *Water Science and Technology*, 73(7), 1572–1582. <https://doi.org/10.2166/wst.2015.633>
- Ardern, E., & Lockett, W.T. (1914a). Experiments on the Oxidation of Sewage without the Aid of Filters. *Journal of Society and Chemical Industry*, 33, 523-539.
- Ardern, E., & Lockett, W.T. (1914b). Experiments on the Oxidation of Sewage without the Aid of Filters, Part II. *Journal of Society and Chemical Industry*, 33, 1122-1124.
- Ardern, E., & Lockett, W.T. (1915). Experiments on the Oxidation of Sewage without the Aid of Filters, Part III. *Journal of Society and Chemical Industry*, 34, 937-943.
- ASCE (2013). FAILURE TO ACT | THE IMPACT OF CURRENT INFRASTRUCTURE INVESTMENT ON AMERICA'S ECONOMIC FUTURE. Retrieved from https://www.asce.org/uploadedFiles/Issues_and_Advocacy/Our_Initiatives/Infrastructure/Content_Pieces/failure-to-act-economic-impact-summary-report.pdf
- Asbhy, M.F. (2012). “Designing architected materials.” *Scripta Materialia*, 4-7.
- Bacalhau, J., Cunha, T., & Afonso, C. (2017). Effect of Ni content on the Hardenability of a Bainitic Steel for Plastics Processing. *24th ABCM Congress of Mechanical Engineering*. <https://doi.org/10.26678/ABCM.COBEM2017.COB17-1174>
- Banashek, L. (2019). Review of the Medical and Environmental Implications of Additive Manufacturing (3D Printing) Filaments. *Anesthesia & Analgesia*, 128, 13-15.
- Barakh Ali, S. F., Mohamed, E. M., Ozkan, T., Kuttolamadom, M. A., Khan, M. A., Asadi, A., & Rahman, Z. (2019). Understanding the effects of formulation and process variables on the printlets quality manufactured by selective laser sintering 3D printing. *International Journal of Pharmaceutics*, 570, 118651. <https://doi.org/10.1016/j.ijpharm.2019.118651>
- Bassin, J. P., Abbas, B., Vilela, C. L. S., Kleerebezem, R., Muyzer, G., Rosado, A. S., van Loosdrecht, M. C. M., & Dezotti, M. (2015). Tracking the dynamics of heterotrophs and nitrifiers in moving-bed biofilm reactors operated at different COD/N ratios. *Bioresource Technology*, 192, 131–141. <https://doi.org/10.1016/j.biortech.2015.05.051>
- Bassin, J.P., Kleerebezem, R., Rosado, A.S., van Loosdrecht, M.C.M., & Dezotti, M. (2012). Effect of Different Operational Conditions on Biofilm Development, Nitrification, and Nitrifying Microbial Population in Moving-Bed Biofilm Reactors. *Environmental Science & Technology*, 46(3), 1546-1555. <https://doi-org/10.1021/es203356z>

- Bolton, J., Tummala, A., Kapadia, C., Dandamudi, M., & Belovich, J. M. (2006). Procedure to quantify biofilm activity on carriers used in wastewater treatment systems. *Journal of Environmental Engineering*, 132(11), 1422–1430. [https://doi.org/10.1061/\(ASCE\)0733-9372\(2006\)132:11\(1422\)](https://doi.org/10.1061/(ASCE)0733-9372(2006)132:11(1422))
- Borisenko, D. N., Borisenko, E. B., Zhokhov, A. A., Redkin, B. S., & Kolesnikov, N. N. (2019). Equipment and a Technique for Manufacturing Shaped Products from Refractory Metals Using the 3D-Printing Method. *Instruments and Experimental Techniques*, 62(6), 862–866. <https://doi.org/10.1134/S0020441219050154>
- Brechet, Y., and Embury, J.D. (2012). “Architected materials: expanding materials space.” *Scripta Materialia*, 1-3.
- Bruker. (2017). *In-Vivo X-Ray Microtomograph SkyScan 1276 V1.3: User Manual*. Kontich, Belgium: Author
- Bruker. (n.d.). An overview of NRecon: reconstructing the best images from your microCT scan: User Manual. Kontich, Belgium: Author
- Chang, I., Gilbert, E. S., Eliashberg, N., & Keasling, J. D. (2003). A three-dimensional, stochastic simulation of biofilm growth and transport-related factors that affect structure. *Microbiology-Sgm*, 149, 2859–2871. <https://doi.org/10.1099/mic.0.26211-0>
- Chopp, D. L., Kirisits, M. J., Moran, B., & Parsek, M. R. (2002). A mathematical model of quorum sensing in a growing bacterial biofilm. *Journal of Industrial Microbiology and Biotechnology*, 29(6), 339–346. <https://doi.org/10.1038/sj.jim.7000316>
- Christen, K. (2003). Infrastructure Outlook Still Troubling, New Reports Find. *Water Environment & Technology*, 15(12), 23–25. Retrieved from JSTOR.
- Coroneo, M., & Yoshihara, L., & Wall, W.A. (2014). Biofilm growth: A multi-scale and coupled fluid-structure interaction and mass transport approach. *Biotechnology and Bioengineering - Wiley Online Library*. (n.d.). Retrieved May 8, 2019, from <https://onlinelibrary-wiley-com.silk.library.umass.edu/doi/full/10.1002/bit.25191>
- Cowle, M. W., Webster, G., Babatunde, A. O., Bockelmann-Evans, B. N., & Weightman, A. J. (2019). Impact of flow hydrodynamics and pipe material properties on biofilm development within drinking water systems. *Environmental Technology*. <https://doi.org/10.1080/09593330.2019.1619844>
- Cox, S. C., Jamshidi, P., Eisenstein, N. M., Webber, M. A., Burton, H., Moakes, R. J. A., Addison, O., Attallah, M., Shepherd, D. E. T., & Grover, L. M. (2017). Surface Finish has a Critical Influence on Biofilm Formation and Mammalian Cell Attachment to Additively Manufactured Prosthetics. *Acs Biomaterials Science & Engineering*, 3(8), 1616–1626. <https://doi.org/10.1021/acsbomaterials.7b00336>
- Cz Garden Supply. Amazon.com: K1 Filter Media PREMIUM GRADE Moving Bed Biofilm Reactor MBBR. Fresh, Virgin, NOT Recycled. Creates Most Robust Good Bacteria

- Colonies. Perfect for Aquariums • Aquaponics • Aquaculture • Ponds: Gateway. (n.d.). Retrieved April 6, 2020, from https://www.amazon.com/Aquaponics-Aquaculture-Hydroponics-Garden-Supply/dp/B014R96C0G/ref=sr_1_6?keywords=k2%2Bmbr&qid=1551208316&s=gateway&sr=8-6&th=1
- Dimensional accuracy of 3D printed parts.* (n.d.). 3D Hubs. Retrieved March 26, 2020, from <https://www.3dhubs.com/knowledge-base/dimensional-accuracy-3d-printed-parts/>
- Dirchx, P. (2013). *Figure 2. A schematic diagram of the stages of biofilm formation from attachment to detachment...* ResearchGate. Retrieved March 31, 2020, from https://www.researchgate.net/figure/A-schematic-diagram-of-the-stages-of-biofilm-formation-from-attachment-to-detachment_fig1_259210319
- Elliott, O., Gray, S., McClay, M., Nassief, B., Nunnelley, A., Vogt, E., Ekong, J., Kardel, K., Khoshkhoo, A., Proaño, G., Blersch, D.M., & Carrano, A.L. (2017). Design and Manufacturing of High Surface Area 3D-Printed Media for Moving Bed Bioreactors for Wastewater Treatment. *Journal of Contemporary Water Research & Education*, 160(1), 144-156. <https://doi-org.silk.library.umass.edu/10.1111/j.1936-704X.2017.03246.x>
- Emelogu, A., Marufuzzaman, M., Thompson, S. M., Shamsaei, N., & Bian, L. (2016). Additive manufacturing of biomedical implants: A feasibility assessment via supply-chain cost analysis. *Additive Manufacturing*, 11, 97–113. <https://doi.org/10.1016/j.addma.2016.04.006>
- EOS Manufacturing Solutions (n.d.), Materialdatacenter.com. Retrieved April 6, 2020, from <https://eos.materialdatacenter.com/eo/en>
- Esser, D. S., Leveau, J. H. J., & Meyer, K. M. (2015). Modeling microbial growth and dynamics. *Applied Microbiology and Biotechnology*, 99(21), 8831–8846. <https://doi.org/10.1007/s00253-015-6877-6>
- EXTRUSION: Orientation: The Good and the Bad.* (n.d.). Retrieved March 27, 2020, from <https://www.ptonline.com/articles/extrusion-orientation-the-good-and-the-bad>
- Falletti, L., & Conte, L. (2007). Upgrading of Activated Sludge Wastewater Treatment Plants with Hybrid Moving-Bed Biofilm Reactors. *Industrial & Engineering Chemistry Research*, 46(21), 6656–6660. <https://doi.org/10.1021/ie061635v>
- Felföldi, T., Jurecska, L., Vajna, B., Barkacs, K., Makk, J., Cebe, G., Szabo, A., Zaray, G., & Marialigeti, K. (2015). Texture and type of polymer fiber carrier determine bacterial colonization and biofilm properties in wastewater treatment. *Chemical Engineering Journal*, 264, 824–834. <https://doi.org/10.1016/j.cej.2014.12.008>
- Five Things to Consider When Cleaning Your SLS Prints. (2017, June 12). *AMFG*. <https://amfg.ai/2017/06/12/cleaning-sls-prints/>

- Fleck, N.A, Deshpande, V.S., and Ashby, M.F. (2010). "Micro-architected materials: past, present, and future." *Proceedings of the Royal Society A*, 2495-2516.
- Franchetti, M., & Kress, C. (2017). An economic analysis comparing the cost feasibility of replacing injection molding processes with emerging additive manufacturing techniques. *The International Journal of Advanced Manufacturing Technology*, 88(9), 2573–2579. <https://doi.org/10.1007/s00170-016-8968-7>
- Gerasimidis S. (2014). Analytical assessment of steel frames progressive collapse vulnerability to corner column loss, *Journal of Constructional Steel Research*, Volume 95, pp. 1-9
- Gerasimidis S., Ampatzis A., & Bisbos C.D. (2012). A mathematical programming computational model for disproportionate collapse analysis of steel building frames, *Optimization Letters*, Volume 6, Number 3, pp. 525-535.
- Gerasimidis S., & Baniotopoulos C.C. (2011a). Evaluation of wind load integration in disproportionate collapse analysis of steel moment frames for column loss, *Journal of Wind Engineering and Industrial Aerodynamics*, Volume 99, Issue 11, pp. 1162-1173.
- Gerasimidis S., & Baniotopoulos C.C. (2011b). Steel moment frames column loss analysis: the influence of time step size, *Journal of Constructional Steel Research*, Volume 67, Issue 4, pp. 557-564.
- Gerasimidis S., & Baniotopoulos C.C. (2015). Progressive collapse mitigation of 2D steel moment frames - Assessment of the effect of different strengthening schemes, *Stahlbau*, Volume 84 (5), pp. 324-331.
- Gerasimidis S., Bisbos C.D., & Baniotopoulos C.C. (2012). Vertical geometric irregularity assessment of steel frames on robustness and disproportionate collapse, *Journal of Constructional Steel Research*, Volume 74, pp. 76-89.
- Gerasimidis S., Bisbos C.D., & Baniotopoulos C.C. (2013). A computational model for full or partial damage of single or multiple adjacent columns in disproportionate collapse analysis via linear programming, *Structure and Infrastructure Engineering*, 10 (5), pp. 670-683.
- Gerasimidis S., Deodatis G., Yan Y., & Ettouney M. (2016). Global instability induced failure of tall steel moment frame buildings, *ASCE Journal of Performance of Constructed Facilities*, 31(2): 04016082.
- Gerasimidis S., Khorasani N.E., Garlock M., Pantidis P., & Glassman, J. (2017). Resilience of tall steel moment resisting frame buildings with multi-hazard post-event fire, *Journal of Constructional Steel Research*, 139, pp. 202-219.
- Gerasimidis S., Kontoroupi T., Deodatis G., & Ettouney M. (2014). Loss-of-stability induced progressive collapse modes in 3D steel moment frames, *Structure and Infrastructure Engineering*, Volume 11 (3), pp. 334-344.
- Gerasimidis S., & Sideri T. (2016). A new partial distributed damage method for progressive collapse analysis of buildings, *Journal of Constructional Steel Research*, Volume 119, pp. 233-245.

- Gerasimidis S, Virot EE, Hutchinson JW, Rubinstein SM., (2018). On Establishing Buckling Knockdowns for Imperfection-Sensitive Shell Structures. *ASME. J. Appl. Mech*; 85(9): 091010.
- Gross, A., Pantidis, P., Bertoldi, K., & Gerasimidis, S. (2019). Correlation between topology and elastic properties of imperfect truss-lattice materials. *Journal of the Mechanics and Physics of Solids*, 124, 577–598. <https://doi.org/10.1016/j.jmps.2018.11.007>
- Gutierrez-Osorio, A. H., Ruiz-Huerta, L., Caballero-Ruiz, A., Siller, H. R., & Borja, V. (2019). Energy consumption analysis for additive manufacturing processes. *The International Journal of Advanced Manufacturing Technology*, 105(1), 1735–1743. <https://doi.org/10.1007/s00170-019-04409-3>
- Guide to Selective Laser Sintering (SLS) 3D Printing*. (n.d.). Formlabs. Retrieved March 26, 2020, from <https://formlabs.com/blog/what-is-selective-laser-sintering/>
- Hammer, M. J., & Hammer, M. J. Jr. (2012). Wastewater Processing. In V. Anthony (Ed.), *Water and Wastewater Technology, Seventh Edition*, (pp. 289-290). Upper Saddle River, NJ and Columbus, OH: Prentice Hall.
- Hamoda, M. F., & Al-Sharekh, H. A. (2000). Performance of a combined biofilm-suspended growth system for wastewater treatment. *Water Science and Technology*, 41(1), 167–175.
- HDPE LDPE LLDPE Comparison. (n.d.). Retrieved April 6, 2020, from <https://omnexus.specialchem.com/selection-guide/polyethylene-plastic>
- Hettesheimer, T., Hirzel, S., & Roß, H. B. (2018). Energy savings through additive manufacturing: An analysis of selective laser sintering for automotive and aircraft components. *Energy Efficiency*, 11(5), 1227–1245. <https://doi.org/10.1007/s12053-018-9620-1>
- Jackson, M.A., Asten, A.V., Morrow, J.D., Min, S., & Pfefferkorn, F.E. (2018). Energy Consumption Model for Additive-Subtractive Manufacturing Processes with Case Study. *International Journal of Precision Engineering and Manufacturing-Green Technology*, 5(4), 459-466. <https://doi.org/10.1007/s40684-018-0049-y>
- Javid, A.H., & Hassani, A.H., & Ghanbari, B., & Yaghmaeian, K. (2013). Feasibility of Utilizing Moving Bed Biofilm Reactor to Upgrade and Retrofit Municipal Wastewater Treatment Plants. *International Journal of Environmental Research*, 7(4), 963-972.
- Jurecska, L., & Barkács, K., & Kiss, É., & Gyulai, G., & Felföldi, T., & Törő, B., & Kovács, R., & Zárny, G. (2012). Intensification of wastewater treatment with polymer fiber-based biofilm carriers. *Microchemical Journal*, 107, 108-114. <https://www.sciencedirect.com/science/article/pii/S0026265X12001464>
- Kim, D.-H., Kim, M. S., & Hwang, J. (2012). Monitoring of Biofilm Formation on Different Material Surfaces of Medical Devices using Hyperspectral Imaging Method. In R. Raghavachari & R. Liang (Eds.), *Design and Quality for Biomedical Technologies V*

- (Vol. 8215, p. UNSP 821507). Spie-Int Soc Optical Engineering.
<https://doi.org/10.1117/12.909980>
- Kim, M., Ravault, J., Han, M., & Kim, K. (2012). Impact of the surface characteristics of rainwater tank material on biofilm development. *Water Science and Technology*, 66(6), 1225–1230. <https://doi.org/10.2166/wst.2012.245>
- Kurt, A., Cilingir, A., Bilmenoglu, C., Topcuoglu, N., & Kulekci, G. (2019). Effect of different polishing techniques for composite resin materials on surface properties and bacterial biofilm formation. *Journal of Dentistry*, 90, UNSP 103199.
<https://doi.org/10.1016/j.jdent.2019.103199>
- Laser Sintering Accuracy Study | Design Guidelines | Stratasys Direct.* (n.d.). Stratasys. Retrieved March 26, 2020, from <https://www.stratasysdirect.com/resources/design-guidelines/selective-laser-sintering-accuracy-study>
- Li, W., Li, Y.J., Lee, S., M.Y., Mok, K.M., & Hao, T. (2019). Nitrogen Removal in Moving Bed Sequencing Batch Reactors with Polyurethane Foam Cube and Luffa Sponge Carrier Materials. *Journal of Environmental Engineering*, 145 (6).
[https://doi.org/10.1061/\(ASCE\)EE.1943-7870.0001534](https://doi.org/10.1061/(ASCE)EE.1943-7870.0001534)
- Mannina, G., & Viviani, G. (2009). Hybrid moving bed biofilm reactors: an effective solution for upgrading a large wastewater treatment plant. *Water Science and Technology: A Journal of the International Association on Water Pollution Research*, 60(5), 1103–1116.
<https://doi.org/10.2166/wst.2009.416>
- Matsumoto, S., Terada, A., & Tsuneda, S. (2007). Modeling of membrane-aerated biofilm: Effects of C/N ratio, biofilm thickness and surface loading of oxygen on feasibility of simultaneous nitrification and denitrification. *Biochemical Engineering Journal*, 37(1), 98–107. <https://doi.org/10.1016/j.bej.2007.03.013>
- McQuarrie, J. P., & Maxwell, M. (2003). PILOT-SCALE PERFORMANCE OF THE MBBR PROCESS AT THE CROW CREEK WWTP, CHEYENNE, WYOMING. *Proceedings of the Water Environment Federation*, 2003, 108–119.
<https://doi.org/10.2175/193864703784641946>
- Mladenovic, K. G., Muruzovic, M. Z., & Comic, L. R. (2018). The Effects of Environmental Factors on Planktonic Growth and Biofilm Formation of *Serratia Odorifera* and *Serratia Marcescens* Isolated from Traditionally Made Cheese. *Acta Alimentaria*, 47(3), 370–378.
<https://doi.org/10.1556/066.2018.47.3.13>
- Nagarajan, H. P. N., & Haapala, K. R. (2018). Characterizing the influence of resource-energy-exergy factors on the environmental performance of additive manufacturing systems. *Journal of Manufacturing Systems*, 48, 87–96. <https://doi.org/10.1016/j.jmsy.2018.06.005>
- Naz, I., & Seher, S., & Perveen, I., & Saroj, D., & Ahmed, S. (2015). Physiological activities associated with biofilm growth in attached and suspended growth bioreactors under

- aerobic and anaerobic conditions. *Environmental Technology*, 36:13, 1657-1671, <https://doi.org/10.1080/09593330.2014.1003614>
- Ødegaard, H., Rusten, B., Westrum, T. (1994). A new moving bed biofilm reactor - applications and results. *Water Science and Technology*. 29, (10–11). 157–165. doi:10.2166/wst.1994.0757
- Orantes, J. C., & González-Martínez, S. (2003). A new low-cost biofilm carrier for the treatment of municipal wastewater in a moving bed reactor. *Water Science and Technology: A Journal of the International Association on Water Pollution Research*, 48(11–12), 243–250.
- Pabi, S., Amarnath, A., Goldstein, R., & Reekie, L. (2013). Electricity Use and Management in the Municipal Water Supply and Wastewater Industries. Palo Alto, CA: *Electric Power Research Institute*.
- Palermo, E. (2013). What is Selective Laser Sintering? Retrieved April 3, 2020, from <https://www.livescience.com/38862-selective-laser-sintering.html>
- Pantidis P., & Gerasimidis S. (2017). New Euler-type progressive collapse curves for 2D steel frames: an analytical method, *ASCE Structural Engineering*, 143 (9): 04017113.
- Pantidis P., & Gerasimidis S. (2018). Progressive collapse of 3D steel composite buildings under interior gravity column loss, *Journal of Constructional Steel Research.*, 150, pp. 60-75.
- Pearson, A. (January 22, 2018). 10 Advantages of 3D Printing. 3D Insider. <https://3dinsider.com/3d-printing-advantages/>
- Pell, M., & Wörman, A. (2008). Biological Wastewater Treatment Systems. In S. E. Jørgensen & B. D. Fath (Eds.), *Encyclopedia of Ecology* (pp. 426–441). Academic Press. <https://doi.org/10.1016/B978-008045405-4.00317-7>
- Peng, T., Kellens, K., Tang, R., Chen, C., & Chen, G. (2018). Sustainability of additive manufacturing: An overview on its energy demand and environmental impact. *Additive Manufacturing*, 21, 694–704. <https://doi.org/10.1016/j.addma.2018.04.022>
- Phillips, H. M., Steichen, M. T., & Johnson, T. L. (2010). The Second Generation of IFAS and MBBR: Lessons to Apply. *Proceedings of the Water Environment Federation, 2010*, 4478–4501. <https://doi.org/10.2175/193864710798182600>
- Philpot, T. A. (2013). Mechanical Properties of Materials. In L. Ratts (Ed.), *Mechanics of Materials, 3rd Edition*, (pp. 58-59). Hoboken, NJ: John Wiley & Sons, Inc.
- Piciooreanu, C., van Loosdrecht, M. C. M., & Heijnen, J. J. (2001). Two-dimensional model of biofilm detachment caused by internal stress from liquid flow. *Biotechnology and Bioengineering*, 72(2), 205–218. [https://doi.org/10.1002/1097-0290\(20000120\)72:2<205::AID-BIT9>3.0.CO;2-L](https://doi.org/10.1002/1097-0290(20000120)72:2<205::AID-BIT9>3.0.CO;2-L)

- Plastic Extrusion Tolerances. (2019, January 29). *Gemini Group*.
<https://geminigroup.net/blog/plastic-extrusion-tolerances/>
- R Core Team (2019). R: A language and environment for statistical computing. R Foundation for Statistical Computing, Vienna, Austria. URL <http://www.R-project.org/>.
- Rana, S., Gupta, N., & Rana, R. S. (2018). Removal of Organic pollutant with the use of Rotating Biological Contactor. *Materials Today-Proceedings*, 5(2), 4218–4224.
- Rittmann, B. E., & McCarty, P. L. (2001a). Basics of Microbiology. In G. Tchobanoglous (Ed.), *Environmental Biotechnology: Principles and Applications* (10, 16-18). Boston, MA: McGraw Hill.
- Rittmann, B. E., & McCarty, P. L. (2001b). Biofilm Kinetics. In G. Tchobanoglous (Ed.), *Environmental Biotechnology: Principles and Applications* (208-215). Boston, MA: McGraw Hill.
- Rittmann, B. E., & McCarty, P. L. (2001c). Microbial Kinetics. In G. Tchobanoglous (Ed.), *Environmental Biotechnology: Principles and Applications* (165-169). Boston, MA: McGraw Hill.
- Rittmann, B. E., & McCarty, P. L. (2001d). Nitrification. In G. Tchobanoglous (Ed.), *Environmental Biotechnology: Principles and Applications* (472-473). Boston, MA: McGraw Hill.
- Rittmann, B. E., & McCarty, P. L. (2001e). The Activated Sludge Process. In G. Tchobanoglous (Ed.), *Environmental Biotechnology: Principles and Applications* (335-336). Boston, MA: McGraw Hill.
- Sabiston, G., & Kim, I. Y. (2020). 3D topology optimization for cost and time minimization in additive manufacturing. *Structural and Multidisciplinary Optimization*, 61(2), 731–748.
<https://doi.org/10.1007/s00158-019-02392-7>
- Saeki, D., Nagashima, Y., Sawada, I., & Matsuyama, H. (2016). Effect of hydrophobicity of polymer materials used for water. Purification membranes on biofilm formation dynamics. *Colloids and Surfaces A-Physicochemical and Engineering Aspects*, 506, 622–628. <https://doi.org/10.1016/j.colsurfa.2016.07.036>
- Sarjit, A., Tan, S. M., & Dykes, G. A. (2015). Surface modification of materials to encourage beneficial biofilm formation. *Aims Bioengineering*, 2(4), 404–422.
<https://doi.org/10.3934/bioeng.2015.4.404>
- Schlegel, S., & Koeser, H. (2007). Wastewater treatment with submerged fixed bed biofilm reactor systems – design rules, operating experiences and ongoing developments. *Water Science & Technology*, 55(8-9), 83-89.
- Sehar, S., & Naz, I. (2016). Role of the Biofilms in Wastewater Treatment. *Microbial Biofilms - Importance and Applications*. <https://doi.org/10.5772/63499>

- Siddique, A., Suraraksa, B., Horprathum, M., Oaew, S., & Cheunkar, S. (2019). Wastewater biofilm formation on self-assembled monolayer surfaces using elastomeric flow cells. *Anaerobe*, 57, 11–18. <https://doi.org/10.1016/j.anaerobe.2019.03.005>
- Sideri J., Mullen C.L., Gerasimidis S., & Deodatis G. (2017). Distributed Column damage effect on progressive collapse vulnerability in steel buildings exposed to an external blast event, *ASCE Journal of Performance of Constructed Facilities*, 31(5): 04017077.
- Soleimani, M., Wriggers, P., Rath, H., & Stiesch, M. (2016). Numerical simulation and experimental validation of biofilm in a multi-physics framework using an SPH based method. *Computational Mechanics*, 58(4), 619–633. <https://doi.org/10.1007/s00466-016-1308-9>
- Song J., Sun Q., Luo S., Arwade S.R., **Gerasimidis S.**, Guo Y., Zhang G., (2018). Compression behavior of individual thin-walled metallic hollow spheres with patterned distributions of microporosity, *Material Science and Engineering A*, 734, pp. 453-475.
- Sonwani, R. K., Swain, G., Giri, B. S., Singh, R. S., & Rai, B. N. (2019). A novel comparative study of modified carriers in moving bed biofilm reactor for the treatment of wastewater: Process optimization and kinetic study. *Bioresource Technology*, 281, 335–342. <https://doi.org/10.1016/j.biortech.2019.02.121>
- Stavridou, N., Efthymiou, E., Gerasimidis, S., & Baniotopoulos C.C. (2015). Investigation of stiffening schemes effectiveness towards buckling stability enhancement in tubular steel wind turbine towers, *Steel and Composite Structures*, Volume 19 (5), pp. 324-331.
- Staudt, C., Horn, H., Hempel, D.C., & Neu, T.R. (2004). Volumetric measurements of bacterial cells and extracellular polymeric substance glycoconjugates in biofilms. *Biotechnology and Bioengineering*, 88 (5), 585-592. <https://doi-org.silk.library.umass.edu/10.1002/bit.20241>
- Steichen, M., Sabherwal, B., Shaw, A., L. Johnson, T., Martin, M., Nussbaum, B., & Kazemi, S. (2009). Piloting Program to Optimize Design and Operation of Innovative MBBR Treatment Strategy. *Proceedings of the Water Environment Federation*, 2009, 3575–3594. <https://doi.org/10.2175/193864709793953115>
- Stender, B., Hilbert, F., Dupuis, Y., Krupp, A., Matei, W., & Houbertz, R. (2019). Manufacturing strategies for scalable high-precision 3D printing of structures from the micro to the macro range. *Advanced Optical Technologies*, 8(3-4), 225-231. <https://doi.org/10.1515/aot-2019-0022>
- Suarez, C., Piculell, M., Modin, O., Langenheder, S., Persson, F., & Hermansson, M. (2019). Thickness determines microbial community structure and function in nitrifying biofilms via deterministic assembly. *Scientific Reports*, 9, 5110. <https://doi.org/10.1038/s41598-019-41542-1>
- Subashchandrabose, S. R., Ramakrishnan, B., Megharaj, M., Venkateswarlu, K., & Naidu, R. (2011). Consortia of cyanobacteria/microalgae and bacteria: Biotechnological potential.

- Biotechnology Advances*, 29(6), 896–907.
<https://doi.org/10.1016/j.biotechadv.2011.07.009>
- Sun, Z., Ding, C., Xi, J., Lu, L., & Yang, B. (2020). Enhancing biofilm formation in biofilters for benzene, toluene, ethylbenzene, and xylene removal by modifying the packing material surface. *Bioresource Technology*, 296, 122335.
<https://doi.org/10.1016/j.biortech.2019.122335>
- Szulzyk-Cieplak, J., Tarnogorska, A., & Lenik, Z. (2018). Study on the Influence of Selected Technological Parameters of a Rotating Biological Contactor on the Degree of Liquid Aeration. *Journal of Ecological Engineering*, 19(6), 247–253.
<https://doi.org/10.12911/22998993/92512>
- Tagliaferri, V., Trovalusci, F., Guarino, S., & Venettacci, S. (2019). Environmental and Economic Analysis of FDM, SLS and MJF Additive Manufacturing Technologies. *Materials*, 12(24). <https://doi.org/10.3390/ma12244161>
- Tancogne-Dejean, T., & Mohr, D. (2018). Elastically-isotropic truss lattice materials of reduced plastic anisotropy. *International Journal of Solids and Structures*, 138, 24-39
- Tierra, G., Pavissich, J.P., Nerenberg, R., Xu, Z., & Alber, M.S. (2015). Multicomponent model of deformation and detachment of a biofilm under fluid flow. *Journal of The Royal Society Interface*, 12(106), 20150045. <https://doi.org/10.1098/rsif.2015.0045>
- Torresi, E., Fowler, S. J., Polesel, F., Bester, K., Andersen, H. R., Smets, B. F., Plósz, B. Gy., & Christensson, M. (2016). Biofilm Thickness Influences Biodiversity in Nitrifying MBBRs—Implications on Micropollutant Removal. *Environmental Science & Technology*, 50(17), 9279–9288. <https://doi.org/10.1021/acs.est.6b02007>
- von der Schulenburg, D. A. G., Pintelon, T. R. R., Picioreanu, C., van Loosdrecht, M. C. M., & Johns, M. L. (2009). Three-dimensional simulations of biofilm growth in porous media. *AIChE Journal*, 55(2), 494–504. <https://doi.org/10.1002/aic.11674>
- Wang, S., Parajuli, S., Sivalingam, V., & Bakke, R. (2019). Biofilm in Moving Bed Biofilm Process for Wastewater Treatment. *Bacterial Biofilms*.
<https://doi.org/10.5772/intechopen.88520>
- Wanjin, L., Jie, L.Y., Ming-Yuen, L.S., Meng, M.K., & Tianwei, H. (2019). Nitrogen Removal in Moving Bed Sequencing Batch Reactors with Polyurethane Foam Cube and Luffa Sponge Carrier Materials. *Journal of Environmental Engineering*, 145(6), 04019025.
[https://doi.org/10.1061/\(ASCE\)EE.1943-7870.0001534](https://doi.org/10.1061/(ASCE)EE.1943-7870.0001534)
- Wellington, M. (2014). *How Does Selective Laser Sintering Work?*
<https://3dprinthq.com/how-does-selective-laser-sintering-work/>
- Westerweel, B., Basten, R. J. I., & van Houtum, G.-J. (2018). Traditional or Additive Manufacturing? Assessing Component Design Options through Lifecycle Cost Analysis.

European Journal of Operational Research, 270(2), 570–585.

<https://doi.org/10.1016/j.ejor.2018.04.015>

- Walachowicz, F., Bernsdorf, I., Papenfuss, U., Zeller, C., Graichen, A., Navrotsky, V., Rajvanshi, N., & Kiener, C. (2017). Comparative Energy, Resource and Recycling Lifecycle Analysis of the Industrial Repair Process of Gas Turbine Burners Using Conventional Machining and Additive Manufacturing. *Journal of Industrial Ecology*, 21(S1), S203-S215. <https://doi.org/10.1111/jiec.12637>
- Wojciechowski, E., Chang, A. Y., Balassone, D., Ford, J., Cheng, T. L., Little, D., Menezes, M. P., Hogan, S., & Burns, J. (2019). Feasibility of designing, manufacturing and delivering 3D printed ankle-foot orthoses: A systematic review. *Journal of Foot and Ankle Research*, 12(1), 11. <https://doi.org/10.1186/s13047-019-0321-6>
- Yadav K.K., Gerasimidis S., (2020a). Thin steel wavy wind turbine towers: A novel approach to make imperfection insensitive tall and super-tall wind turbine towers, *Journal of Constructional Steel Research*, 172, 106228.
- Yadav K.K., Gerasimidis S., (2020b). Imperfection insensitivity of thin wavy cylindrical shells under axial compression or bending, *ASME. Journal of Applied Mechanics*, 87(4): 041003.
- Yadav K.K., Gerasimidis S., (2019). Instability of thin steel cylindrical shells under bending, *Thin-Walled Structures*, 137, pp. 151-166.
- Yang, J., Cheng, S., Li, C., Sun, Y., & Huang, H. (2019). Shear Stress Affects Biofilm Structure and Consequently Current Generation of Bioanode in Microbial Electrochemical Systems (MESs). *Frontiers in Microbiology*, 10, 398. <https://doi.org/10.3389/fmicb.2019.00398>
- Yang, Y., & Li, L. (2018). Cost modeling and analysis for Mask Image Projection Stereolithography additive manufacturing: Simultaneous production with mixed geometries. *International Journal of Production Economics*, 206, 146–158. <https://doi.org/10.1016/j.ijpe.2018.09.023>
- Zafar, M. Q., & Zhao, H. (2020). 4D Printing: Future Insight in Additive Manufacturing. *Metals and Materials International*, 26(5), 564–585. <https://doi.org/10.1007/s12540-019-00441-w>
- Zok, F.W., Latture, R.M., & Begley, M.R. (2016). Periodic truss structures. *Journal of the Mechanics and Physics of Solids*, 96, 184-203.

9. Appendix

Simple Cube

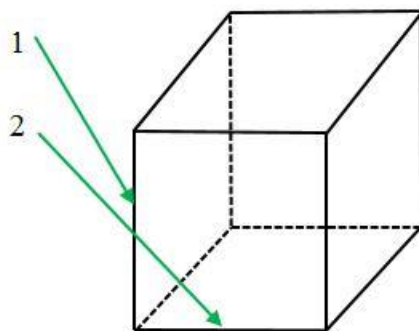


Figure 9-1: Strut Serialization of the Simple Cube Topology

Octahedron

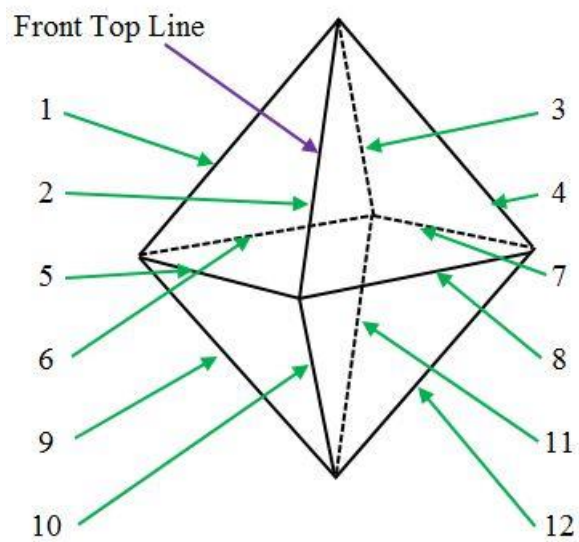


Figure 9-2: Strut Serialization of the Octahedron Topology

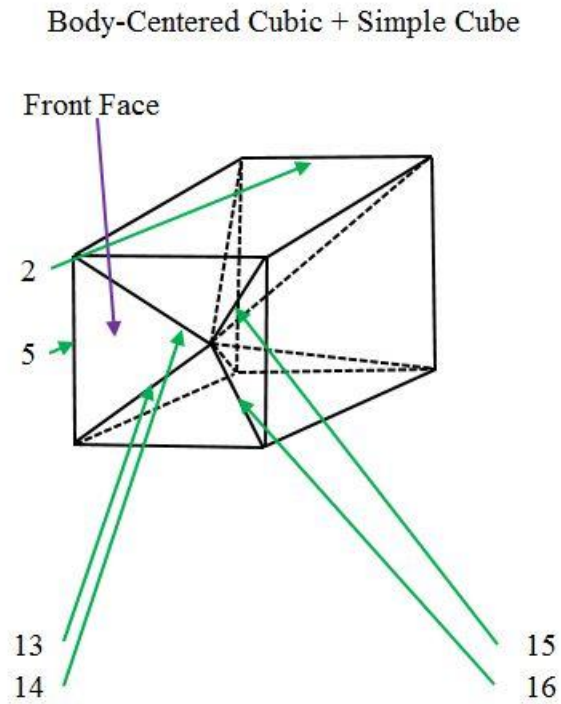


Figure 9-3: Strut Serialization of the Body-Centered Cubic + Simple Cube Topology

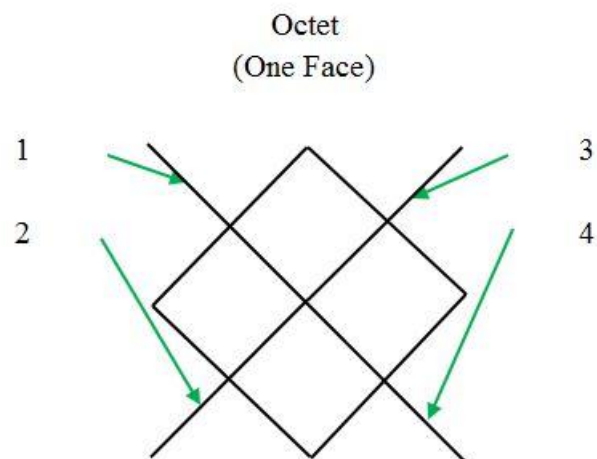


Figure 9-4: Strut Serialization of the Octet Topology

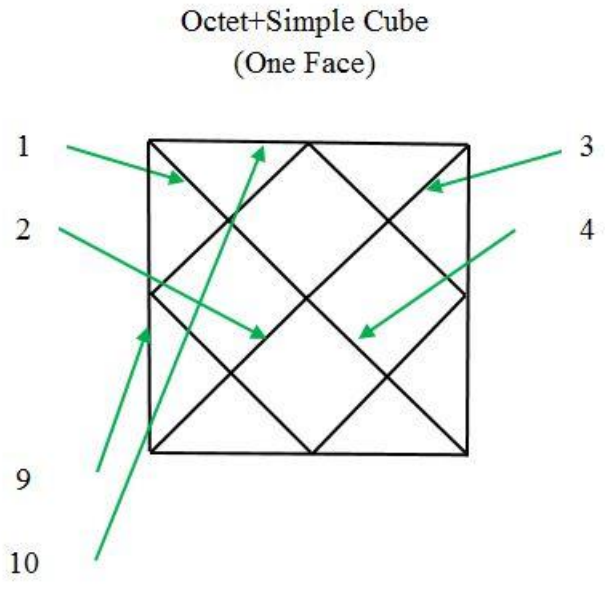


Figure 9-5: Strut Serialization of the Octet + Simple Cube Topology

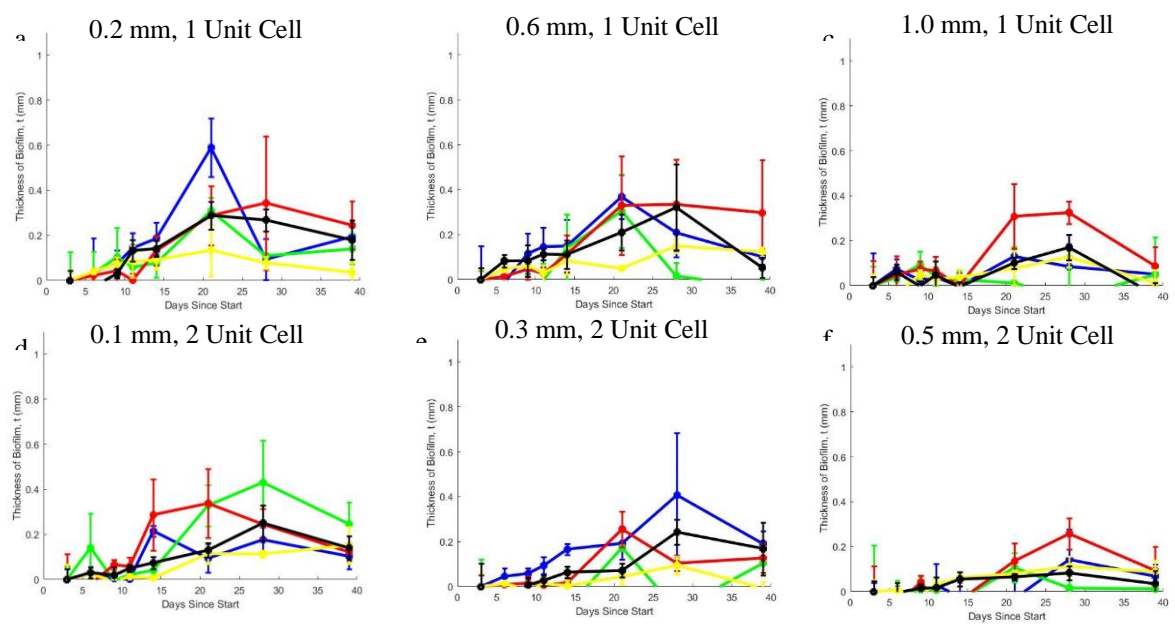


Figure 9-6: Quantitative ImageJ Measurements Taken During the Preliminary Study

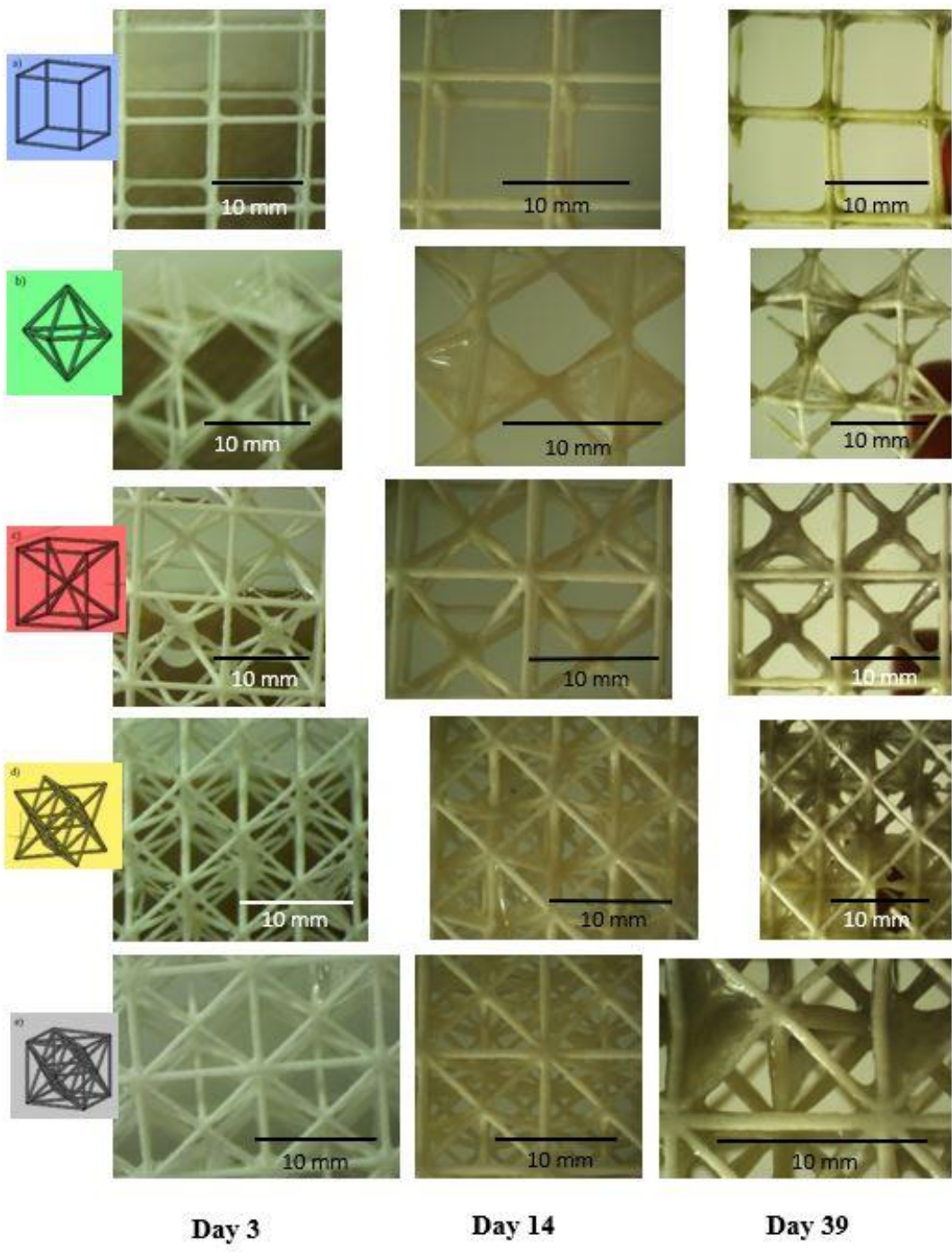


Figure 9-7: 5 geometries used for growing biofilm over time. All geometries are the 1 unit cell, 0.2 mm version of the topologies. The topologies are, from top to bottom, the simple cube, the octahedron, the body-centered cubic + simple cube, the octet, and the octet + simple cube. The time images, from left to right, are day 3, day 14, and day 39. Note: the colors of the topologies on the left side of the images correlates with the colors of results that will be shown of the topologies in sections 5 and 6 of this thesis.

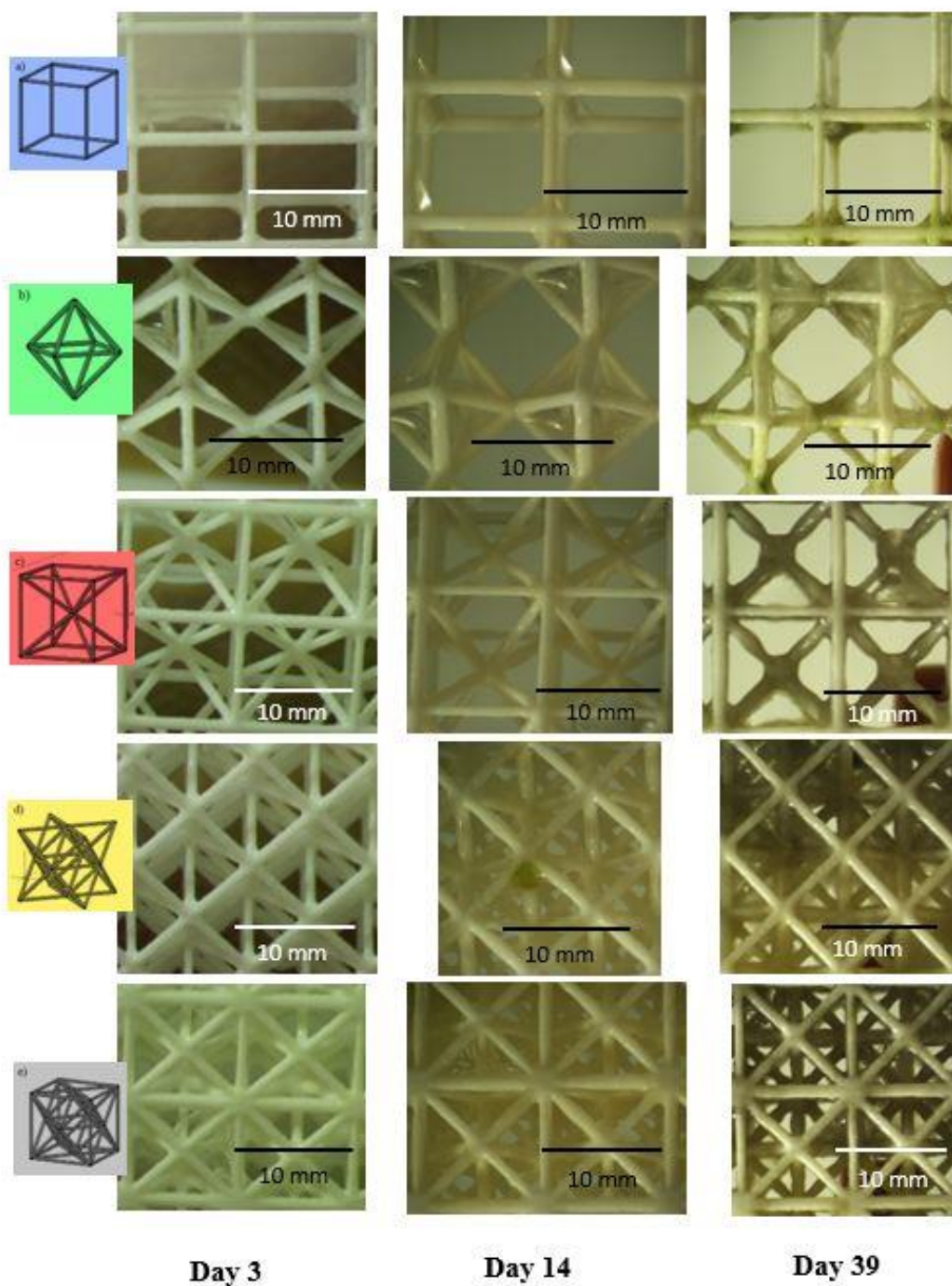


Figure 9-8: 5 geometries used for growing biofilm over time. All geometries are the 1 unit cell, 0.4 mm version of the topologies. The topologies are, from top to bottom, the simple cube, the octahedron, the body-centered cubic + simple cube, the octet, and the octet + simple cube. The time images, from left to right, are day 3, day 14, and day 39. Note: the colors of the topologies on the left side of the images correlates with the colors of results that will be shown of the topologies in sections 5 and 6 of this thesis.

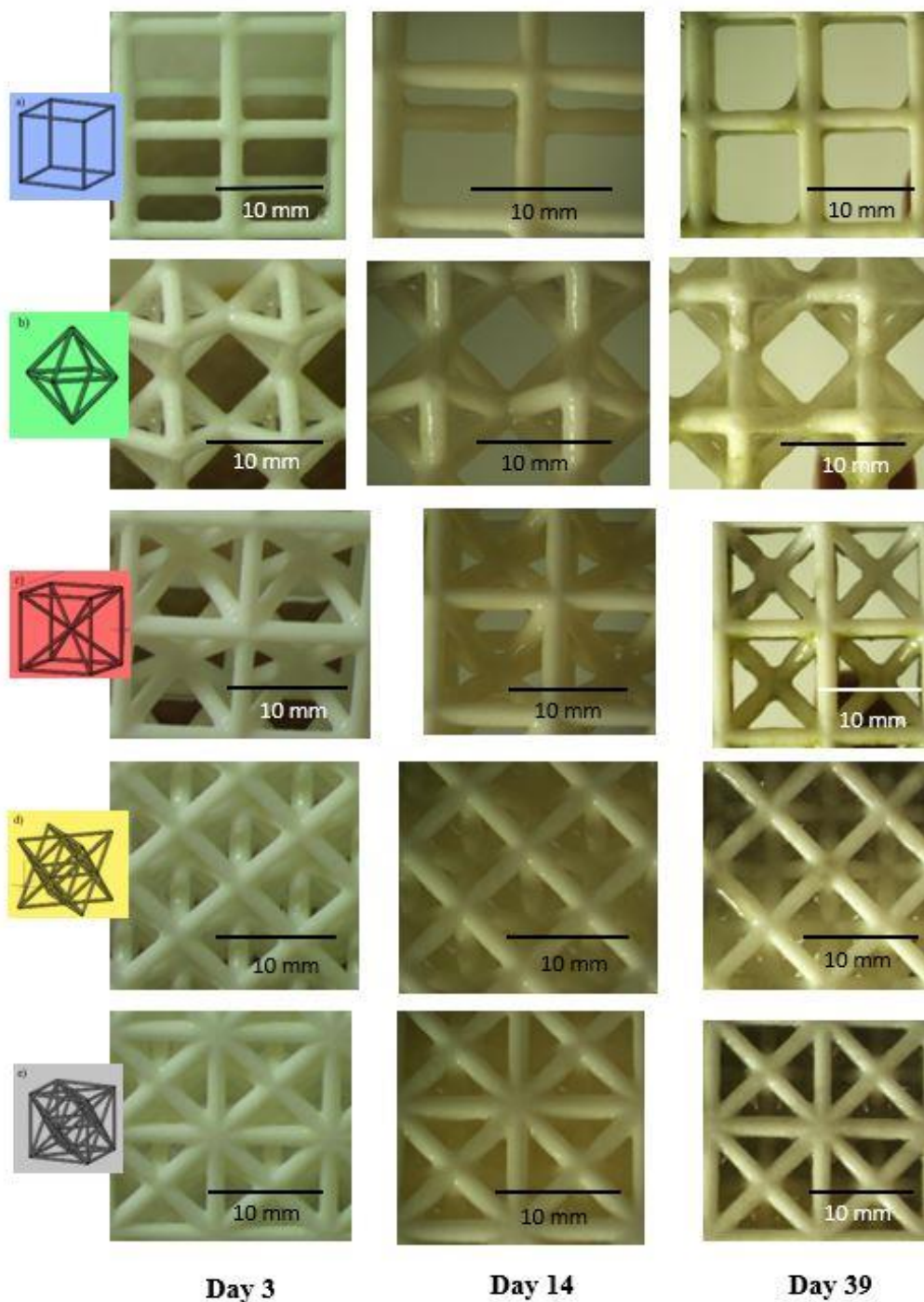


Figure 9-9: 5 geometries used for growing biofilm over time. All geometries are the 1 unit cell, 0.8 mm version of the topologies. The topologies are, from top to bottom, the simple cube, the octahedron, the body-centered cubic + simple cube, the octet, and the octet + simple cube. The time images, from left to right, are day 3, day 14, and day 39. Note: the colors of the topologies on the left side of the images correlates with the colors of results that will be shown of the topologies in sections 5 and 6 of this thesis.

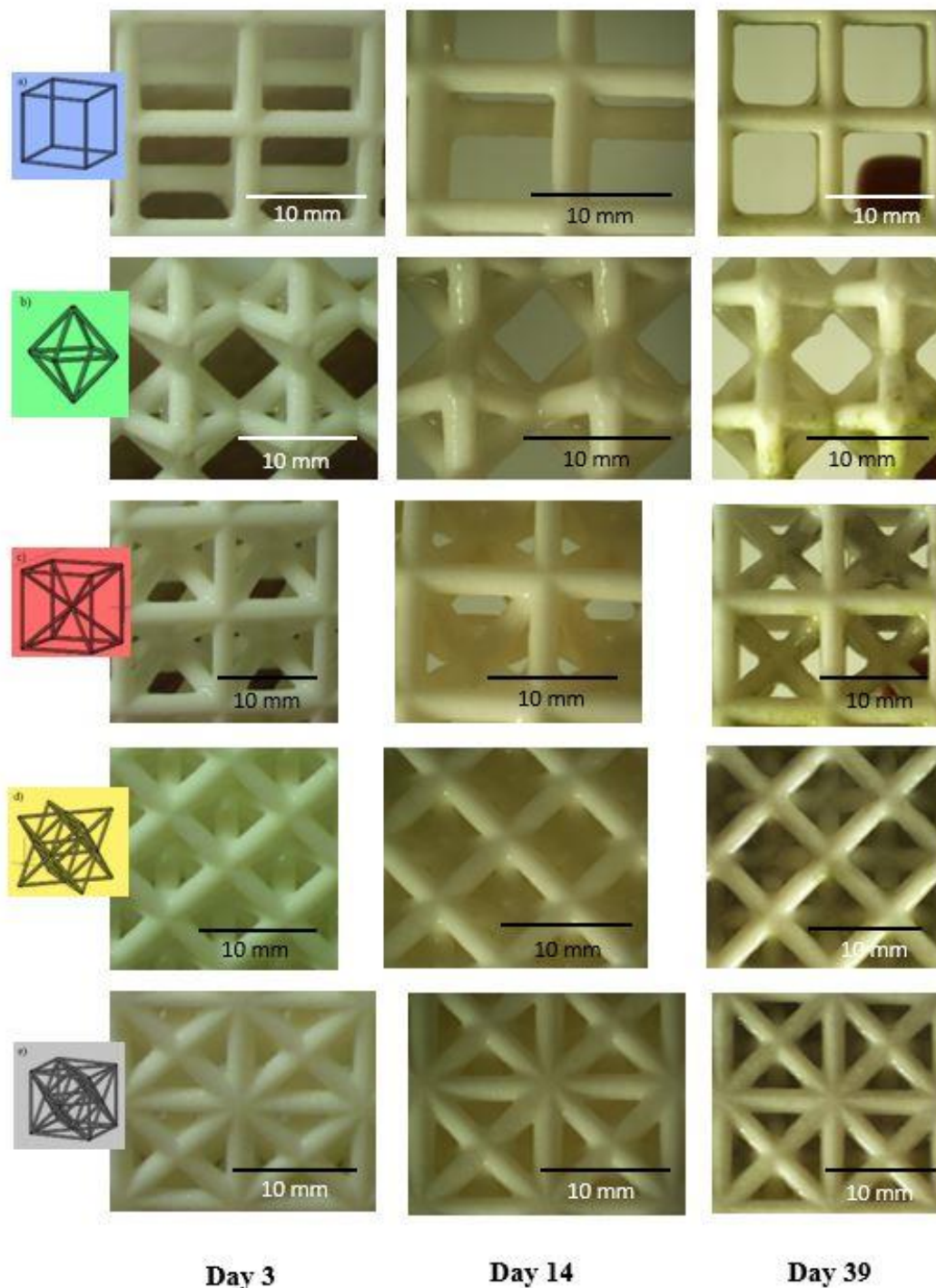


Figure 9-10: 5 geometries used for growing biofilm over time. All geometries are the 1 unit cell, 1.0 mm version of the topologies. The topologies are, from top to bottom, the simple cube, the octahedron, the body-centered cubic + simple cube, the octet, and the octet + simple cube. The time images, from left to right, are day 3, day 14, and day 39. Note: the colors of the topologies on the left side of the images correlates with the colors of results that will be shown of the topologies in sections 5 and 6 of this thesis.

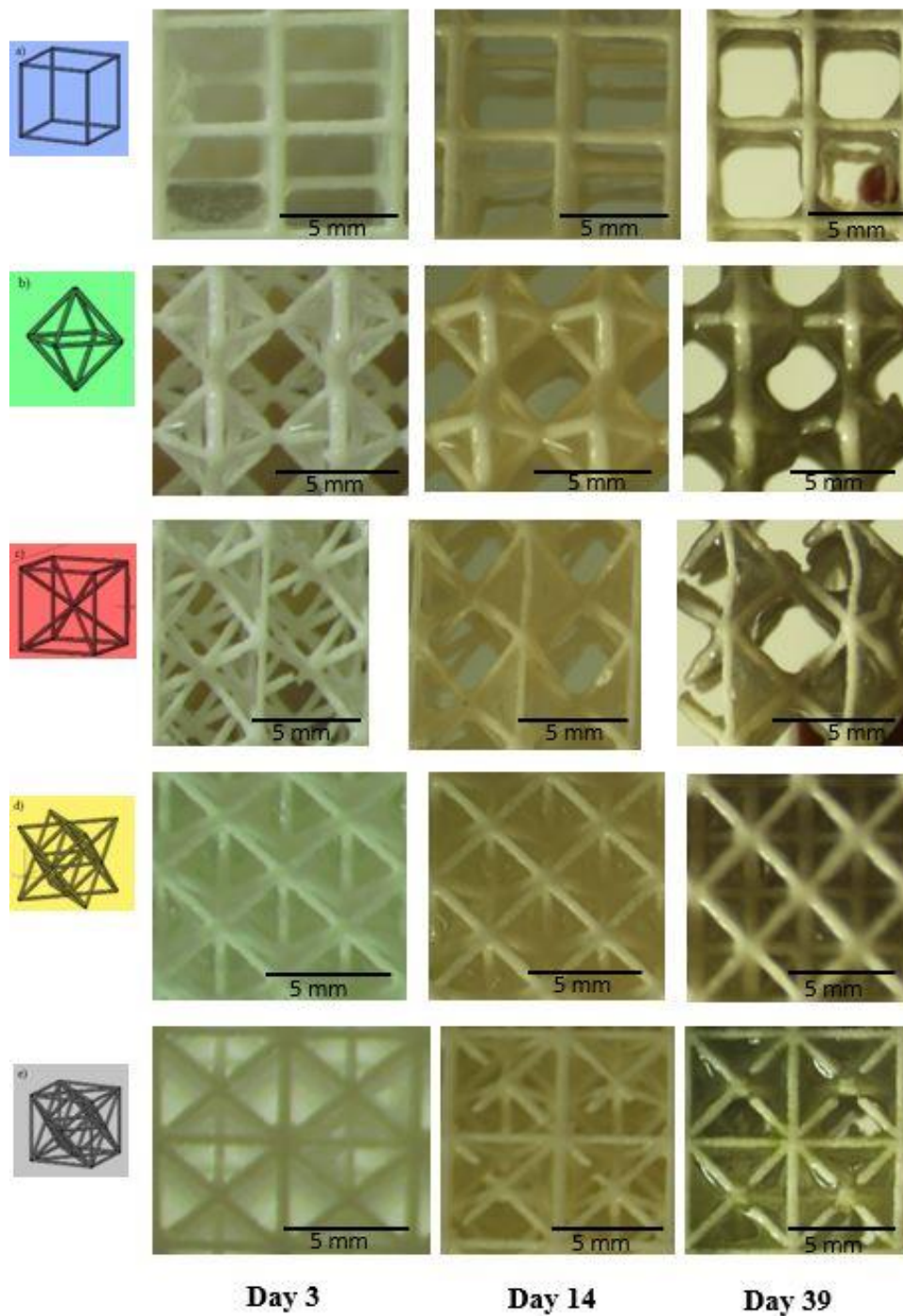


Figure 9-11: 5 geometries used for growing biofilm over time. All geometries are the 2 unit cell, 0.1 mm version of the topologies. The topologies are, from top to bottom, the simple cube, the octahedron, the body-centered cubic + simple cube, the octet, and the octet + simple cube. The time images, from left to right, are day 3, day 14, and day 39. Note: the colors of the topologies on the left side of the images correlates with the colors of results that will be shown of the topologies in sections 5 and 6 of this thesis.

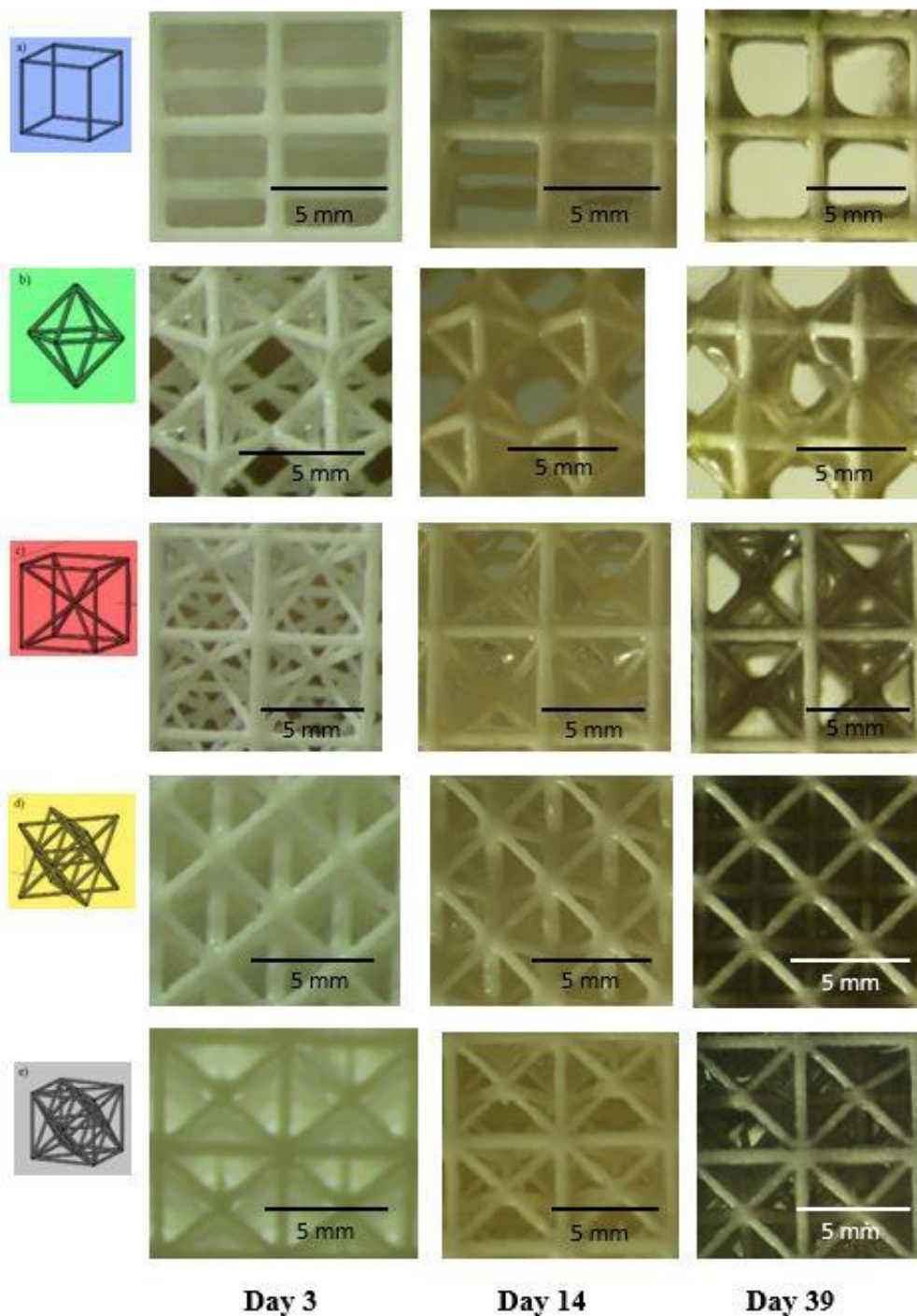


Figure 9-12: 5 geometries used for growing biofilm over time. All geometries are the 2 unit cell, 0.2 mm version of the topologies. The topologies are, from top to bottom, the simple cube, the octahedron, the body-centered cubic + simple cube, the octet, and the octet + simple cube. The time images, from left to right, are day 3, day 14, and day 39. Note: the colors of the topologies on the left side of the images correlates with the colors of results that will be shown of the topologies in sections 5 and 6 of this thesis.

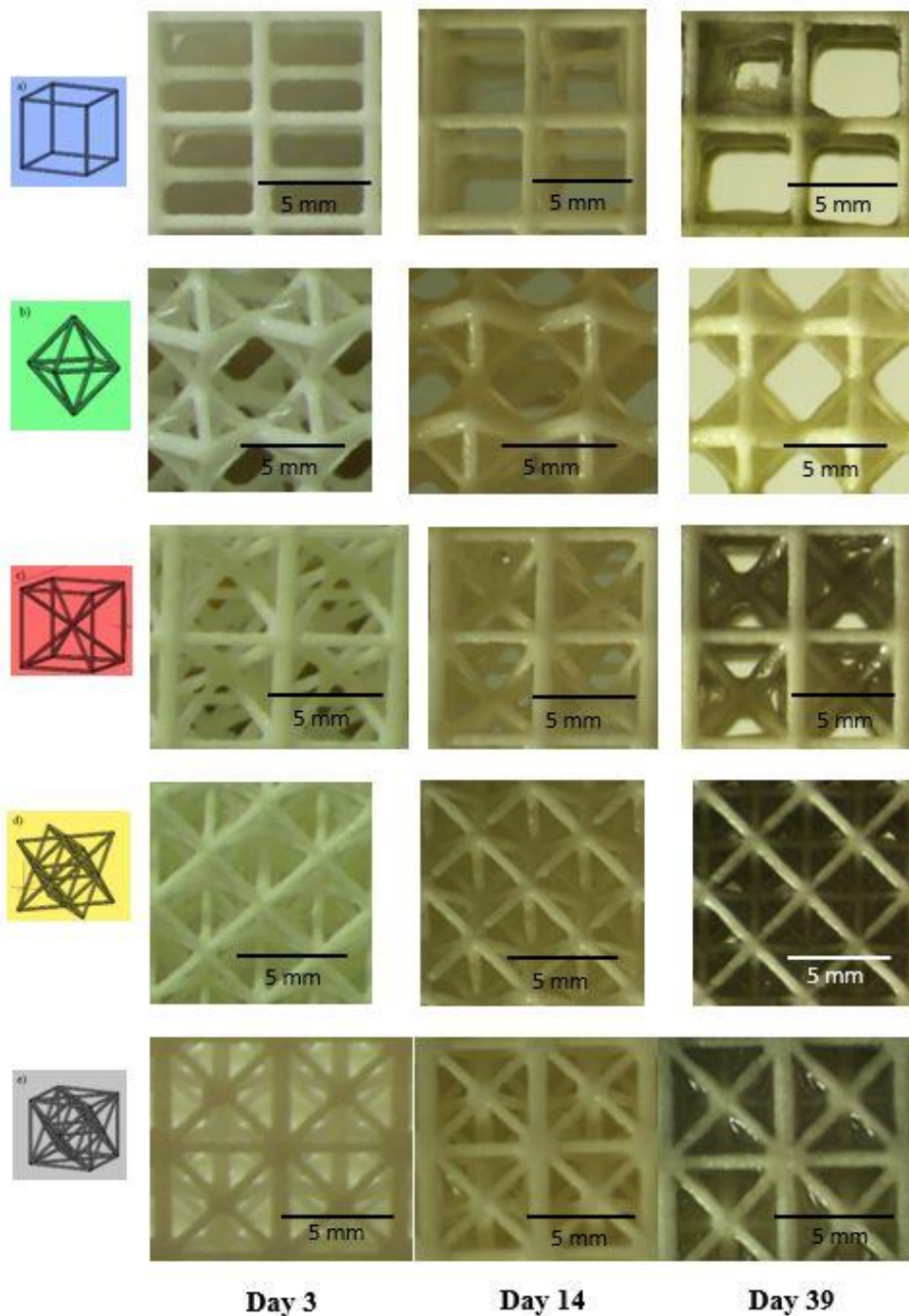


Figure 9-13: 5 geometries used for growing biofilm over time. All geometries are the 2 unit cell, 0.3 mm version of the topologies. The topologies are, from top to bottom, the simple cube, the octahedron, the body-centered cubic + simple cube, the octet, and the octet + simple cube. The time images, from left to right, are day 3, day 14, and day 39. Note: the colors of the topologies on the left side of the images correlates with the colors of results that will be shown of the topologies in sections 5 and 6 of this thesis.

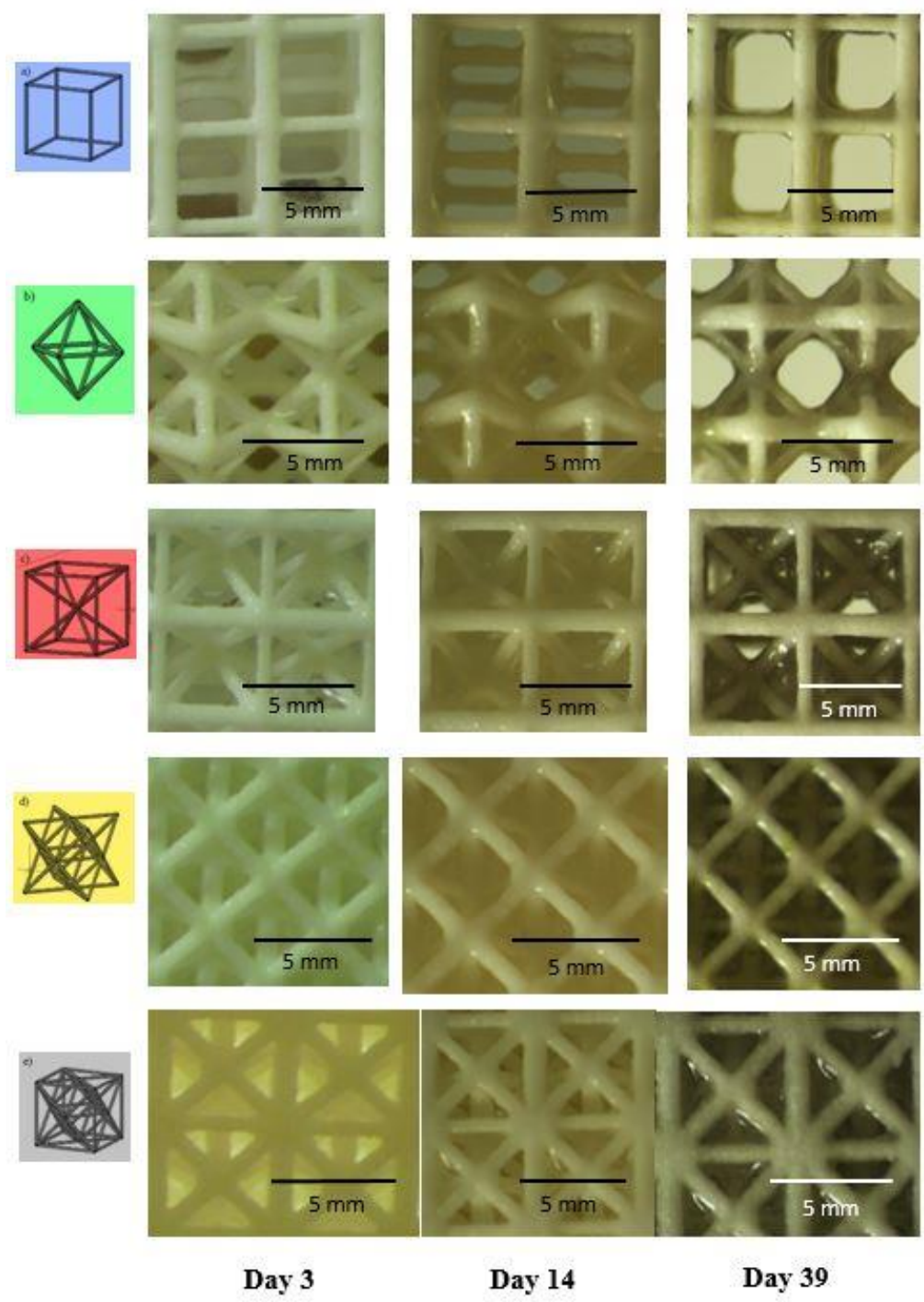


Figure 9-14: 5 geometries used for growing biofilm over time. All geometries are the 2 unit cell, 0.4 mm version of the topologies. The topologies are, from top to bottom, the simple cube, the octahedron, the body-centered cubic + simple cube, the octet, and the octet + simple cube. The time images, from left to right, are day 3, day 14, and day 39. Note: the colors of the topologies on the left side of the images correlates with the colors of results that will be shown of the topologies in sections 5 and 6 of this thesis.

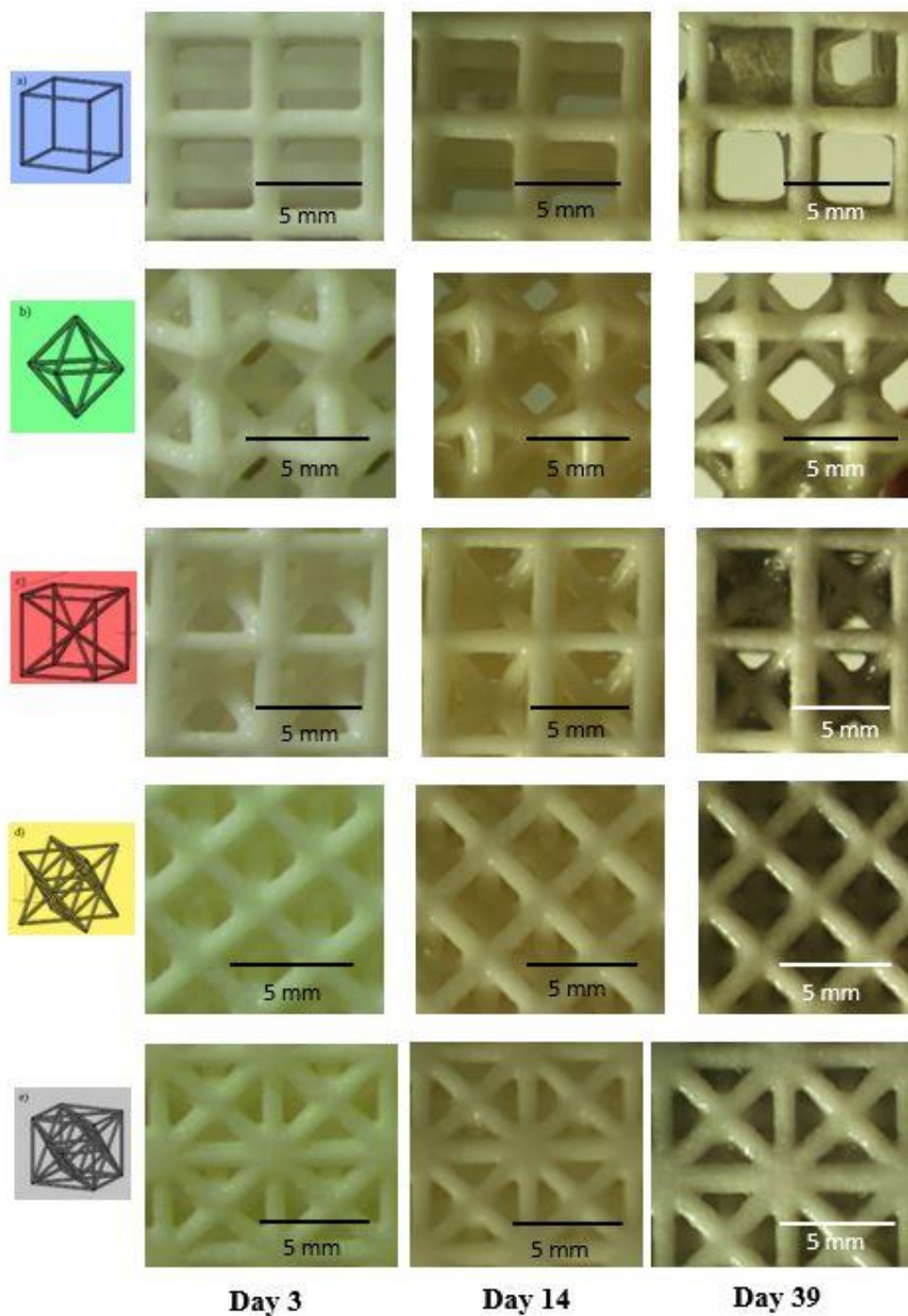


Figure 9-15: 5 geometries used for growing biofilm over time. All geometries are the 2 unit cell, 0.5 mm version of the topologies. The topologies are, from top to bottom, the simple cube, the octahedron, the body-centered cubic + simple cube, the octet, and the octet + simple cube. The time images, from left to right, are day 3, day 14, and day 39. Note: the colors of the topologies on the left side of the images correlates with the colors of results that will be shown of the topologies in sections 5 and 6 of this thesis.

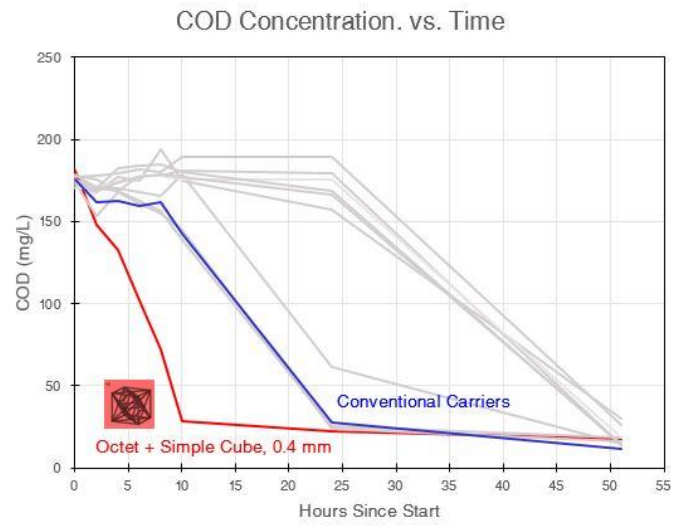


Figure 9-16: First batch study: COD concentration vs. time. Biofilm was visually lacking during this batch study, and therefore this study was not a good assessment of carriers with abundant biofilm.

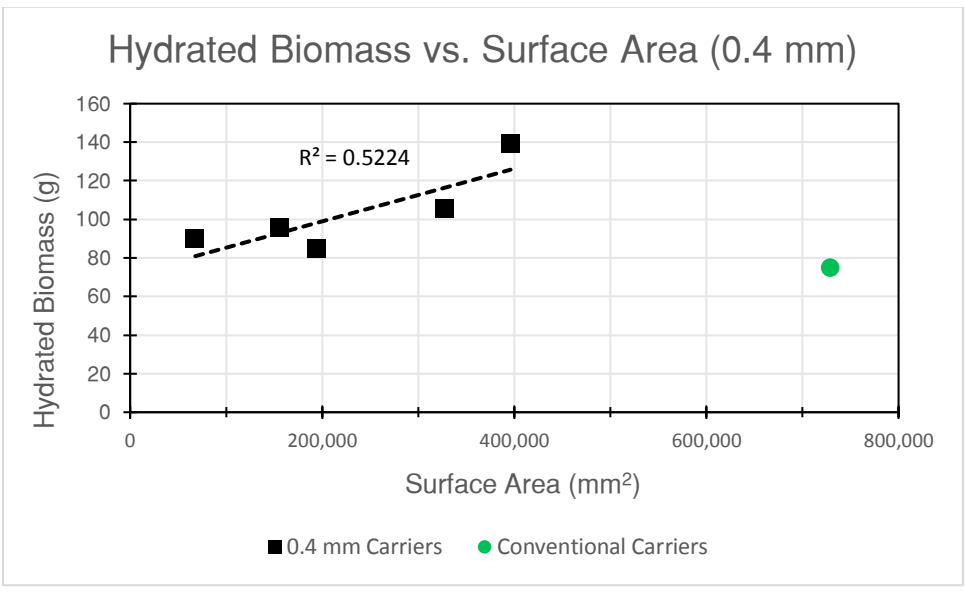


Figure 9-17: Hydrated Biomass vs. Surface Area for the 0.4 mm Cubes

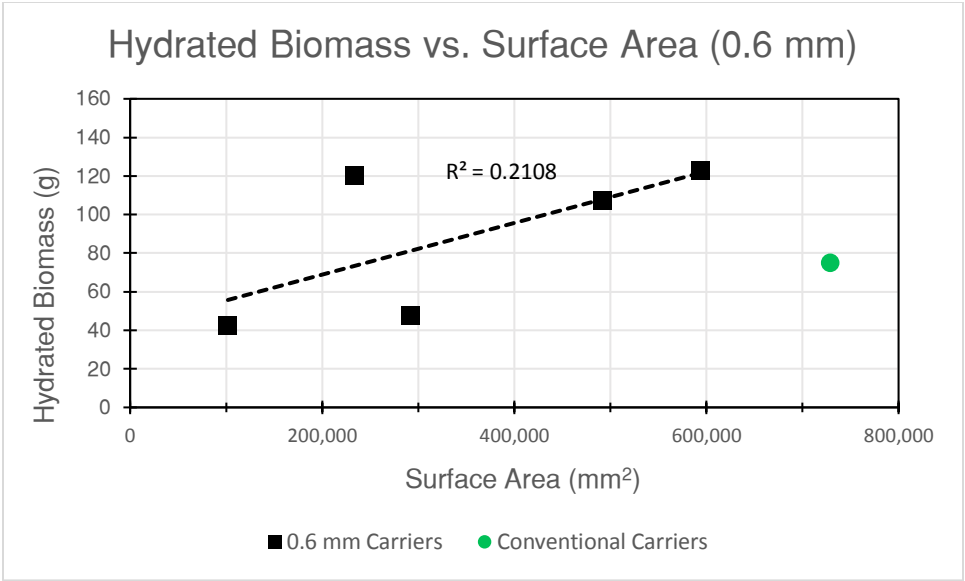


Figure 9-18: Hydrated Biomass vs. Surface Area for the 0.6 mm Cubes

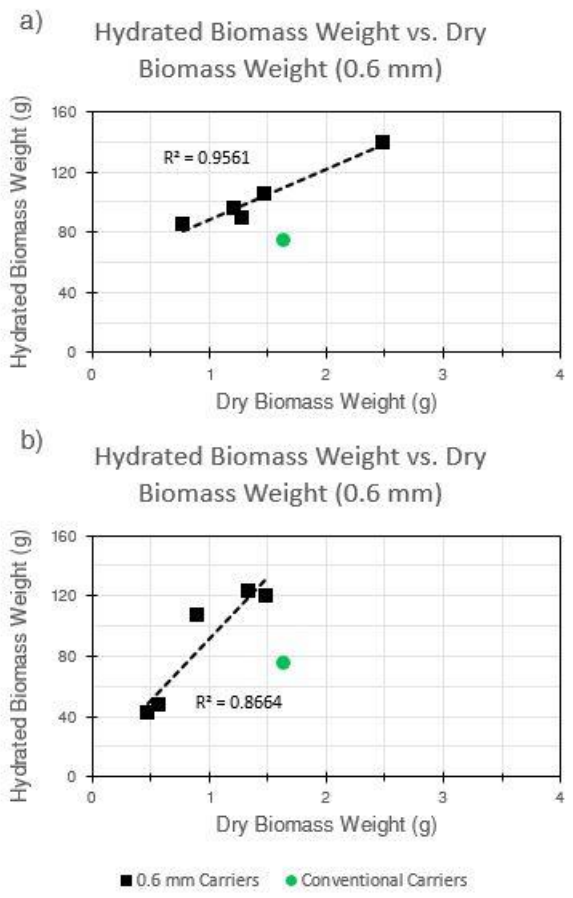


Figure 9-19: Hydrated biomass weight vs. dry biomass weight. Hydrated biomass is presented on the vertical axis, while dry biomass is presented on the horizontal axis. The architected

carriers are represented as black markers with a line of best fit connecting them. The top graph represents the 0.4 mm carriers, while the bottom graph represents the 0.6 mm carriers.

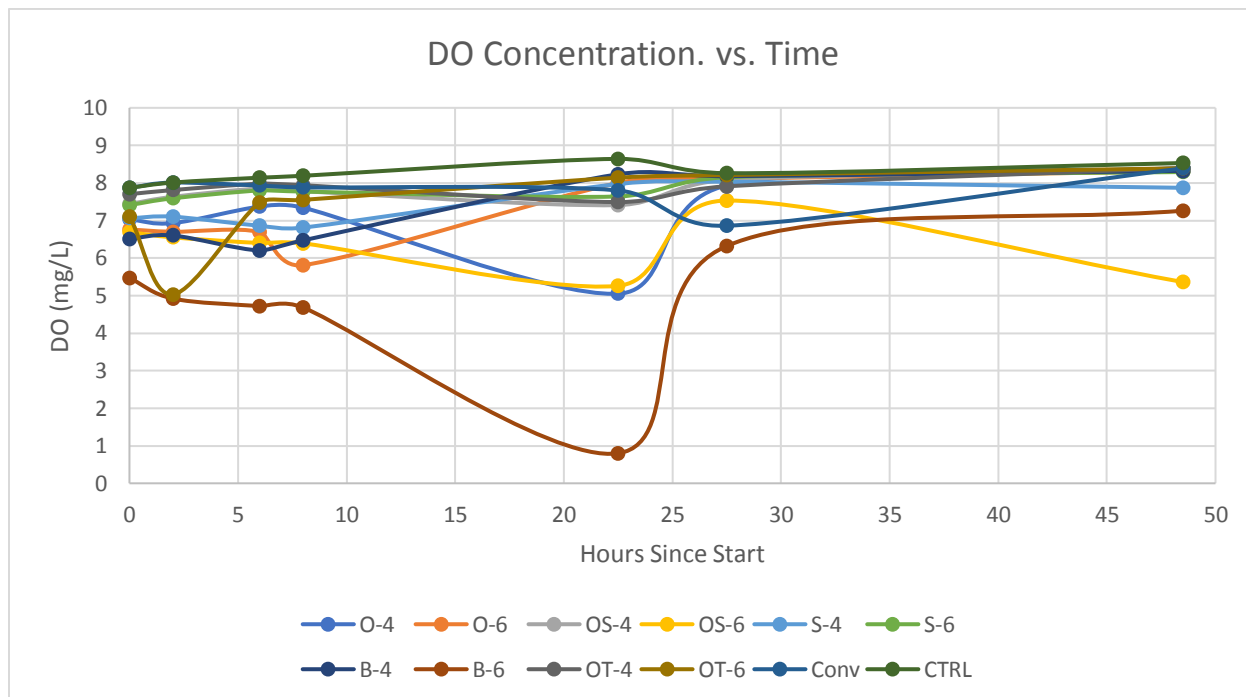


Figure 9-20: Dissolved Oxygen vs. Time Measured During the Second Batch Study

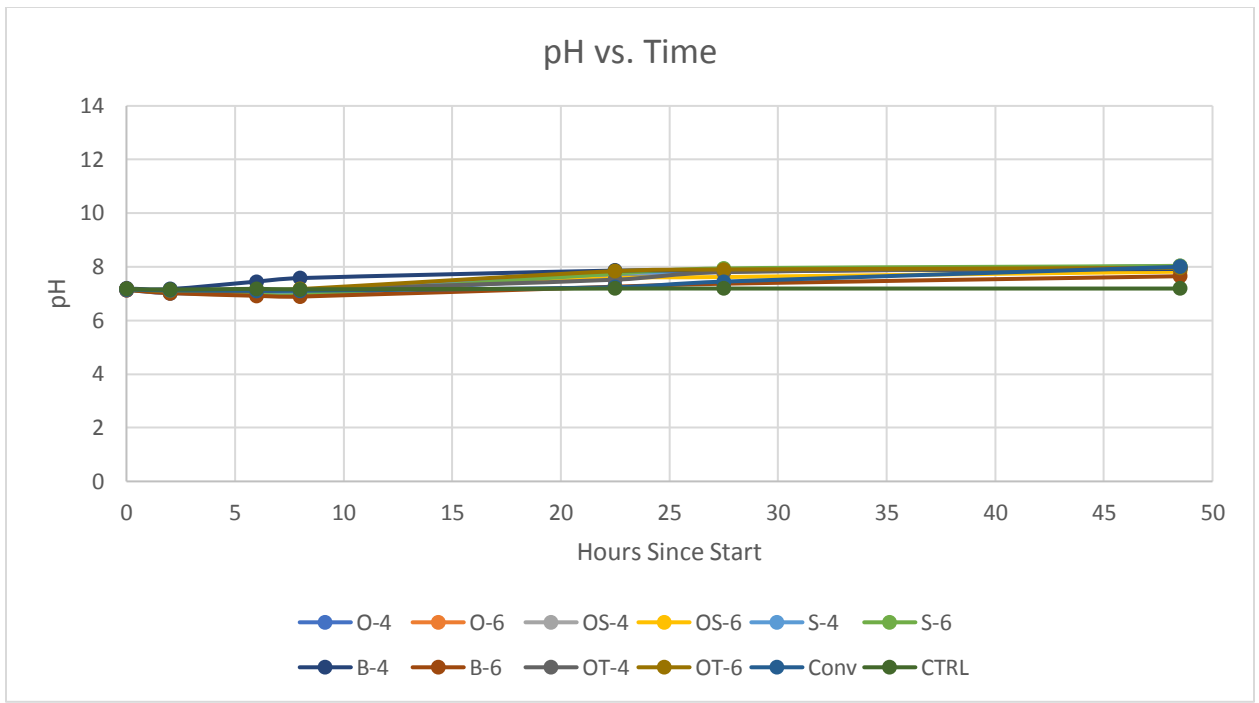


Figure 9-21: pH vs. Time Measured During the Second Batch Study

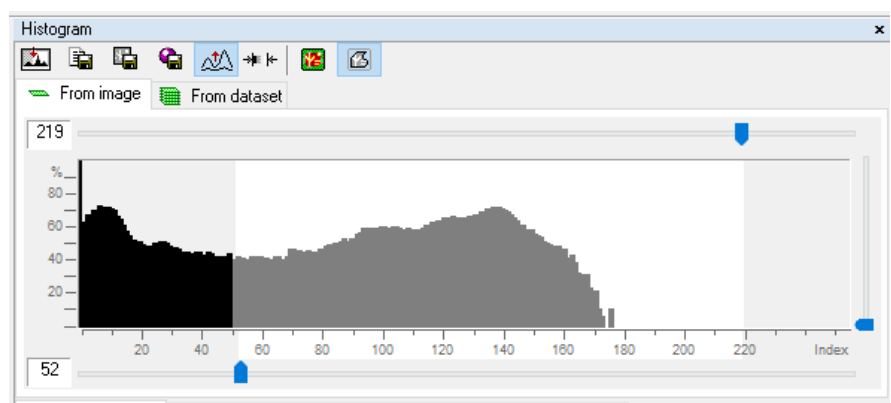


Figure 9-22: Screenshot of Micro-CT CT-An Screen: Thresholding Window used During Binarization

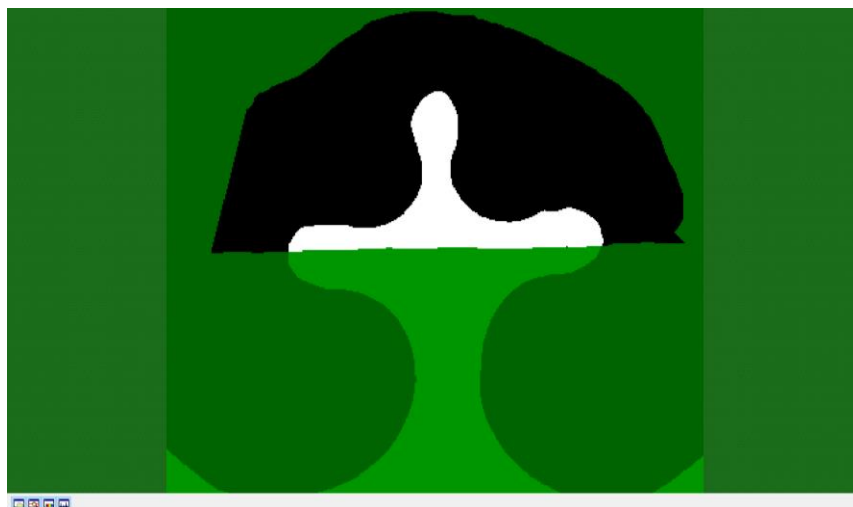


Figure 9-23: Screenshot of Micro-CT CT-An Screen: Top Half of Geometry Selection. Image is Binarized

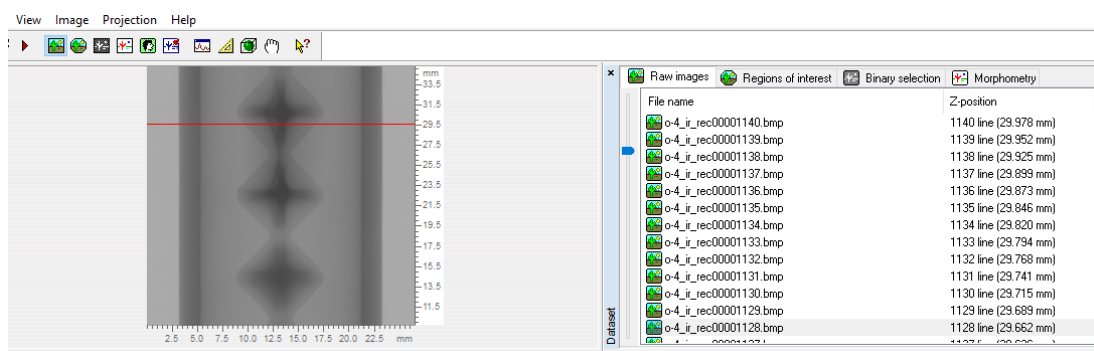


Figure 9-24: Screenshot of Micro-CT CT-An Screen: Top Half of Geometry Selection. Volume of Interest Selection